NAGOYA University

Doctoral Thesis

CONSTRAINT ON ANNIHILATING DARK MATTER WITH STACKING OF LOCAL FAINT OBJECTS

Author: Daiki Hashimoto *Supervisor: Kiyotomo Ichiki*

A thesis submitted in fulfillment of the requirements
for the degree of doctor of philosophy

Acknowledgements

I am grateful to Associate Professor, Kiyotomo Ichiki for the greatly careful and helpful supervising. He always gives me a lot of thoughtfully cosmological or physical statements for my studies. In particular, in our laboratory seminars I have given presentations, he always has caused me to essential questions and discussions for my studies. Also I am grateful to Lecturer, Atsushi J. Nishizawa, who is a superviser for me in actual, which has definitely guided me in the next step in difficult situations with several aspects not only for a technical side in our work, but also for my mental health. All of those have led me to the next stage that is substantially important in my life. Further I would like to thank Professor Naoshi Sugiyama. He has helped all Ph.D students' activities with respect to our researches, including financial assistance, nevertheless he is always pressed by business. Next, I deeply appreciate great numerous supports by all collaborators, Oscar Macias, Masahiro Takada, Kohei Hayashi, Masao Shirasaki, Shin'ichiro Ando, Shunsaku Horiuchi, Hiroyuki Tashiro and Masamune Oguri. All of my studies are based on all of your great support, again. Also, staffs of my laboratory including who already have gone to other academies or institutes, I thank all of you for kind and helpful discussion. The work for this thesis is publicly supported by Research Fellow of the Japan Society for the Promotion of Science No.20J11682. For all of students having involved with me, thank you for giving me really different supports in my Ph.D sudent days. And finally, I am grateful to my parents for supporting me in both financial and health over many years not only this term of the Ph.D course.

Contents

Abstract

Revealing the nature of dark matter (DM) has been one of biggest issues in astrophysics and particle physics for several decades. Weakly interacting massive particle (WIMP) is one of the most theoretically motivated candidates of DM. WIMPs are expected to produce γ-ray photons through interactions of the WIMP-pair annihilation into standard model particles and their cascade processes. Therefore, one can search the annihilating DM nature via signal probes with cosmic γ-ray observations. In recent years, the DM annihilation signal has been explored by γ-ray observations, mainly, using the Fermi Large Area Telescope (LAT) data. In those searches, the cross correlation between highly DM dominated and massive structures, such as galaxies and galaxy clusters, with observed photons in the direction of the structures, has provided constraints on the annihilation rate.

In this thesis, we investigate one of the desirable targets, low surface-brightness galaxies (LSBGs), which have significant features for the DM cross-section probe as follows. LSBGs are highly DM dominated systems, and their halo masses are relatively massive. The annihilation probe with LSBGs is expected to be robust, because they have less astronomical γ-ray contamination, and the angular size of a typical LSBG is much smaller than the angular resolution of the *Fermi*-LAT, whose γ-ray data are used in our analysis. Further, large volumes of LSBGs are likely to be in the local universe, which supports a statistical approach with stacking objects to the signal probe. However, there is a disadvantage that the redshifts of most LSBGs are unknown; nevertheless, we need object redshifts to build the flux models of γ rays originated that originated from the DM annihilation within each object.

In our analysis, instead of measuring individual redshifts, we measure the redshift distribution dN/dz of the overall LSBG catalog using the clustering redshift method. Then, we randomly assign redshifts to each LSBG from the distribution to calculate the γ-ray flux from the annihilation. Finally, we perform a composite likelihood analysis with the flux models of individual LSBGs and the observed γ-ray flux to provide an upper limit on the annihilation cross-section. In the likelihood analysis, we assume all parameters of LSBG's flux models to be independent of each other to reduce the computational cost.

In this thesis, we employ the *Fermi*-LAT photon data in addition to two LSBG catalogs, which are produced from the Hyper Suprime-Cam (HSC) and Dark Energy Survey (DES) data. First, in the analysis with the HSC-LSBG catalog (including ∼800 objects), we find that it is sufficient for the cross-section constraint to use dN/dz of the overall samples with unknown redshifts. We also find that the upper limit decreases with the number of stacked objects. Next, we probe the cross section with the DES-LSBG catalog (including ∼24,000 objects) and provide the upper limit with 95% C.L. of $\sim 3\times10^{-25}$ [cm^3/s] at DM mass of 100 GeV. To be conservative in our analysis, we remove $\sim$ 30% LSBGs ($\sim$ 7000 obejcts) within 1° from bright point-like sources, because there can be mismodeling of the γ-ray background flux around these sources. We find that the upper limit with the limited sample is $\sim$ 30% weaker than the one with the full sample in all energy ranges, which follows the scaling relation we found in the analysis using the HSC-LSBG catalog. Consequently, in this analysis, the artificial effect due to the mismodeling is not found.

Currently, the upper limit with all the DES LSBGs is an order of magnitude weaker than the canonical cross-section (3×10^{-26} [cm^3/s]) at DM mass of 100 GeV, nevertheless, in the future we expect to discover $\mathcal{O}(10^5)$ LSBGs in surveys with next-generation telescopes, like the Legacy Survey of Space and Time. The cross-section constraint with these LSBGs can be a few order of magnitudes more stringent than our findings. Therefore, the indirect DM search with the joint analysis of large amounts of LSBGs should be significant presence in the next decade.

Chapter 1

Introduction

1.1 Evidence and candidates of dark matter

Revealing the nature of dark matter (DM) is a challenging issue in modern astrophysics and cosmology as well as particle physics. In the context of astrophysics, all structures in the universe, such as galaxies and galaxy clusters, is affected by DM with gravitational interactions; thus, it is significant for understanding the formation and evolution of these structures to reveal the DM nature. Moreover, it has been clarified that DM particles rarely interact with the standard model (SM) particles by numerous astronomical observations and experiments, which strongly indicate the existence of a framework beyond the SM.

The DM search began in the 1930s through observations of member galaxies of several galaxy clusters. Zwicky [1933] searched scatters of apparent velocities of member galaxies in various galaxy clusters and found several galaxies had large scatters above ~ 2000 k/m in the Coma cluster. He employed the virial theorem to estimate the cluster mass and concluded the mass-to-light ratio of the cluster was at least 400 with an assumption of a Hubble constant H_0 of 558 [km s^{-1}Mpc^{-1}]; if $H_0 = 70$ [km s^{-1}Mpc^{-1}], the ratio is ~ 60. This result raised questions of whether well-known visible and invisible components, such as cool or cold stars and gases, satisfy the estimated cluster mass[1]. Rubin and Ford [1970] searched the circular velocities of stars and small patch H-II regions in M31. They

[1]In Zwicky [1933], Zwicky first used the phrase *dark matter*

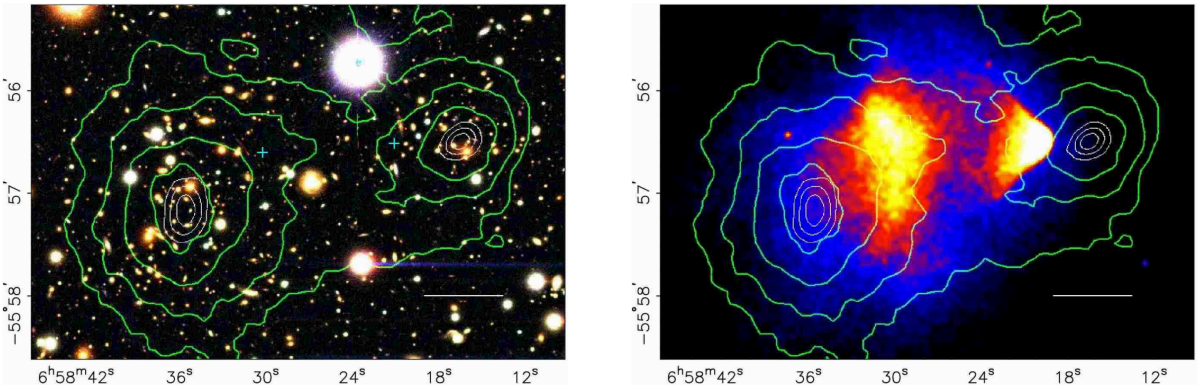

FIGURE 1.1: (*Left*) Optical color image from the Magellan observation. (*Right*) X-ray emission from the Chandra image. Green contours in both panels represent the weak lensing signal κ, which is 0.16 at the outermost contour and increases by 0.07 for each step. The white bar indicates a physical scale of 200 kpc. (Adapted from Figure 1 in Clowe et al. [2006]).

found that the velocity radial profile is a flat shape at the outer regions of the galaxy spiral plane, which differed from an expected result from observations of the visible matter profile with the Keplerian dynamical behavior. This led to the hypothesis of the existence of abundant DM[2].

Among numerous studies to clarify the existence of DM, Clowe et al. [2006] studied a single merger of galaxy clusters (often referred to as the *bullet cluster*) and provided well-known visible evidence for the existence of DM (Figure 1.1). They showed the visible difference between DM and SM particles as a significant difference in spatial distributions of the weak lensing signal comprising the DM density field and X-ray emission from hot baryonic matters. This discordance implies that the mass distribution does not trace the baryon density field and strongly supports the necessity of abundant nonbaryonic matter - DM. The Bullet cluster also tells us that DM is collisionless matter and the self-interaction cross-section of DM per unit mass is $\sigma/m_\chi < 1.25$ [cm^2/g] [Randall et al., 2008].

In the past few decades, numerous studies to realize substantive DM properties have been conducted. The cosmic microwave background anisotropy has played a significant role in estimating the DM cosmic abundance ($\Omega_{\rm DM} \sim 0.120h^{-2}$ with $h \sim 0.674$ in Planck Collaboration et al. [2018]) and other cosmological parameters. In several cosmological

[2]See Bertone and Hooper [2018] for more details for the history of the DM search.

probes with large-scale structures, gravitational lensing, and supernovae observations, the DM abundance has been estimated, and the results are consistent [e.g., Pike and Hudson, 2005, Hikage et al., 2019, Holanda et al., 2019, Sugiyama et al.]. Considering the free-streaming scale of DM, three types of species are DM candidates: cold DM (CDM), warm DM (WDM), and hot DM (HDM). Indeed, they have different velocity dispersions at the freeze-out time; CDM is non-relativistic, HDM is relativistic, and WDM is has the medium state of the CDM and HDM velocities. The time evolution of the matter structures is affected by the DM density field through the gravitational interaction. Therefore, the cosmic structure formation in different scales reflects the information about the nature of DM, which enables us to restrict DM natures by observations of cosmic structures.

From the matter power spectrum analysis, HDM, which is thermal light DM such as neutrinos, has been excluded from the dominant DM candidates [Kuhlen et al., 2012]. For example, the present abundance of neutrino $\Omega_{\nu 0}$ is given as $\Omega_{\nu 0} h^2 \sim \sum m_\nu / 94[\mathrm{eV}]$, where $\sum m_\nu$ is the sum of neutrino masses of all flavors with an upper limit of 0.12 eV [Planck Collaboration et al., 2018]; thus $\Omega_{\nu 0} \lesssim 0.002$. As a representative WDM candidate, there is a sterile neutrino model, which interacts with SM particles through only gravitational interactions (no electroweak interaction) and has a typical mass of keV scale. See detailed discussion in a recent review [Dasgupta and Kopp, 2021]. In WDM searches, the strongest bounds on the mass scale of DM have been obtained by observations of the Lyman-α forest (see recent probes in Baur et al. [2017], Murgia et al. [2018]).

Although the possibility of WDM as a dominant component of DM has not been ruled out, here, we consider CDM, which has several well-motivated candidates, such as a primordial black hole (PBH) [Carr et al., 2016, Sasaki et al., 2018], axions [Sikivie, 2008, Marsh, 2016], and weakly interacting massive particle (WIMP). PBHs are formed in the very early universe in extremely dense matter clumps. Their masses are at least higher than $\sim 10^{-18}\ M_\odot$ because PBHs with lower masses than the bound cannot exist in the present universe due to the black-hole evaporation. In more massive regime, the fraction of PBH in the DM abundance has been constrained by various probes, such as lensing surveys in the Milky Way (MW), 21-cm radio surveys, gravitational-wave experiments, and CMB observations. However, there are remain open windows for PBHs to be above $\sim 10\%$ of the DM fraction for PBH masses of $\sim 10^{-16}\ M_\odot$ and $\sim 10^{-11}\ M_\odot$-$\sim 10^{-13}\ M_\odot$ [Katz

et al., 2018]. Axions, produced non-thermally in the early universe, are pseudo-Nambu-Goldstone bosons with a Peccei-Quinn symmetry, which were originally considered to solve the strong CP problem in quantum chromodynamics (QCD). The QCD axion mass depends on the breaking scale f_a of the symmetry, $m_a \sim 0.6$ meV$(10^{10}$ GeV$/f_a)$ and if $m_a \sim 10^{-5}$ eV, the axion abundance explains all of the DM fraction. The term "axion" is often used in more general sense and can refer to ultralight pseudo-scalar field with two parameters of m_a and f_a. The parameter space has been explored by observations, such as the CMB temperature anisotropy, large-scale structures, reionization of intergalactic medium, and halo density profiles [Marsh, 2016]. In this thesis, we focus on WIMPs as a DM candidate.

1.2 WIMP and pair-annihilation

One of the most theoretically well-motivated DM candidates of a thermal relic is weakly interacting massive particle (WIMP), which is considered as heavy particles in supersymmetric extensions of the SM with a mass scale from GeV to TeV[3]. They are expected to be produced in thermal equilibrium with the SM particles in the early universe, and nonrelativistic particles at the freeze-out of thermal equilibrium; thus, they are regarded as CDM particles. The present DM abundance depends on the freeze-out time of WIMPs, which is determined by the annihilation rate and DM mass. This particle nature is essential for DM indirect searches with astronomical observations. In WIMP-pair annihilation into SM particles, SM particles such as quarks, leptons, and gauge bosons are produced as the final states. Because these massive SM particles are unstable, they decay into more stable particles, and then photons, electrons, and neutrinos are emitted in the end. Therefore, one can search the annihilating DM nature by the signal probe of the stable more particles. WIMPs are expected to produce γ-ray photons through interactions of the WIMP-pair annihilation into SM particles and cascade processes of them. Thus, one can search the annihilating DM nature via signal probes with cosmic γ-ray observations. In recent years, the γ-ray signal of the DM annihilation has been searched by observations such as those represented by the Fermi Large Area Telescope (LAT). In those searches, the cross-correlation between highly DM dominated structures with observed

[3]The lightest model of WIMP is called neutralino, which consists of four species of supersymmetric particles of the bino, neutral wino, and neutral higgsinos.

photons in the direction of the structures, has been provided constraints on the annihilation rate. In general, WIMP mass is considered to be from 2 GeV (the so-called Lee-Weinberg bound [Lee and Weinberg, 1977]) to ∼100 TeV (unitary bound [Griest and Kamionkowski, 1990]); hence, we can detect WIMPs within this limited mass range, or rule them out from DM candidates to provide a stringent upper limit on the annihilation rate because the present DM abundance scales with an inverse of the annihilation rate, and then exists the rate to explain the present DM abundance.

For WIMP searches, there is two types of complementary probes in addition to the indirect search for the annihilation signal: the direct detection of DM scattering signals and pair-production of DM with colliders. The direct detection experiments explore the scattering signal of DM with nuclei in detectors. The nuclear recoil by the scattering can induce scintillation photons from excitation of nuclei, ionization of atoms in a target material, and production of phonons in the detectors; thus, we can directly detect DM particles by detecting these measurable quantities. As one of such experiments, there is the DAMA/LIBRA experiment, in which an annually modulated DM-like signal with the significance at the level of 9.3σ has been reported [Bernabei et al., 2013]. The estimated DM-mass range is 10-15 GeV or 60-100 GeV. However, results from other experiments, such as XENON1T, PandaX-II, and XMASS, have excluded that the annual modulation is interpolated by the effect of the velocity dispersion of DM particles [Xenon Collaboration, 2017, XMASS Collaboration, 2015].

To search for the pair-creation of DM particles, collider experiments such as ones in the Tevatron, Large Electron-Positron Collider, and Large Hadron Collider (LHC), have been conducted. In the experiments, one should miss a part of the total energy of the pair-creation event because one cannot detect DM due to DM particles being neutral and stable. Therefore, measuring the visible counterpart of the event, such as charged leptons and photons, which is generally referred to as mono-X searches standing for searches for the WIMP production in association with one or more QCD jets or other SM particles of γ, h, and Z [CMS, 2016, Atlas Collaboration, 2016]. As other searches, there are searches for invisible Higgs decay and Z decay [ATLAS Collaboration, 2015, Patrignani et al., 2016].

1.3 Indirect DM searches for annihilation signal

Astronomical objects, such as galaxies and galaxy clusters, are highly DM dense and extremely massive systems. Thus, in a few decades, these objects have been used in indirect searches for DM annihilation with observations of the cosmic γ ray, X-ray, radio emission, and neutrinos. In particular, in the last decade, γ-ray data by the *Fermi* LAT has been used in most probes. LAT is a γ-ray detector on boarding the Fermi Gamma-Ray Space Telescope, which was launched on June 11, 2008, and has observed the whole sky from 20 MeV to 1 TeV. Numerous γ-ray sources have been detected in LAT experiments, containing pulsars and supernova remnants in our Galaxy as well as the extragalactic sources of blazars, star-forming galaxies, radio galaxies, and active galactic nuclei (AGNs). The LAT Collaboration produced the most recent source catalog (the fourth catalog) [Abdollahi et al., 2020] which contains over 5,500 sources resolved at a detection level of above 4σ. More than 3,700 counterparts have been found or associated with those γ-ray sources.

Moreover, unresolved diffuse components of cosmic γ rays have been detected. It is crucial for the DM-signal probes to reveal the origin of these components, because these γ-ray photons that originated from the DM annihilation cab be contained. Therefore, these components allow us to probe signals with various DM-dense astronomical objects. In practice, objects within Milky Way (MW) halos or in the local universe are selected in most studies, because the predicted flux of γ rays produced in the DM annihilation process decreases inversely proportional to the square of the distance.

As one of the unresolved components, there is an excess emission at the galactic center region at an energy of a few GeV, whose detection has been reported by several groups [e.g., Petrović et al., 2014, Ajello et al., 2016, Ackermann et al., 2017]. The excess is considered to include γ-ray photons from a series of burst events, and unresolved millisecond pulsars in addition to the DM annihilation. Exploring the unknown excess emission can enable us to provide a stringent annihilating-DM constraint because one expects the significantly luminous γ-ray flux from the DM annihilation due to the Galactic center region being extremely DM dense and close to us [e.g., Hooper and Goodenough, 2011, Gordon and Macías, 2013, Ackermann et al., 2017, Abazajian et al., 2020]. However, there is a large systematic uncertainty of accumulated emissions from the astronomical unresolved sources as well as the DM density profile of the MW core. Therefore, it is very

challenging to perform robust DM searches with γ-ray observation towards the Galactic center region. In addition, with observed γ-ray emission from the Galactic halo without the galactic center region, the MW globular clusters and halo have been used as target objects [e.g., Hurst et al., 2015, Chang et al., 2018, Wirth et al., 2020].

For indirect searches with extragalactic objects, the unresolved γ-ray background (UGRB) and extragalactic γ-ray background (EGB) are usually considered. UGRB contains residual photons extracted by the subtraction of the galactic diffuse and all resolved-source emissions from the observed photon flux. Meanwhile, EGB includes both UGRB photons and the resolved extragalactic source emission. The two backgrounds can include photons that originated from the DM annihilation within extragalactic objects; accordingly, those have been studied to probe the DM signal by combining several low-redshift galaxies, galaxy groups, and galaxy clusters [e.g., Ando et al., 2014, Ackermann et al., 2015a, Lisanti et al., 2018, Thorpe-Morgan et al., 2021].

The galactic and extragalactic targets have numerous γ-ray sources of astronomical origins. For the robustness of faint DM-signal probes, it is imperative to avoid the contamination of γ-ray photons from astronomical sources in target objects. The search for the annihilation-induced γ-ray emission from MW dwarf spheroidals (dSphs) enables robust annihilation probes, because MW dSphs are expected to have quiescent star-formation activities [Albert, A. et al., 2017, Gammaldi et al., 2018, Hoof et al., 2018, Boddy et al., 2018, Hoof et al., 2020]. Thus, MW dSphs have less astronomical γ-ray emission from star-formation regions, such as pulsars and supernova remnants. Using 27 MW dSphs, Hoof et al. [2020] have obtained the most robust and relatively stringent upper limit on the DM annihilation cross-section to be $\sim 3 \times 10^{-26}$ [cm^3/s] at a 100 GeV DM mass with 95% C.L.[4], which is comparable to the canonical cross-section. In Figure 1.2, we show various upper limits on the DM cross-section using the MW dSph, galactic center region, galactic halo, and galaxy groups.

[4]In accordance with convention, we call the ensemble average of the product of the DM velocity dispersion and DM annihilation cross-section, $\langle \sigma v \rangle$, the "DM cross-section" throughout this thesis.

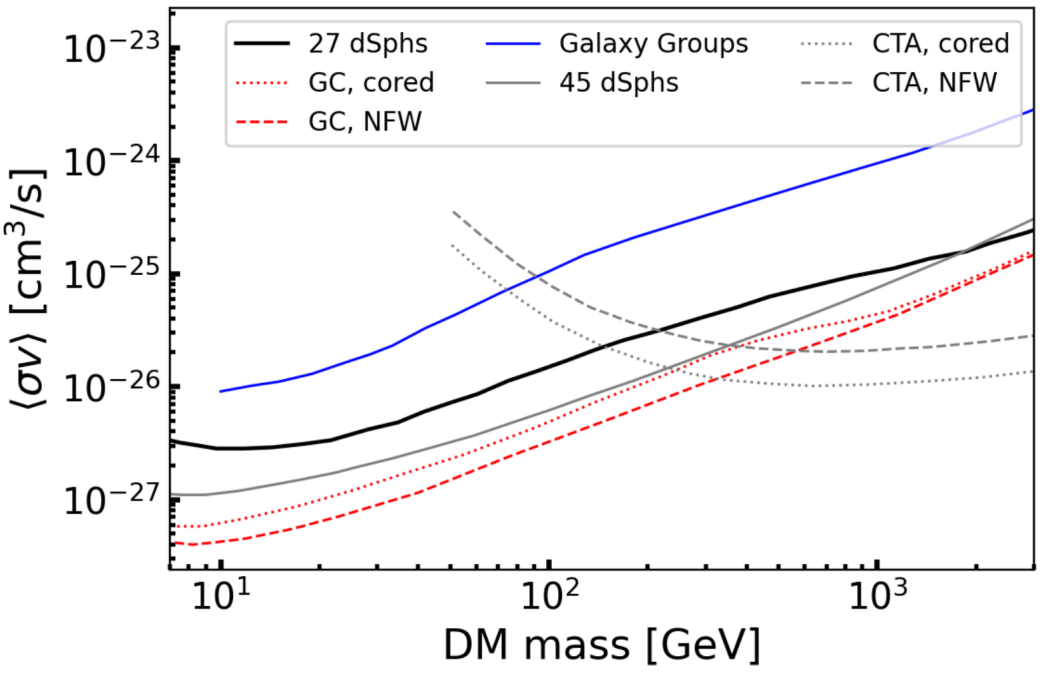

FIGURE 1.2: Current upper limits on the DM cross-section with 95% C.L using observations of the Fermi-LAT in all plots except for the gray dotted and dashed lines, and Cherenkov Telescope Array (CTA) in the remaining two plots. The black and blue lines represent the upper limits with 27 dSphs and the local galaxy groups, respectively [Hoof et al., 2020, Lisanti et al., 2018]. The red dotted and dashed lines are upper limits using the galactic center region, assuming the Einasto and NFW profiles, respectively [Abazajian et al., 2020]. The gray dotted and dashed lines represent predicted upper limits with the CTA observation using the Galactic halo assuming the Einasto and NFW profiles, respectively [Carr et al., 2015]. The gray solid line is a prediction with 45 dSphs and the 15-year LAT data [Charles et al., 2016].

1.4 Our strategy

In this thesis, we focus on low surface brightness galaxies (LSBGs) [Impey and Bothun, 1997] as a target object for the DM annihilation probe, which has some advantages as follows. First, LSBGs are highly DM dominant systems [Di Paolo et al., 2019], and their DM halos are at least an order of magnitude more massive than those of the Milky Way dSphs [Prole et al., 2019]. Moreover, LSBGs are relatively quiescent in astronomical γ rays because of having fewer γ-ray emitters such as pulsars, supernova remnants, and active galactic nuclei [Cao et al., 2017]. In addition, an angular size of a typical LSBG is much smaller than the point-spread function (PSF) of *Fermi*-LAT in all γ-ray energy

ranges. Accordingly, the annihilation probe with LSBGs is expected to be less systematic uncertainty. Finally, large amounts of LSBGs are likely to reside in the local universe (the object count fraction in the local universe is at least 30% [Trachternach et al., 2006]), which shows that the joint analysis with LSBGs can be a powerful method to constrain the DM cross-section.

However, using LSBGs has a limitation. Most LSBGs do not have known redshifts, which is required to model the γ-ray flux induced by the annihilation from an object, in addition to the DM density profile and total DM mass of the object. The lack of the redshift information is because most LSBGs have very faint surface brightness and diffuse structures; consequently, it is difficult to measure their spectroscopic redshifts and estimate their precise photometric redshifts. So far, there are a few studies for the annihilation signal using known-redshift LSBGs with radio or γ-ray observations [Hernández Cadena et al., 2017, Gammaldi et al., 2018, Bhattacharjee et al., 2021], including one of our studies [Hashimoto et al., 2020].

In our main study in this thesis, we present a method to perform the DM signal probe using numerous LSBGs with unknown redshifts. To do so, we assign redshifts to each object using the redshift distribution dN/dz of the overall object sample, instead of measuring individual redshifts. For dN/dz measurement, we apply the clustering redshift method [Newman, 2008, Ménard et al., 2013], which relies on spatial clustering of astronomical objects affected to each other through the gravitational interaction. To extract the clustering information, we measure the angular cross-correlation of an LSBG sample with a spectroscopic redshift (spec-z) sample as a reference sample. With the redshift-binned reference samples, we obtain the cross correlations in different redshift bins and convert from the correlation amplitudes to dN/dz amplitudes. Then, we randomly assign redshifts to individual LSBGs from the measured dN/dz and model their annihilation γ-ray fluxes with the DM cross-section as a parameter, by estimating the halo mass of LSBG as well as assuming the spectral energy distribution of a single annihilation event and DM density profile. For the model flux of a single object, this redshift assignment introduces a large uncertainty, resulting in a large uncertainty for the constraint on the cross section. However, in the joint analysis with numerous LSBGs, the statistical uncertainty would be dramatically suppressed.

In this thesis, we use the *Fermi*-LAT photon data and two LSBG catalogs. One of these catalogs is produced from optical survey data (g, r, and i bands) by the Subaru Hyper Suprime-Cam Subaru Strategic Program (HSC-SSP) and contains 781 objects of the effective surface brightness > 23.4 [mag/arcsec^2] in g-band with a sky coverage of ~ 200 deg^2 [Greco et al., 2018a]. By performing the composite likelihood analysis using this LSBG sample and the LAT photon data, we will validate our above procedure. In other words, we confirm whether it is sufficient for the DM cross-section constraint to use the redshift distribution of the overall sample instead of the individual object redshifts. For the reference sample in dN/dz measurement, we use the spec-z sample from NASA Sloan Atlas (NSA) [Blanton et al., 2011] in fully overlapping areas with the HSC survey region. Further, in the likelihood analysis, we find a scaling relation between the number of LSBGs and the constraint on the DM cross-section, which is significant for the future DM constraint with LSBGs that are potentially abundant.

To reduce the computational cost for the composite likelihood analysis with numerous objects, we assume that all the parameters included in LSBG γ-ray flux models for the DM annihilation are independent of each other. Actually, the mean angular separation of our LSBGs is $\sim 0.5^\circ$, which is comparable to the LAT PSF ($0.1^\circ < \theta < 1.5^\circ$ in the energy range we considered). Accordingly, we may need to consider a correlation between flux-model parameters of neighboring LSBGs in our likelihood analysis. Hence, we need to verify this assumption when performing our procedure.

The other LSBG catalog is produced by the Dark Energy Survey (DES) Collaboration and is the largest LSBG catalog at present, including $23,790$ objects of the effective surface brightness > 23.2 [mag/arcsec^2] in g-band with a sky coverage of $\sim 5,000$ deg^2 [Tanoglidis et al., 2021]. We perform the composite likelihood analysis with all DES-LSBGs to provide a constraint on the cross section with the unknown-redshift objects. In addition, we will consider further analyses to better understand our procedure and the results with respect to the UGRB construction. As mentioned in [Ackermann et al., 2015b], the putative flux of a faint source such as LSBG is fairly sensitive to variability of flux model parameters of bright sources in a region of interest (ROI) as well as resolved sources around the objects of interest. Accordingly, after constructing UGRB field by the maximum likelihood runs with all model parameters of flux models of all diffuse and resolved sources, we will perform a recalibration of only bright and adjacent resolved-source parameters around the LSBG position. Then, we will compare DM cross-section constraints using the UGRB

flux with and without the recalibration process. Further, for conservation of our analysis, we will consider LSBGs except for objects within 1° from resolved sources, which is $\sim 30\%$ of the total sample, because UGRB fluxes around the sources can be under-estimated due to the incompleteness of source parameter optimization, which can lead to a suspiciously strong DM constraint.

The rest of this thesis is organized as follows. In Chapter 2, we revisit a summary of WIMP DM with respect to DM abundance in the universe and the annihilation cross-section. In addition, we describe the model of γ-ray flux from the DM annihilation within astronomical objects. In Chapter 3, we summarize recent indirect searches for the DM annihilation signal with γ-ray observations. In Chapter 4, the properties of our target objects, LSBGs, are described. In Chapter 5, the datasets used in our analyses (two LSBG catalogs, LAT photon data, and spec-z samples) are described. In Chapter 6, we probe the annihilation cross-section with individual HSC LSBGs with known redshifts and describe details for γ-ray flux modeling for the annihilation within LSBG halos and the composite likelihood analysis with multiple objects. In Chapter 7, first, we perform a validation check for our procedure in which we use the redshift distribution estimated using the clustering redshift method, instead of individual object redshifts, including underlying assumptions. Next, we provide the upper limit on the cross section with all DES LSBGs as the final result. Finally, as concluding remarks, we summarize this thesis and describe future prospects in Chapter 8.

Chapter 2

Dark Matter Annihilation

2.1 Annihilation rate and thermal relic abundance of DM

First, we review a relation between the DM annihilation cross-section and CDM abundance at present in underlying assumptions. We start from the Boltzmann equation for CDM χ and SM particles X using the geodesic equation,

$$p^\alpha \frac{\partial f(x,p)}{\partial x^\alpha} - \Gamma^\alpha_{\beta\gamma} p^\alpha p^\gamma \frac{\partial f(x,p)}{\partial p\alpha} = C[f], \tag{2.1}$$

where $f(x,p)$ is the phase space distribution at the space-time position x and 4-momentum p. Γ and $C[f]$ are the Christoffel symbols and collision term, respectively. Under an assumption of the isotropic and homogeneous universe, $f(x,p) = f(E,\mathbf{x})$. Then, Equation 2.1 is rewritten as,

$$E\frac{\partial f}{\partial t} - H|\mathbf{p}|^2 \frac{\partial f}{\partial E} = C[f], \tag{2.2}$$

where $|\mathbf{p}|^2 = E^2 - m^2$. We denote the number density of a particle n as follows,

$$n(t) = g \int \frac{d^3p}{(2\pi)^3} f(E,t), \tag{2.3}$$

where g is the internal degrees of freedom. Equation 2.1 is rewritten as follows,

$$\frac{dn}{dt} + 3Hn = g\int \frac{d^3p}{(2\pi)^3}\frac{C[f]}{E}, \tag{2.4}$$

Here, we consider the number density of DM particles when DM annihilate into SM particles, $\chi + \bar{\chi} \to X + \bar{X}$ and set the following assumption. 1) There is no asymmetry between χ and $\bar{\chi}$, 2) X and $\bar{X}$ have zero chemical potential with thermal equilibrium, 3) this interaction has the time-reversal symmetry, and 4) $f_i = \exp[-(E_i - \mu_i)/T]$ and $f_i = \exp[-(E_i)/T]$ for DM and SM particles, respectively; thus, $n_i = e\mu_i/Tn_i^{eq}$, where $n_i^{eq} = \int \frac{gd^3p}{(2\pi)^3}e^{-E_i/T}$. Then, the right-hand side of Equation 2.4 is expressed as follows,

$$g\int \frac{d^3p_\chi}{(2\pi)^3}\frac{C[f]}{E_\chi} = -\int d\Pi_\chi d\Pi_{\bar{\chi}} d\Pi_X d\Pi_{\bar{X}} (2\pi)^4\delta^4(p_\chi + p_{\bar{\chi}} - p_X - p_{\bar{X}})|\mathcal{M}_{\chi\bar{\chi}\to X\bar{X}}|^2(f_X f_{\bar{X}} - f_\chi f_{\bar{\chi}}), \tag{2.5}$$

where $\Pi = gd^3p/((2\pi)^3 2E)$ for each species. $\mathcal{M}_{\chi\bar{\chi}\to X\bar{X}}$ is the scattering amplitude, which is averaged over spins and includes symmetry factors for identical particles. Considering the energy conservation and zero chemical potential for X and $\bar{X}$,

$$f_X f_{\bar{X}} - f_\chi f_{\bar{\chi}} = [e^{\mu_X + \mu_{\bar{X}}} - 1]e^{-(E_\chi + E_{\bar{\chi}})/T}. \tag{2.6}$$

Then, defining the DM annihilation cross-section as follows,

$$\langle\sigma v\rangle \equiv \frac{1}{n_{\chi^2}^{eq}}\int d\Pi_\chi d\Pi_{\bar{\chi}} d\Pi_X d\Pi_{\bar{X}} (2\pi)^4\delta^4(p_\chi + p_{\bar{\chi}} - p_X - p_{\bar{X}})|\mathcal{M}_{\chi\bar{\chi}\to X\bar{X}}|^2 e^{-(E_\chi + E_{\bar{\chi}})/T}, \tag{2.7}$$

we obtain the time evolution of the DM number density using Equations 2.4, 2.5, and 2.6,

$$\frac{dn_\chi}{dt} + 3Hn_\chi = -\langle\sigma v\rangle(n_\chi^2 - (n_\chi^{eq})^2). \tag{2.8}$$

Here, we assume the cross section having no dependence on the temperature (or the velocity of DM particles)[1] and apply the following definitions of $x \equiv m_\chi/T$, $Y \equiv n_\chi/s$, and $Y_{eq} \equiv n_\chi^{eq}/s$, where s is the entropy density per physical volume. Due to the conservation law of entropy in the comoving volume S, $S = sa^3 = (2\pi^2/45)g_{s*}T^3 =$

[1]Otherwise, the cross section can be expanded as $\langle\sigma v\rangle = a_0 + a_1 T + \mathcal{O}(T^2)$, or $\langle\sigma v\rangle = a_0 + a_1\langle v\rangle^2 + \mathcal{O}(\langle v\rangle^4)$, where a_0 and a_1 are independent from the temperature and the velocity dispersion, but depend on the DM mass. The first and second terms of the right-hand side are called s-wave and p-wave, respectively. However, the expansions are not valid in some cases, such as annihilations through the resonant exchange of an s-channel mediator [Griest and Seckel, 1991].

$(2\pi^2/45)g_{s*}m^3/x^3 = \text{const}$. Then, in the radiation-dominated era, Equation 2.8 is rewritten as follows,

$$\frac{dY}{dx} = \frac{s\langle\sigma v\rangle}{Hx}(Y_{eq}^2 - Y^2). \tag{2.9}$$

Further, from $H = \sqrt{\frac{4\pi^3 g_*}{45}}\frac{m_\chi^2}{m_{\rm Pl}x^2}$, where $m_{\rm Pl}$ is the planck mass,

$$\frac{dY}{dx} = \sqrt{\frac{\pi}{45}}\frac{g_{*s}}{\sqrt{g_*}}m_{\rm Pl}m_\chi^2(Y_{eq}^2 - Y^2). \tag{2.10}$$

The temperature of the universe is representative by the temperature of photon T_γ, i.e., $T \equiv T_\gamma$. The effective degree of freedom for the energy density is written by,

$$g_* = \sum_B g_B\left(\frac{T_B}{T_\gamma}\right)^4 + \frac{7}{8}\sum_F g_F\left(\frac{T_F}{T_\gamma}\right)^4, \tag{2.11}$$

where subscripts B and F denote bosons and fermions with their temperatures of T_B and T_F, respectively. A factor of $\frac{7}{8}$ comes from the difference of statistics of bosons and fermions. Similarly, The effective degree of freedom for the entropy density is defined as follows,

$$g_{s*} = \sum_B g_B\left(\frac{T_B}{T_\gamma}\right)^3 + \frac{7}{8}\sum_F g_F\left(\frac{T_F}{T_\gamma}\right)^3. \tag{2.12}$$

If all particles are in the thermal equilibrium, then $T = T_B = T_F$ and the entropy density is identical to the energy density. Due to the conservation law of entropy in the comoving volume S, $S = sa^3 = (2\pi^2/45)g_{s*}T^3 = (2\pi^2/45)g_{s*}m^3/x^3 = \text{const}$.

To discuss the relation of the relic abundance and the DM freeze-out time, we consider the annihilation rate in the universe, $\Gamma_A \equiv n_\chi^{eq}\langle\sigma v\rangle$. Then, Equation 2.9 is modified as,

$$\frac{x}{Y_{eq}}\frac{dY}{dx} = -\frac{\Gamma_A}{H}(\frac{Y^2}{Y_{eq}^2} - 1). \tag{2.13}$$

In Figure 2.1, we show a numerical result from Equation 2.13, which indicates that the relic DM abundance hardly depends on the DM mass, but depends on the annihilation cross-section. For $\Gamma_A/H \gg 1$, $Y \approx Y_{eq}$ and for $\Gamma_A/H \ll 1$, the DM number density hardly changes and leads to the DM abundance at the present. We define

$\lambda \equiv m_{\rm Pl} m_\chi \sqrt{\pi/45} \langle \sigma v \rangle g_{s*}/\sqrt{g_*}$ and modify Equation 2.10 as follows,

$$\frac{dY}{dx} = -\frac{\lambda}{x^2}(Y^2 - Y_{eq}^2). \tag{2.14}$$

When $x \to \infty$, then $Y \gg Y_{eq}$ and Equation 2.14 is approximately,

$$\frac{dY}{dx} \simeq -\frac{\lambda}{x^2} Y^2. \tag{2.15}$$

Therefore, integrating this equation from $x = x_f$, which is x at the freeze-out time, to $x = \infty$,

$$Y(\infty) \simeq \frac{x_f}{\lambda}. \tag{2.16}$$

Compering Equations 2.13 and 2.14, we derive $Y_{eq}(x_f)\lambda/x_f = 1$, and solving this equation, we obtain x_f, which is approximately,

$$x_f \simeq \ln\left[0.038 \frac{g}{g_*^{1/2}} m_{\rm Pl} m_\chi \langle \sigma v \rangle\right] + \frac{1}{2}\ln\left[\ln\left(0.038 \frac{g}{g_*^{1/2}} m_{\rm Pl} m_\chi \langle \sigma v \rangle\right)\right]. \tag{2.17}$$

Finally, using $Y(\infty) \approx Y_{eq}(x_f) = x_f/\lambda$, the cosmological density parameter of χ at the present is found as follows,

$$\Omega_{\chi 0} \approx 10^{-27} h^{-2} \frac{\sqrt{g_*}}{g_{s*}} x_f \left(\frac{\langle \sigma v \rangle}{\rm cm^3/s}\right)^{-1}. \tag{2.18}$$

Hence, we find the relic DM abundance, $\Omega_{\rm DM} = \Omega_{\chi\bar{\chi}0} = 2\Omega_{\chi 0}$, including the present abundance of χ and $\bar{\chi}$. To consider χ as one of DM components, the relic DM abundance provides an upper limit on the present abundance of χ, $\Omega_{\chi\bar{\chi}0} < 0.12h^{-2}$. As seen in Equation 2.18, This condition gives the lower limit on the DM cross-section. If the abundance of χ satisfies the total DM abundance, $\langle \sigma v \rangle \sim 3 \times 10^{-26}$ [cm^3/s] at a DM mass range of 100 GeV $\lesssim m_\chi \lesssim$ 10 TeV with $x_f \approx 25$ [Nihei et al., 2001]. Given the DM velocity dispersion at the freeze-out time to be $\sim 0.1c$, one obtains a cross section of weak strength for WIMP with mass around the electroweak scale. This coincidence has induced a fundamental motivation of the WIMP search.

For more precise canonical cross-section as a function of DM mass, Steigman et al. [2012] have revisited the thermal relic abundance calculation for a generic WIMP. For improvement of analytical treatments, they have considered the evolution of g_* and the mass

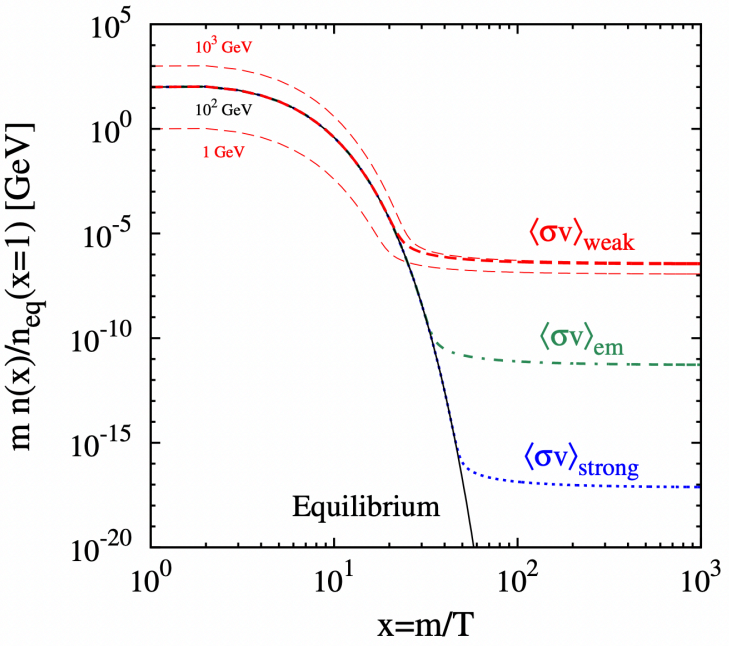

FIGURE 2.1: The DM abundance in the Universe as a function of a ratio of DM mass to temperature in the universe. The equilibrium number density (for DM mass of 100 GeV) with exponential dumping is represented in the black solid curve. The DM number density for weak interactions of $\langle\sigma v\rangle_{\rm weak} = 2 \times 10^{-26}$ cm^3/s (at 100 GeV) is shown in the thin red dashed line. The other two thick red lines are similar plots but for 1 TeV and 1 GeV from top to bottom. The abundance of electromagnetic ($\langle\sigma v\rangle_{\rm em} = 2 \times 10^{-21}$ cm^3/s) and strong ($\langle\sigma v\rangle_{\rm strong} = 2 \times 10^{-15}$ cm^3/s) interactions at DM mass of 100 GeV are represented in the dot-dashed and dotted lines, respectively. The plots are from Steigman et al. [2012].

dependence on g_*, x, and Γ/H, in addition to several simple improvements to the analytical approach. As shown in Figure 2.2, they have shown that for DM mass above ∼10 GeV, the precise cross section is $\sim 2.2 - 2.4 \times 10^{-26}$ [cm^3/s], and for lower than a few GeV, the value is $\sim 4 - 5 \times 10^{-26}$ [cm^3/s], while the canonical cross section is often set to 3×10^{-26} [cm^3/s] over all WIMP-mass range (from a few GeV to ∼10 TeV). Because DM masses lower than several tens GeV are excluded by current constraints with MW dSphs, the difference of the canonical cross-section in the traditional technique ($\sim 3 \times 10^{-26}$ [cm^3/s]) and that in this study is significant for the DM constraint.

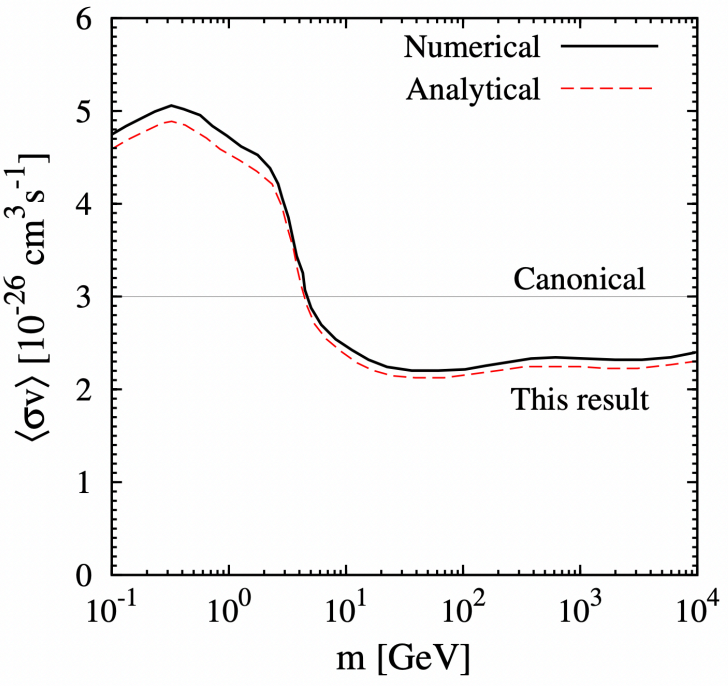

FIGURE 2.2: The thermal relic cross section as a function of DM mass for a Majorana WIMP. The solid and dashed curves are from a numerical result to consider the evolution of equation and from an approximate analytic solution, respectively. The horizontal line corresponding to $\langle \sigma v \rangle = 3 \times 10^{-26}$ cm^3/s. The cosmological DM abundance at present is assumed to $\Omega_\chi h^2 = 0.11$. This is appeared in Steigman et al. [2012].

2.2 γ-ray emission from DM annihilation

In the DM pair-annihilation into SM particles, γ rays are emitted in some cascade processes of massive species in the SM produced as one of the final states in the annihilation, rather than the photons produced directly in the annihilation. The final states are considered quarks, leptons, and gauge bosons such as $b\bar{b}, s\bar{s}$, $t\bar{t}, \tau^+\tau^-, \mu^+\mu^-, e^+e^-, W^+W^-$, and $g\bar{g}$. In the cascade processes, unstable particles decay into more stable species and finally emit γ-ray photons, electrons, positrons and neutrinos. Further, the more stable species induce secondary γ-ray photons by following two interactions. One is that the energetic e^+ and e^- cause the inverse-Compton scattering with radiation fields, and the other is that hadronic states interact with the interstellar medium, producing pions. Then, these interactions modify the electromagnetic spectral shape or amplitude in lower energy. Therefore, instead of searching a line spectrum of photons directly produced by

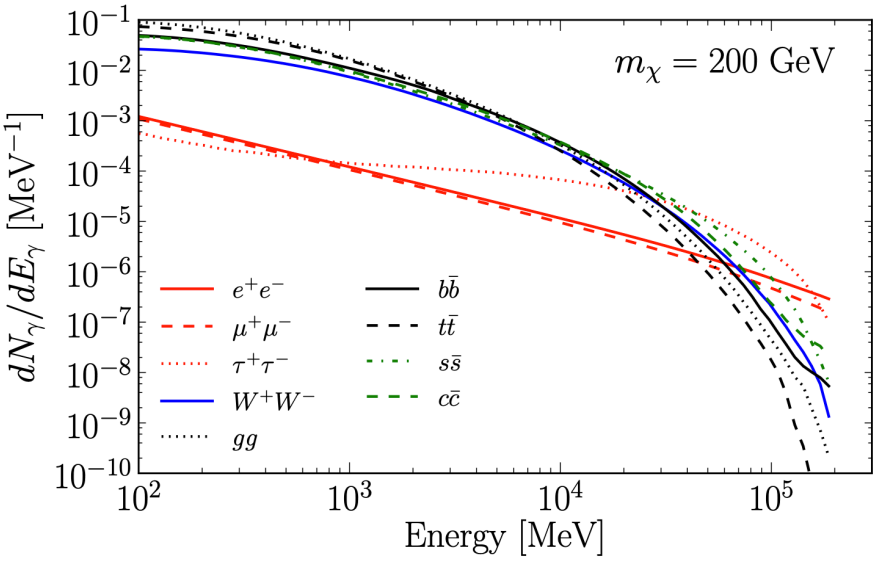

FIGURE 2.3: γ-ray spectra of different annihilation channels at DM mass of 200 GeV. These fluxes do not contain the secondary γ rays resulting from the inverse Compton scattering with charged particles produced by the annihilation process, such as e^+ and e^-. This figure is from Charles et al. [2016].

the annihilation, most indirect DM searches with cosmic γ-ray observations, including our works, have studies a continuous spectrum of γ rays resulting from cascade processes. The energy range of the γ rays has an upper bound corresponding to the DM mass, i.e., when the mass of the SM particle in the final state is equal to the DM mass.

2.3 Annihilation signal from astronomical objects

We derive the flux model of γ rays that originated from the DM annihilation and the cascade processes within astronomical objects. The flux model can be written as follows,

$$\frac{d\Phi_\gamma}{dE_\gamma} = J \times \frac{\langle \sigma v \rangle}{8\pi m_\chi^2} \sum_i Br_i \frac{dN_i}{dE'_\gamma}, \tag{2.19}$$

where dN_i/dE_γ and Br_i denote the differential spectrum of γ rays and the branching fraction in the i-th annihilation channel, respectively. J is the so-called J-factor, which includes all astrophysical features of the object, whereas, it contains no information on the particle physics of DM; it is defined by the integration of the squared DM density

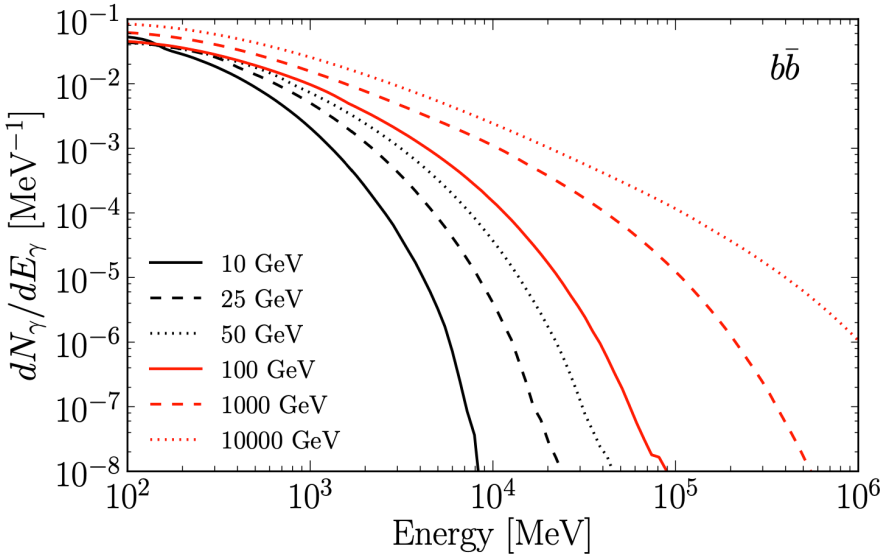

FIGURE 2.4: γ-ray spectra for the annihilation channel of $b\bar{b}$ at different DM masses. The plots do not include the secondary γ rays as in Figure 2.3. This figure is from Charles et al. [2016].

profile along the line of sight,

$$J = \int ds \int d\Omega \rho^2_{\rm DM}(s, \Omega), \tag{2.20}$$

where s and Ω are the line-of-sight vector and angular size of the halo, respectively. Other factors on the right-hand side of Eq. 2.19 are given by the particle physics nature of the DM candidate. In general, DM particles can self-annihilate in various final states. In our analysis, we consider an annihilation channel of $b\bar{b}$, which is a representative channel and benchmark to assess the sensitivity of the LAT to a putative DM signal from our search targets. The DM spectra are obtained using the `DMFIT` package Jeltema and Profumo [2008] provided within `fermipy`. The `DMFIT`[2] itself provides an interpolation to DM γ-ray spectrum tables extracted from `DarkSUSY` Bringmann et al. [2018].

[2] https://fermi.gsfc.nasa.gov/ssc/data/analysis/scitools/gammamc_dif.dat

Chapter 3

Current Constraints with γ-ray Sky

In this chapter, we describe indirect DM searches with astronomical γ observations, using DM-dense objects in the local universe, such as the MW center, halo and dSphs as well as the galaxy groups and clusters.

3.1 γ-ray components for DM indirect searches

The *Fermi*-LAT has observed cosmic γ-ray photons in the whole sky over 13 years and discovered natures of various astronomical γ-ray components (see descriptions for the instrument in Section 5.3). The emission is divided into the resolved source emission, the Galactic and isotropic diffuse emissions in addition to the residual emission that is obtained by subtracting the resolved and two diffuse emissions from the observed flux. Each component has been used in the indirect search for the DM annihilation signal. Before individual probes, we first describe these γ-ray components with the LAT observation.

3.1.1 Cataloged source emission

With continuous observation by the *Fermi*-LAT, the γ-ray source detection has been in progress, which is able to higher-level improvements of searches for the Galctic or isotropic

diffuse emission. The photon flux from detected sources is majority of the photons detected by LAT, thus for high-energy astrophysics, to reveal the nature of this component is significantly important. The Fermi Collaboration has produced four γ-ray source catalogs stepwisely (1FGL was released at 1 [Abdo et al., 2010] year, 2FGL [Nolan et al., 2012] at 2 years, 3FGL [Acero et al., 2015] at 4 years and 4FGL [Abdollahi et al., 2020] at 8 years). In addition, there is an incremental version of the 4FGL catalog (4FGL-DR2 Ballet et al. [2020] for Data Release 2), which is based on 10-year observation data of energy ranges of 50 MeV to 1 TeV, while the data analysis is identical to 4FGL.

The 4FGL catalog is based on 8 years (August 4th 2008 to August 2nd 2016) of survey data with energy ranges of 50 MeV-1 TeV. The source detection has been based on their average fluxes. With the maximum likelihood analysis with the photon data, 5065 point-like and extended sources was detected with the detection threshold of test statistic (TS) larger than 25, which corresponds to somewhat more than 4 σ significance. On the other hand, in the 4FGL-DR2 catalog, 723 sources are newly detected while 120 sources are below the detection threshold among the 4FGL sources. 53 sources are newly associated and 4 associations are withdrawn. In the 4FGL sources, 358 sources have been found their counterparts, which are considered as identified based on angular extent, periodicity or variability correlation with other wavelength observations. In those counterparts, the Galactic objects (pulsar, binary, supernova remnant, globular cluster and pulsar wind nebula) and extragalactic objects (blazar, active galactic nuclei, star-forming, raidio and normal galaxy) are included. For 1336 sources, associated counterparts are not found at other wavelengths. It is essentially important for DM indirect searches using γ rays to identify γ-ray source counterparts, because those efforts lead to reduction of cosmic γ-ray photon flux with unknown origin, and then enable us to perform more robust signal probes.

3.1.2 Galactic diffuse emission

The Galactic diffuse emission is one of unresolved γ-ray components, that is, has no specific sources and is only known to be associated with the MW. According to Acero et al. [2015], the unresolved sources in the MW contribute less than 10% of the total Galactic diffuse emission. Therefore, the most photon flux of the diffuse emission is produced by interaction of cosmic rays with interstellar gas and the radiation field photons in the MW.

There are four production processes; inelastic collisions of cosmic-ray nuclei with nuclei in the interstellar gas, bremsstrahlung by interaction of cosmic-ray with electron, positron and ionized atoms, inverse Compton scattering of energetic charged particles with interstellar photons. With such various processes, it is very complicated to understand the nature of the diffuse emission.

In our analysis in Chapter 6, we estimate the systematic uncertainties introduced by our Galactic diffuse emission model. We follow the rigorous approach recommended in Ackermann et al. [2015a]. In that reference three different Galactic diffuse emission model is constructed using the Cosmic Rays (CR) propagation code `GALPROP`[1]. The three different model named Model A, B and C encapsulate a wide range of uncertainties in the interstellar gas column density distribution, CRs source distribution and energetics as well as the diffusion coefficient and Galactic magnetic fields. More details about those models are given in Ackermann et al. [2015a].

3.1.3 UGRB

UGRB is the residual component after subtracting all resolved source emission and Galactic diffuse emission from the observd photon flux. As this residual component consists of sources below a certain source-detection threshold, various sources that are too faint to be resolved discretely by LAT can contribute to the UGRB. While one cannot specify origins of individual UGRB photons, the nature of UGRB has been probed with statistical methods [e.g., Ackermann et al., 2015c, 2018].

It is worth to mention that the background modeling, derived from the standard Galactic diffuse, isotropic and resolved sources in the 4FGL source catalog, has been known to be incomplete in Ackermann et al. [2014] and Carlson et al. [2015]. That is because remaining γ-ray sources below the detection threshold largely contribute to diffuse anisotropic background which is able to be encompassed completely by the background modeling.

[1] `http://galprop.stanford.edu`

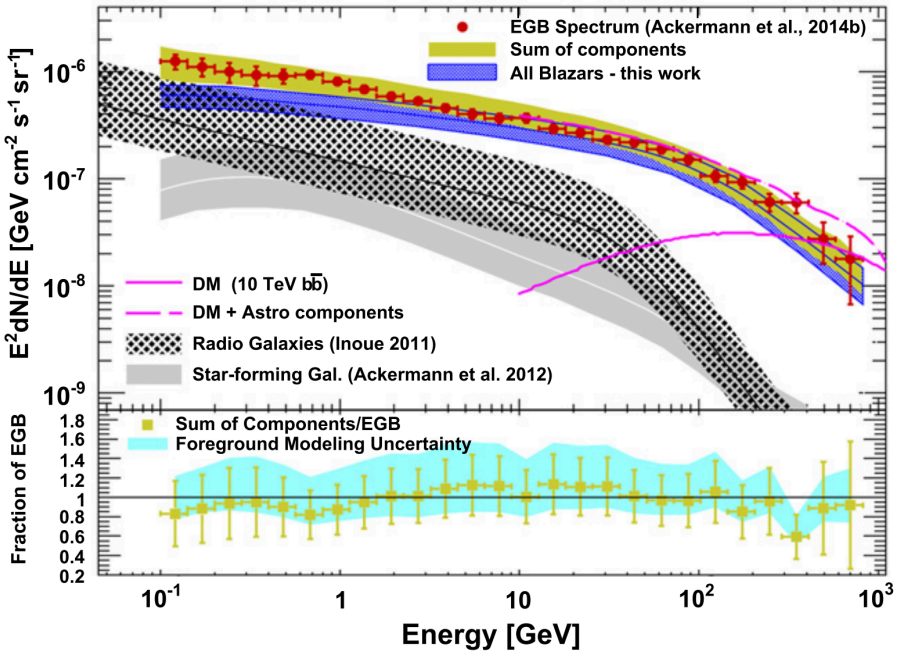

FIGURE 3.1: Extragalactic γ-ray components in GeV scales from Ajello et al. [2015]. (*Top*): There are the three components of the largest contribution to the γ-ray photons; Blazars (blue band), radio galaxies (black striped) and star-forming galaxies (gray band) with bath statistical and systematic uncertainties. The red errorbar plots are the observed extragalactic γ-ray background spectrum from the *Fermi*-LAT observation, including the contribution of resolved extragalactic sources. The yellow band represents the total contribution of the three astronomical components. (*Bottom*): The ratio of the total contribution to the observed extragalactic γ-ray spectrum. The Galactic foreground modeling uncertainty is shown in the shaded region.

3.2 Current constraints with Galactic structures or various local systems

3.2.1 Milky Way dwarf spheroidals

The MW dSphs, with few astronomical γ-ray sources, are located from several tens kpc to a few hundreds kpc and highly DM dominated. In addition, there is no association with γ-ray source among MW dSphs. Thus, the dwarfs are one of the most desirable objects for robust indirect DM searches in the Universe. There are many recent works, Ackermann et al. [2015d], Albert, A. et al. [2017], Boddy et al. [2018], Gammaldi et al. [2018], Ando

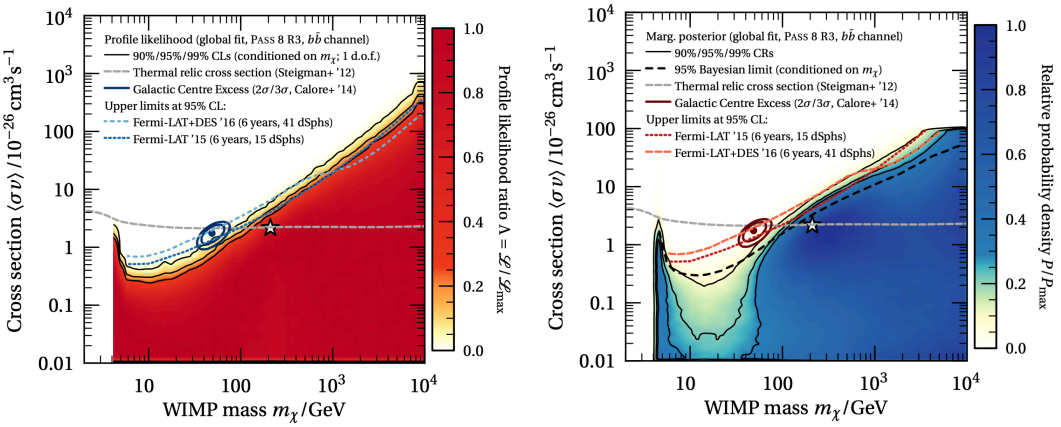

FIGURE 3.2: The constraint on the DM cross-section with 27 dwarfs. (*left*) With the profile likelihood method. (*right*) With the marginalized posterior for the Bayesian method. The colorbars represent a value of likelihood ratio to the maximum likelihood and posterior probability for the left and right panel, respectively. A considered annihilation channel is $b\bar{b}$.

et al. [2020], Hoof et al. [2020]. In Hoof et al. [2020], 27 MW dSphs have been used in the signal probe with 11 years of the LAT data. With spectroscopically measured J-factors, they have presented stringent upper limits using two different method, profile likelihood (frequentist) and Bayesian method without the log-normal approximation usually used in the probes with dSphs.

3.2.2 Galactic Center

The Galactic center are highly DM-dense region and very close to us, accordingly, one expects the luminous γ-ray flux that originated from the DM annihilation from this region. With recent γ-ray observations [Ackermann et al., 2017], the galactic center excess has been discovered, however components of the excess is yet unknown; thus the excess can include the annihilation γ-ray signal. At the same time, however, it is very challenging to distinguish γ rays produced by the DM annihilation from astronomical originated emissions in the excess emission, because the systematic uncertainties from luminous γ-ray emission from abundant astronomical activities is highly dominated. It is reported that the excess is well described by processes of decaying pions produced in interaction of high-energy cosmic ray with interstellar medium as well as the inverse Compton scattering of energetic electrons with radiation-field photons. Although our knowledge is short of

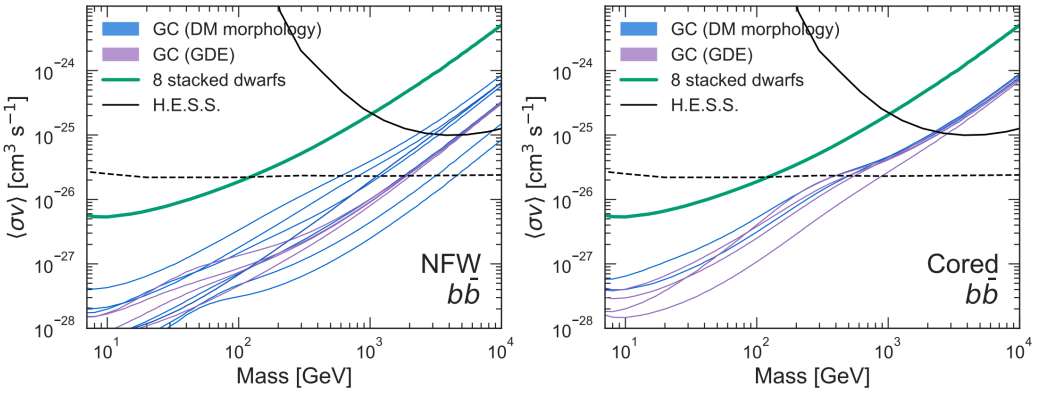

FIGURE 3.3: Upper limit on the DM cross-section with galactic center regions with the DM density profile assumed to the NFW (*left*) and cored (*right*) profile. All upper limits correspond to 95% confidence level. The purple lines represent constraints with different Galactic diffuse emission models. The black and green lines are constraints with the HESS observation towards the inner Galactic halo and the LAT observation using 8 MW dSphs, respectively. The dashed line corresponds to the thermal-relic cross-section. An annihilation channel of $b\bar{b}$ is considered.

the origin of this unresolved excess, the signal probe with this excess to detect the nature of DM particles is one of best way.

Abazajian et al. [2020] have searched the Galactic center excess, considering the large uncertainty of the unresolved astronomical emissions. To do so, they have performed the likelihood analysis with various templates for the stellar galactic and nuclear bulges as well as the Galactic diffuse emission models with generous variations. In the Galactic models, they have considered the three-dimensional inverse Compton emission, variations of interstellar-gas, and central electron distributions. Further, as the DM spatial morphology in the MW core, spherical and ellipsoidal shapes with both cuspy and cored radial profiles have been considered. As a result, they has reported no significant emission of the annihilating DM signal, and ruled out DM mass below 300 GeV for $b\bar{b}$ annihilation channel.

3.2.3 Catalog of extragalactic halos

Galaxy clusters are the most massive objects in the Universe while their angular sizes are relative small, accordingly the DM-signal probe with nearby galaxy clusters is one

of powerful approaches to understand the annihilating DM nature. The probe, however, has difficulty of robustness due to systematic uncertainties coming from intracluster astronomical γ rays. Despite the difficulty, their massive DM halos are expected to provide stringent constraint on the DM cross-section, using the fact that there is no evidence of significant γ-ray emission from them. In lots of those studies [Ando and Nagai, 2012, Ando, 2014, Regis et al., 2015, Ahnen et al., 2016], one of recent studies Lisanti et al. [2018] has provide the upper limit of 10^{-25} [cm^3/s] at DM mass of 100 GeV, using Galaxy Groups within $z \lesssim 0.03$.

In addition to the DM constraint using those cataloged clusters, there are a few studies using individual local clusters [Ackermann et al., 2015b, Adam et al., 2021]. In Adam et al. [2021], γ-ray emission induced by cosmic rays, which is a major component of the γ-ray emission from clusters, in the Coma cluster has been probed. Hence, the Coma cluster has halo mass of $\sim 7 \times 10^{14}$ M$_\odot$ and is relative close to us ($\sim$100 Mpc), one of the most promising sources to search γ-ray emission from the DM annihilation among extragalactic objects. The Coma cluster is associated with a 4FGL source, however the source may be originated from a radio galaxy in the cluster rather than the cluster itself. In this study, the residual γ-ray flux has been searched with the LAT data, applying a model of γ-ray flux induced by cosmic rays expected from intracluster thermal gas properties using the thermal Sunyaev-Zel'dovich effect and X-ray observations. In Ackermann et al. [2015b], with similar procedures to the study with the Coma cluster, the DM signal has been probed and DM particles with mass of < 40 GeV for $b\bar{b}$ have been excluded.

3.3 Indirect searches for other wavelengths

The annihilation process is expected not to only emit γ rays, but also photons with other wave lengths through decay and annihilation processes of charged particles, such as charged $\pi^\pm$ and $\mu^\pm$. In the decay processe, secondary charged particles are generated, i.e., $\pi^\pm \to \mu^\pm + \nu_\mu(\bar{\nu_\mu})$ and $\mu^\pm \to e^\pm + \bar{\nu_\mu}(\nu_\mu)$. The secondary products are very energetic, so that they heat environment photons (CMB photons or starlight) by electromagnetic interactions. Accordingly, indirect searches for the DM annihilation signal have been performed using observations in wavelength of radio, X-rays and γ rays [Vollmann et al.,

2020, Bhattacharjee et al., 2021]. Those DM annihilation probe with radio and X-ray observations are one of complementary probes with γ-ray data.

The electromagnetic interactions of energetic charged particles with photons are considered to several mechanisms like the synchrotron, inverse Compton, bremsstrahlung and Coulomb energy loss. In high energy regime, the synchrotron radiation and inverse Compton scattering are significant. In order to estimate the radio and X-ray emission originated from the DM annihilation, one needs to solve the diffusion equation of the secondary electron spectrum. The transport equation is,

$$\frac{\partial}{\partial t}\frac{\partial n_e}{\partial E} = \nabla\left[D(E,r)\nabla\frac{\partial n_e}{\partial E}\right] + \frac{\partial}{\partial E}\left[b(E,r)\frac{\partial n_e}{\partial E}\right] + Q_e(E,r), \tag{3.1}$$

where $n_e, D(E,r)$ and $b(E,r)$ are the electron number density, diffusion coefficient and energy loss per unit time of electron and position ($e^{\pm}$), respectively. $Q_e(E,r)$ is denoted by,

$$Q_e(E,r) = \frac{\langle\sigma v\rangle}{2m_\chi^2}\rho_{\rm DM}^2(r)\sum_i Br_i\frac{dN_f^e}{dE}, \tag{3.2}$$

where dN_f^e/dE is the $e^{\pm}$ injection spectrum in the f-th final state.

In Bhattacharjee et al. [2021], the multi-wavelength approach have been carried out to constrain the DM cross-section for different annihilation channels with a radio (Very Large Array) data in addition to the LAT γ-ray data, using four LSBGs with distance from 8 to 15 Mpc. With each observation data, they have estimated the radio and γ-ray limits and provided the upper limits for each annihilation channel with DM mass of 10 GeV-1 teV. As a result, in most mass ranges the constraints from the radio limit are more stringent roughly an order of magnitude than ones from the γ-ray limit except for the constraint for $b\bar{b}$ with DM mass $\lesssim 100$. The difference of the constraints with radio and γ ray observations shows the importance of the multi-wavelength approach for indirect DM searches. A sample of the constraints is displayed in the right panel in Figure 3.4 in addition to the multi-wavelength SED of a LSBG (UGC 3371) for different annihilation channels. We note that their DM constraint with the LAT data is consistent with one in our analysis with 8 HSC-LSBGs with known redshifts (see 6).

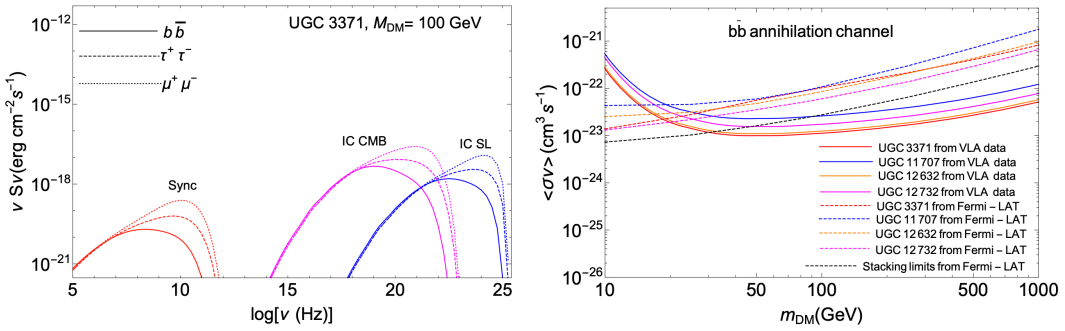

FIGURE 3.4: (*left*) SED for different annihilation channels at DM mass of 100 GeV for one of the four LSBGs (UGC 3371) in Bhattacharjee et al. [2021]. The solid, dashed and dotted lines are photon energy spectra for annihilation channels of $b\bar{b}, \tau^+\tau^-$ and $\mu^+\mu^-$, respectively. Three different types of peaks correspond to the synchrotron radiation, inverse Compoton with CMB photons and with starlight in order from left to right. In this plots, the diffusion coefficient and magnetic field are assumed to $D(E,r) = 3 \times 10^{-28} \mathrm{e}^{0.3}$ and $B(E,r) = 10^{-6} \mathrm{e}^{-r/r_c}$ (r_c is the core radius), respectively. (*right*) The cross-section upper limits for $b\bar{b}$ channel using four individual LSBGs. The solid and dashed lines represent the upper limits from the radio and γ-ray data, respectively.

Chapter 4

Low Surface Brightness Galaxy

In this chapter, we summarize LSBG properties in the context of astrophysics and mention their significant features related to the annihilation-signal probe.

Research on faint and diffuse objects stared with the statistical studies of galaxy surface brightness. In 1970, Freeman [1970] measured the central surface brightness of 36 galaxies and found that 28 objects had quite similar central surface brightness in B-band $\mu_0(B)$, and the average was $\mu_0(B) = 21.65$ with standard deviation of 0.3 mag arcsec^{-2}, whereas the absolute magnitudes had a significant difference (distributed over a range of 5 magnitudes). He also discovered a significantly low surface brightness object, IC 1613, in the remaining eight irregulars, which had $\mu_0(B) = 23.7$ mag arcsec^{-2}, and the absolute magnitude was estimated to be -14.4 magnitude. Because the central surface brightness of faint objects, such as IC 1613, are typically darker than the dark night sky background, discovering such dwarfs had been very rare at the time.

According to the history, the traditional definition of LSBG is a faint object of lower surface brightness than $\mu_0 \sim 22$ mag arcsec^{-2}. In practice, researchers have defined the lowest brightness of the central or effective surface brightness in a certain band (B or g band in most cases) to classify LSBGs and other high surface-brightness galaxies (HSBGs). For example, Greco et al. [2018a] and Tanoglidis et al. [2021], who provide two LSBG catalogs used in this thesis, applied the definition of the effective surface brightness limit in g-band of $\mu_{\rm eff}(g) = 24.3$ mag arcsec^{-2} and 24.2 mag arcsec^{-2}, respectively. In the two catalogs, most objects have $\mu_{0,g} > 22$ mag arcsec^{-2}. Because the definition of LSBG

is not based on any astrophysical background, the astrophysical properties of LSBGs have diversity. Nevertheless, their statistical properties have been elucidated in recent studies, wherein LSBGs are gas rich, metal poor, and dust (molecular cloud) poor [McGaugh and Bothun, 1994, Matthews et al., 2001, Trachternach et al., 2006]. In addition, LSBGs have low-density diffuse stellar disks [Galaz et al., 2011, Lei et al., 2019]. As expected from the above properties, they have very low star-formation rates (SFRs) Cao et al. [2017], Lei [2019]. Understanding LSBG properties is significant for revealing the galaxy evolution and morphology, which has been studied with multiwavelength observations [e.g., Greco et al., 2018b, Du et al., 2019, Di Paolo et al., 2019].

In particular, because most LSBGs are HI-rich, radio surveys with a frequency of $\sim$ 1.4 GHz are one of the best technique to discover them in the local universe. Du et al. [2015] have probed the statistical properties of LSBGs to a distance of up to 250 Mpc using the 40% sky area of the Arecibo Legacy Fast Arecibo L-band Feed Array (ALFALFA) catalog [Haynes et al., 2011] cross-matching with the SDSS DR7 catalog [Abazajian et al., 2009], thereby discovering different LSBG properties, such as the HI mass, absolute magnitude, luminosity and velocity width of HI line. Moreover, with optical bands for measuring rotation curves of galaxies, the DM halo mass of LSBGs and their density profile have been probed [Greco et al., 2018b, Di Paolo et al., 2019].

Advantages of use of LSBG

For our probe of the annihilating DM signal, we have several advantages of using LSBGs as follows.

· *DM dominated system*
The rotation curve measurements of LSBGs are robust techniques to estimate the DM halo mass of LSBGs directly. According to de Blok and McGough [1997], Di Paolo et al. [2019], most LSBGs have DM halo masses of $\sim 10^{10} - 10^{12}$ $M_\odot$, contrary to their stellar mass of $\sim 10^{8} - 10^{10}$ $M_\odot$. Therefore, LSBGs are highly DM-dominated systems with a comparison of those of HSBGs.

· *Low astronomical γ-ray contamination*
With observations for CO or Hα line emissions from molecular gas clouds and hot stars in target galaxies, one can access information of star-formation activities for these objects.

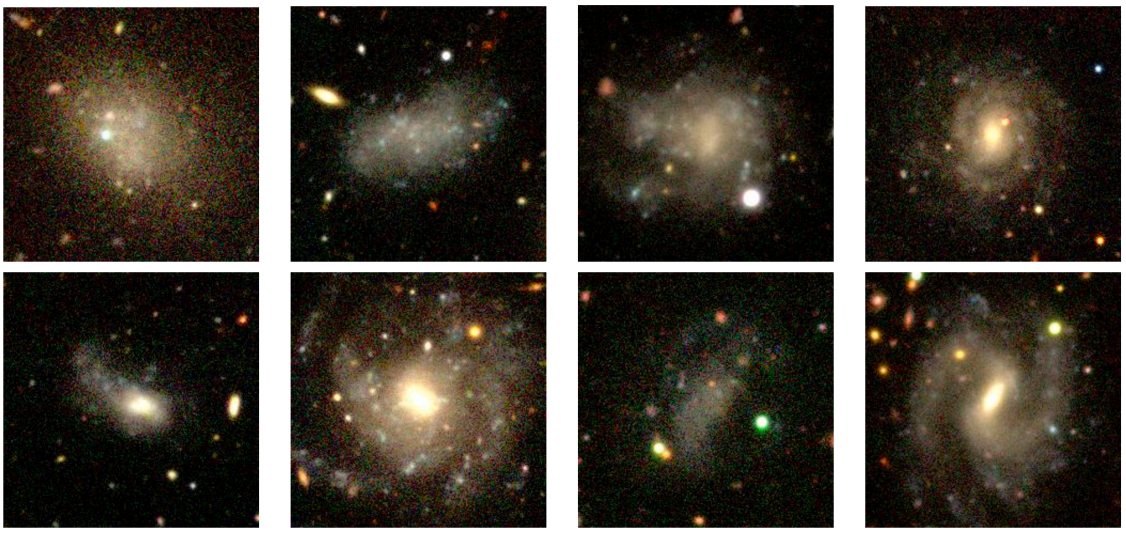

FIGURE 4.1: Image samples of the eight HSC-LSBGs with measured redshifts, which are used in Section 7.3 and 6.3. Each image size is 40 arcsec on the side. This figure is from *gri* composite images by the HSC Subaru Strategic Program (HSC-SSP) [Hashimoto et al., 2020].

Cao et al. [2017] and Lei [2019] have searched for emission lines from LSBGs to infer their star-formation rates (SFRs), using CO spectra and Hα fluxes. As a result, they have found that most LSBGs have low SFRs of $\lesssim -0.1$ [$M_\odot$ yr^{-1}], which are comparable to those of local dwarf galaxies. A Low SFR leads to a few γ-ray photons that originated from star-forming activities, neutron stars and supernova remnants, resulting in low astronomical γ-ray contamination to the UGRB field used in our analysis as well as robust probe of the annihilating DM signal.

· *Point-like sources*

As we will describe in Section 5.3.1, we consider our LSBG samples point-like sources in the likelihood analysis with the LAT γ-ray data because their angular sizes are much smaller than the LAT-PSF in all energy ranges we consider, resulting in less systematic uncertainty in our likelihood analysis than one using more extended sources.

· *Numerous objects in the local universe*

Minchin et al. [2004] have searched a population of gas-rich LSBGs using radio surveys with a sky coverage of 36 deg^2, and concluded that the LSBGs contribute $20 \pm 10\%$ to the dynamical mass of galaxies in the local universe, and their number density can reach 60% fraction of the local gas-rich galaxy population. Moreover, Trachternach et al. [2006]

have combined HI-selected LSBGs and an optical search for local galaxies, and showed that the number density of LSBGs can reach 30%-40% of the local galaxy population.

Chapter 5

Data

In this chapter, we describe datasets of two LSBG catalogs and the γ-ray photon data from the *Fermi*-LAT observation as well as two spec-z galaxy catalogs used in Chapters 6 and 7, to estimate redshift distributions of overall each LSBG catalog using the clustering redshift method.

5.1 LSBG sample

In this section, we describe two LSBG catalogs, the HSC- and DES-LSBG catalog, concerning the construction of each observation and catalog. Note that our purpose of the use of two LSBG catalogs is as follows: (i) The HSC-LSBG catalog will be used in Chapter 6 and Chapter 7. In Chapter 6, we will describe the calculation of the J-factor of eight HSC LSBGs with known redshifts and the likelihood analysis with the stacking of these objects. Further, in Chapter 7, we will use the catalog to validate our procedure, which focuses on the redshift distribution of the catalog to constrain the DM cross-section, instead of using individual object redshifts. In addition, to clarify the efficiency of our procedure, we will find a scaling relation between the number of LSBGs and the DM cross-section constraint. (ii) In the analysis with the DES-LSBG catalog, we will find the main result of this thesis, which shows the current constraint on the DM cross section with the largest LSBG catalog at present.

5.1.1 HSC-LSBG catalog

HSC is a wide-field imaging camera installed at the prime focus of an 8.2-m Subaru telescope built by the National Astronomical Observatory of Japan collaborating with international partners, covering ∼1.5° diameter field of view (FoV) with a 0.17 arcsec pixel scale [Miyazaki et al., 2018, Komiyama et al., 2018]. Owing to this imaging camera, highly adjustable adaptive optics with lots of computer-controlled actuators and superb site on the summit of Maunakea (seeing $\sim 0.6''$), the HSC survey enables us to measure the shape and photometry measurements of numerous objects residing in a wide distance range, from the solar system to cosmological distance.

The HSC-SSP survey employs three layers, wide, deep, and ultradeep layers, to discover numerous astronomical objects and events in a wide range (for galaxies, the range extends to $z \sim 1.5$), and each HSC working group has performed different targeted projects, such as the search for AGN, weak/strong lensing, clusters, supernovae, and photometric calibration. Among the three layers, the wide layer has five broad photometric bands g, r, i, z, and y similar to those of SDSS and, has a depth of 24.5–26.6 in the five filters for 5σ point-source detection, as described in a report of the second data release of the survey by Aihara et al. [2019]. The observation dataset of the wide layer for the first internal data release *S16A* [Aihara et al., 2018] has a survey area of ~ 200 deg^2 sky coverage. In the third public data release [Aihara et al., 2021], which is the up-to-date data release of the HSC-SSP survey, the deep layer covers 27 deg^2 in four separate regions with both the five broad bands and three narrow filters (N387, N816 and N921) using exposure times of 1-3 hours in each band. The ultradeep layer covers 3.5 deg^2 with a narrow band filter of N1010 in addition to the same broad and narrow filters of the deep layer, with long integration times of $\sim$ 5-10 hours in each band. The fields of the UltraDeep layer are centered at the COSMOS and Subaru XMM-Newton Deep Field. In the final data release, the survey will cover a 1200 deg^2 sky coverage with integration times of 10-20 minutes and the depth with 5σ detection will reach $i \sim$26 mag [Aihara et al., 2021].

For the HSC-SSP data reduction, the optical imaging processing pipeline, `hscPipe` [Bosch et al., 2018], have been built, which is based on a prototype pipeline developed by the Legacy Survey of Space and Time (LSST) survey Data Management system [Jurić et al., 2017]. Unfortunately, `hscPipe` is not optimized for detecting and measuring diffuse objects, such as extended LSBGs, because the pipeline is likely to cause the shredding of such

objects. Moreover, it is difficult for the detection/measurement of such objects to avoid contamination of the foreground and background light. Particularly, this contamination leads to unreliable shape and surface brightness measurements of LSBGs. Accordingly, Greco et al. [2018a], who provide the HSC-LSBG catalog, developed a pipeline [1] based primarily on the LSST codebase to reduce HSC images. They further have incorporated two software systems, *SourceExtractor* [Bertin and Arnouts, 1996] and *imfit* [Erwin, 2015], to measure initial object parameters for sample selection and refine estimates of object parameters, respectively.

In Greco et al. [2018a], the LSBG catalog is produced using an observation dataset of the wide layer with *S16A* data. To avoid the limitation of survey areas by requiring all bands, they have used only three bands (g, r, and i-band) because the survey progress differs by photometric bands. Using `hscPipe`, they have produced sky-subtracted co-add images and divided the images into equivalent rectangular regions called tracts (each tract has an area of 1.7 deg^2). Further, tracts have been divided into 9×9 grids of patches and each patch have been pixelized into 4200×4200 pixels. To identify LSBGs, the validity of the sky-subtraction is important because the mean surface brightness of target objects is fainter than the night sky brightness. As described in Bosch et al. [2018], an algorithm for the sky-subtraction used in `hscPipe` causes an oversubtraction of the background around extended sources ($> 1'$). Therefore, LSBGs found in Greco et al. [2018a] can be biased against the detection of LSBGs around such extended sources.

`hscPipe` is optimized to identify faint and small objects, such as distant galaxies. If we use the pipeline for extended objects, single extended objects are decomposed into multiple child objects, the so-called "shredding". Typically, an LSBG in the HSC-LSBG catalog is divided into more than 10 child objects. Moreover, LSBG brightness is comparable to the sky background noise; thus the shape and surface brightness of LSBGs are probably misestimated. Therefore, in procedures to identify LSBGs, Greco et al. [2018a] have developed a pipeline based on the LSST codebase mainly, instead of using `hscPipe`. In addition, they have used SourceExtractor Bertin and Arnouts [1996] to compose an initial catalog of LSBG candidates and then selected them based on size and color measurements. Finally, `imfit` Erwin [2015] has been used to refine their parameters. The above procedures has been performed on a patch-by-patch basis. Then, LSBGs are finally defined such that the mean surface brightness is larger than 24.3 mag arcmin^{-2}.

[1] https://github.com/johnnygreco/hugs

Consequently, 781 LSBGs are detected within an HSC Wide *S16A* footprint. The LSBG identification procedure is summarized as follows.

1. First, bright sources and associated diffuse lights are subtracted from images because they might mimic LSBGs. The subtracted regions are replaced with randomized background noise.

2. After smoothing with the Gaussian kernel (full width at half maximum = $1''$), sources with the half-light radius of $2.5'' < r_{1/2} < 20''$ are extracted. Furthermore, by applying reasonable color cuts, optical artifacts and high-redshift galaxies are removed.

3. By modeling the surface brightness profiles of LSBG candidates, astronomical false positives are removed. Finally, the remaining false candidates, which are typically point-like sources with diffuse background lights, are removed by visual inspection. The obtained LSBG samples are 781 objects.

Basically, these procedures are applied to the i-band images; however, to reduce the number of false detections including any artificial effects, all LSBG candidates are required to be detected in g-band images as well. We divide the full sample into red and blue LSBGs, which are defined by $g - i \geq 0.64$ (450 objects) and $g - i < 0.64$ (331 objects), respectively. This color selection roughly corresponds to the galaxy age of 1 Gyr for a 0.4 $\times$ solar metallicity galaxy [Greco et al., 2018a]. For a random catalog corresponding to the LSBG catalog, we employ the random catalog of the HSC photometric data, and randomly resample it such that the number density is approximately 10 times larger than the LSBG density. We also apply the bright star mask to the random catalog. In Figure 5.2, the HSC LSBGs' properties of color magnitudes and effective radii are shown, and the sky distribution of the LSBG sample is displayed in Figure 5.1.

8 HSC LSBGs with known redshifts

In the next chapter, we will consider one of our studies to probe the DM annihilation cross-section rate using eight individual HSC LSBGs with known redshifts. Note that only the eight objects have known redshifts in the HSC-LSBG catalog, and their redshifts are provided by cross-matching with other catalogs or from long-slit spectroscopy.

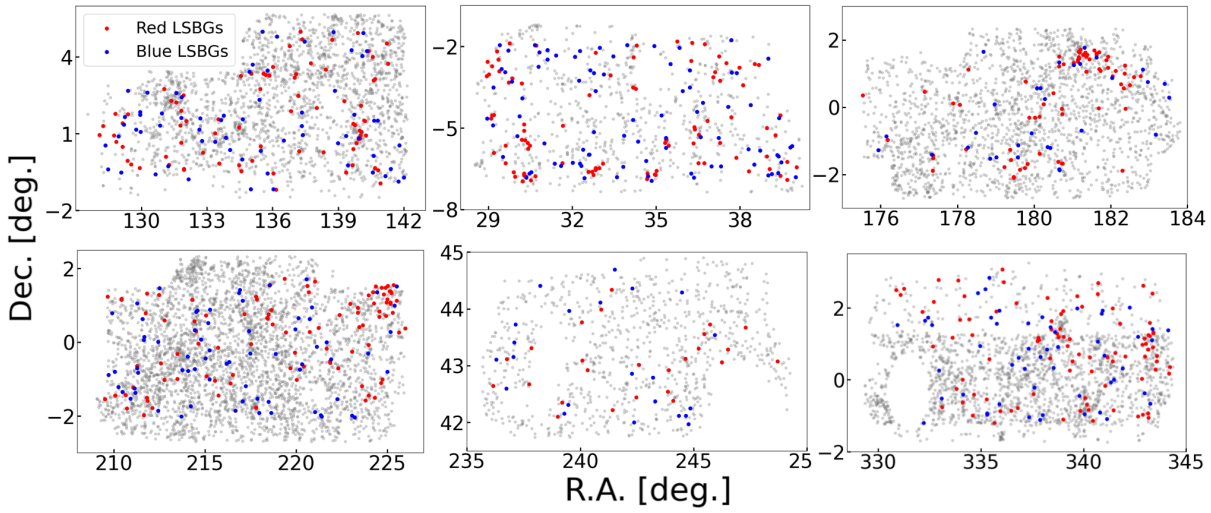

FIGURE 5.1: Sky distributions of the red ($g-i \geq 0.64$, red dots) and blue ($g-i < 0.64$, blue dots) HSC LSBGs as well as the NSA sample with $z < 0.15$ (gray dots) in the HSC-SSP internal data release of *S16A*.

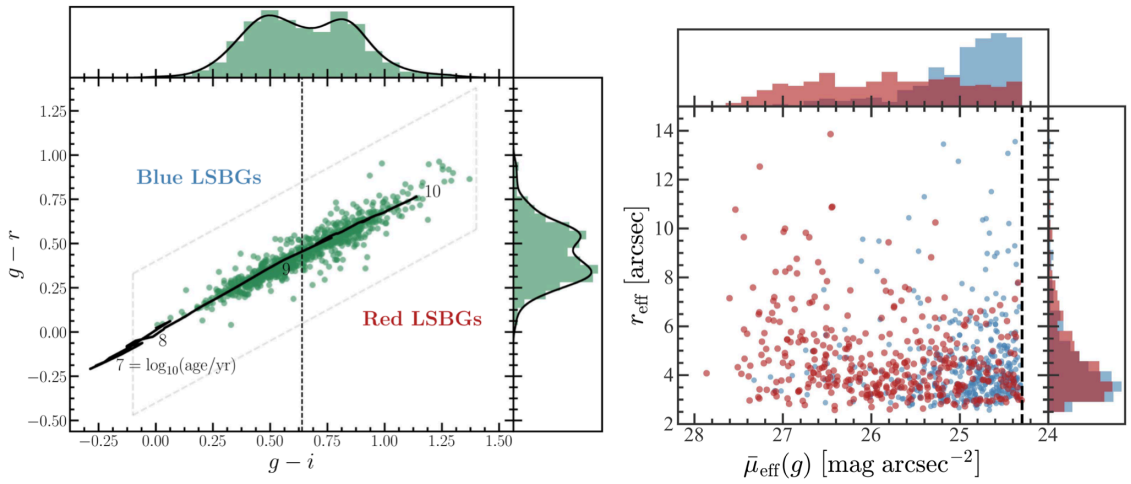

FIGURE 5.2: (*Left*) Color-color diagram for HSC LSBGs divided into red ($g-i \geq 0.64$) and blue ($g-i < 0.64$) samples. (*Right*) The scatter plot of the effective surface brightnesses (measured within the circularized effective radius) in g band and effective radii (measured along the major axis) of HSC LSBGs. (Adapted from Greco et al. [2018a])

In Greco et al. [2018b], redshifts of six LSBGs have been specified by cross-matching with other object catalogs as follows.

(i) The NSA catalog (Blanton et al. [2011]) has three matches: LSBG-171, LSBG-456, and LSBG-613. The first two are face-on spirals at $z = 0.04389$ and $z = 0.02863$, respectively, from the SDSS spectroscopic catalog (NSA ID: 42601 and 145288). The third matche (NSA ID 144517) is measured in an LSB dwarf search of Roberts et al. [2004] and is at $z = 0.02447$. Although the three LSBGs' physical sizes and central surface brightnesses are similar to those of ultra diffuse galaxies (UDGs), the absolute magnitudes of the first two (LSBG-171 and LSBG-456) are at least three magnitudes brighter than those of UDGs.
(ii) The 70% ALFALFA catalog [Haynes et al., 2011] has three matches: LSBG-456, LSBG-464 and LSBG-575. The first match (AGC 243463) is the same object in cross-matching with the NSA catalog. The second match (AGC 249425) is at $z = 0.02573$. It is inferred that AGC 249425 has active star-formation regions in the entire disk due to strong detection of the disk in the ultraviolet range. The remaining one (AGC 189086) at 29.5 Mpc is a gas-rich UDG with a baryonic gas fraction of $\sim$0.87. Its stellar mass is inferred to be $\sim 2.6 \times 10^7$ $M_\odot$.
(iii) The LSBG-729 is a host galaxy of the Type IIb supernova SN 2009Z (Zinn et al. [2012]) at $z = 0.02513$, which is confirmed using the archival optical imaging from SDSS and the Newton Technology Telescope. Greco et al. [2018a] have estimated its stellar mass to be $\sim 10^9$ $M_\odot$ from the HSC-SSP photometry.

Greco et al. [2018a] have searched the remaining two objects of the eight LSBGs, LSBG-285 and LSBG-750, using long-slit spectroscopy from the Gemini Multiobject Spectrograph observation, whose integration time for each object is 1 hour with a spectral range of 4880-7200 Å, and photometry with different wavelengths of mid-infrared, optical, and ultraviolet. Via spectroscopy, they have estimated distances to be 24.6 ± 0.3 (LSBG-285) and 41.3 ± 0.3 (LSBG-750) using Hα line-emission centroids. Further, from template fitting of the spectral energy distribution (SED) combined results from spectroscopic analysis, they have estimated the absolute magnitudes, stellar masses, metallicities, and ages since star-formation activities started. In particular, the stellar masses are estimated to be $2.7^{+0.4}_{-0.3} \times 10^7$ $M_\odot$ (LSBG-285) and $2.3^{+0.9}_{-0.6} \times 10^7$ $M_\odot$ (LSBG-750)[2], and the halo masses

[2]These three values are median, 84th (superscript) and 16th (subscript) percentile of the posterior distribution in the combined analysis.

LSBG ID	(l [deg], b [deg])	redshift	m_i	$g-r$	$g-i$	Distance[Mpc]
171	(62.628, -45.915)	0.0439	17.55	0.49	0.77	186
285	(178.250, -57.202)	0.00581	17.47	0.44	0.6	24.9
456	(351.210, 54.493)	0.0286	17.18	0.4	0.57	122
464	(348.724, 55.429)	0.0257	16.95	0.37	0.58	110
575	(224.099, 24.123)	0.00695	18.45	0.29	0.3	29.7
613	(339.731, 57.465)	0.0244	19.17	0.19	0.29	104
729	(336.533, 56.860)	0.0251	17.57	0.36	0.55	107
750	(276.818, 59.451)	0.00862	18.38	0.24	0.33	36.9

TABLE 5.1: Parameters of eight LSBGs with known redshifts in the HSC-LSBG catalog. The parameters are object ID, galactic longitude, galactic latitude, redshifts, i-band magnitudes, color diagram for $g-r$, $g-i$, and comoving distances of LSBGs, respectively. The values, except for distances of LSBG-285 and LSBG-750, are obtained from Greco et al. [2018a], and the two distance values are obtained from Greco et al. [2018b].

are indicated to be $< 10^{11}$ $M_\odot$.

In Table 5.1, the parameters of the eight LSBGs are summarized, and each LSBG image used in this thesis is shown in Figure 4.1.

5.1.2 DES-LSBG catalog

DES is an imaging survey of five optical broad bands spanning 400 to 1,080 nm (g, r, i, z, and Y) covering $\sim 5,000$ deg^2 of the southern hemisphere using the Dark Energy Camera (DECam) [Flaugher et al., 2015] on the 4-m Blanco Telescope at the Cerro Tololo Inter-American Observatory. The DECam comprises 74 charge-coupled devices (CCDs) of 250-μm thickness, which are divided into two types of CCDs: 62 CCDs of 2k $\times$ 4k pixels and 12 CCDs of 2k $\times$ 2k pixels. The total number of pixels in the full imaging reaches 570 Mpixels with an FoV of 2.2° diameter and a central pixel scale of 0.263″.

The DES collaboration has conducted the photometric survey 105 nights per year, particularly to uncover the dark energy nature by performing the survey of the southern Galactic cap in unprecedented depth and width. To accomplish this aim, they have planned complementary probes for galaxy clusters, weak lensing, Type Ia supernovae, and baryon acoustic oscillations. The DES survey area is designed to include the entire

South Pole Telescope survey footprint, which is for the Sunyaev-Zel'dovich (SZ) cluster survey to search for cluster cosmology using both surveys. In addition, the survey area overlaps a part of the SDSS observation area, which is designed for better precision of the DES photometric calibration.

To satisfy observational requirements for each cosmological probe, the DES Collaboration has planned the following two survey modes. (i) The *Wide Survey* covers the entire survey area of $\sim 5,000$ deg^2 to probe the gravitational weak lensing, galaxy clustering, and cluster cosmology. Each co-add image in each of the five broad bands is processed with 10 dithered exposures to consider gaps between CCDs. In the first three years of DES (DES Y3), each survey position has been visited four times in most footprints in each band. (ii) The *Supernova Survey* covers only a 27 deg^2 sky, which consists of 10 DECam fields, and DES has observed each filed repeatedly per six nights in g, r, i, and z bands. This survey strategy enables us to discover thousands of Type Ia supernovae in the redshift range of $0.2 < z < 0.85$ and obtain their photometric lightcurves.

In the Wide Survey of DES Y3, the median co-add magnitude limits in the g, r, i, z, and Y band with a signal-to-noise ratio (S/N) of 10 are 24.3, 24.0, 23.3, 22.6, and 21.4, respectively [Sevilla-Noarbe et al., 2021]. For LSBG detection, dedicated background estimation is indispensable [Morganson et al., 2018, Sevilla-Noarbe et al., 2021]. The single epoch processing pipeline, `Final Cut` [Morganson et al., 2018], provides reduced images and performs the source detection and measurement of galaxies with `SourceExtractor`, which can discover faint objects.

The LSBG sample [3] [Tanoglidis et al., 2021] is constructed from the DES Y3 Gold sample as follows.

1) *Extraction of candidates from DES Y3 Gold catalog*

From the DES Y3 Gold co-add catalog (v2.2) [Sevilla-Noarbe et al., 2021], point-like objects are removed based on i-band `SourceExtractor SPREAD_MODEL` parameter, and the following sample selection constraints are imposed: i) half-light radii in g-band, $2.5'' < r_{1/2}(g) < 20''$, ii) surface-brightness in g-band, $24.2 < \bar{\mu}_{\rm eff}(g) < 28.8$ mag/arcsec^2, iii)

[3] `http://desdr-server.ncsa.illinois.edu/despublic/other_files/y3-lsbg/`

ellipticity < 0.7, and iv) color cuts based on the `SourceExtractor MAG_AUTO` magnitudes,

$$
\begin{aligned}
-0.1 < g - i < 1.4 \\
g - r > 0.7 \times (g - i) - 0.4 \\
g - r < 0.7 \times (g - i) + 0.4.
\end{aligned}
$$

The obtained catalog contains 419,895 candidates after these source selections from ~ 400 million objects in the initial catalog.

2) *Sample selection by machine learning*

A machine learning algorithm is used to further remove contaminations, such as giant elliptical galaxies, compact objects with the diffuse foreground or background, and knots of large spiral galaxies. Note that this step is not for identifying LSBG samples from candidates, but for rejecting numerous false candidates. The training set is constructed by visual inspection of images in seven patches with no overlapping region (~ 100 deg^2 of the total sky coverage). As a result of the visual inspection, 640 objects have been classified as LSBGs in total labeled objects of 7,760. The samples are divided into 75% and 25% as the training and validation sets, respectively. As an optimal classifier, a linear support vector machine is employed. The machine learning classification identified 44,979 objects as LSBG candidates. Note that the $\sim 9\%$ LSBGs are undetected with this method. The validation of the machine learning algorithm provided a false-negative rate of $\sim 9\%$, meaning that the number of LSBGs corresponding to this rate may be included in the rejected candidates.

3) *Visual inspection and Sersic model fitting*

The candidates have been visually inspected using cutouts of $30'' \times 30''$ centered at the candidate position of each candidate. A Sersic profile [Sersic, 1968] is fitted to each candidate, and multiband photometric properties is measured using `galfitm` [Häußler, Boris et al., 2013], which enables us to compare the LSBG properties to those of other LSB objects catalogs. Finally, the light profile is fitted to the Sersic profile to distinguish the LSBGs from other objects. All LSBGs should pass the selections of effective radii $R_{\rm eff}(g) > 2.5''$ and $\bar{\mu}_{\rm eff}(g) > 24.2$ mag/arcsec^2.

The final catalog contains 23,790 LSBGs with the surface brightness fainter than 24.2 mag/arcsec^2. They are divided into 7,805 red ($g-i \geq 0.6$) and 15,985 blue ($g-i < 0.6$) LSBGs. Although the red LSBGs are strongly clustering, the blue LSBGs are rather uniformly distributed. According to the stellar population model of [Marigo et al., 2017], the typical ages of red and blue LSBGs are, respectively, 4 Gyr and 1 Gyr with [Fe/H] = -0.4. In Figure 5.3, the sky distribution of the DES-LSBG sample is shown, and their colors and effective radii are displayed in Figure 5.4.

5.2 Spectroscopic sample

For measuring of the dN/dz distribution, we need reference spec-z samples in the overlapped region in both sky-coverage and redshift ranges which will be a very low-redshift span because LSBGs are possibly in the local universe.

5.2.1 NSA sample

The NSA sample [4] is a spec-z sample obtained from the spec-z campaign of the Sloan Digital Sky Survey with the Galaxy Evolution Explorer data for the energy spectrum of the ultraviolet wavelength and includes objects up to $z = 0.15$, containing 11,820 objects in the overlapping region with HSC LSBGs. The redshift distribution of the spec-z sample is displayed in Figure 5.5. Because the uniformity of the NSA sample is not guaranteed, we attempt to mitigate the nonuniformity as follows. First, we remove the sample from both HSC and NSA in the bright star masked regions. After removing the masked regions, we check that the local number density of NSA galaxies has a uniform distribution in most areas of the HSC regions we are working on, except for the low-density region in the VIMOS-VLT Deep Survey with Dec.>1. We generate a random catalog, including about 10 times more objects than that of the NSA galaxies. In addition, we removed the edge regions in the HSC survey footprint for safety, because the exact survey window near the boundaries is difficult to define.

[4] https://data.sdss.org/sas/dr13/sdss/atlas/v1/nsa_v1_0_1.fits

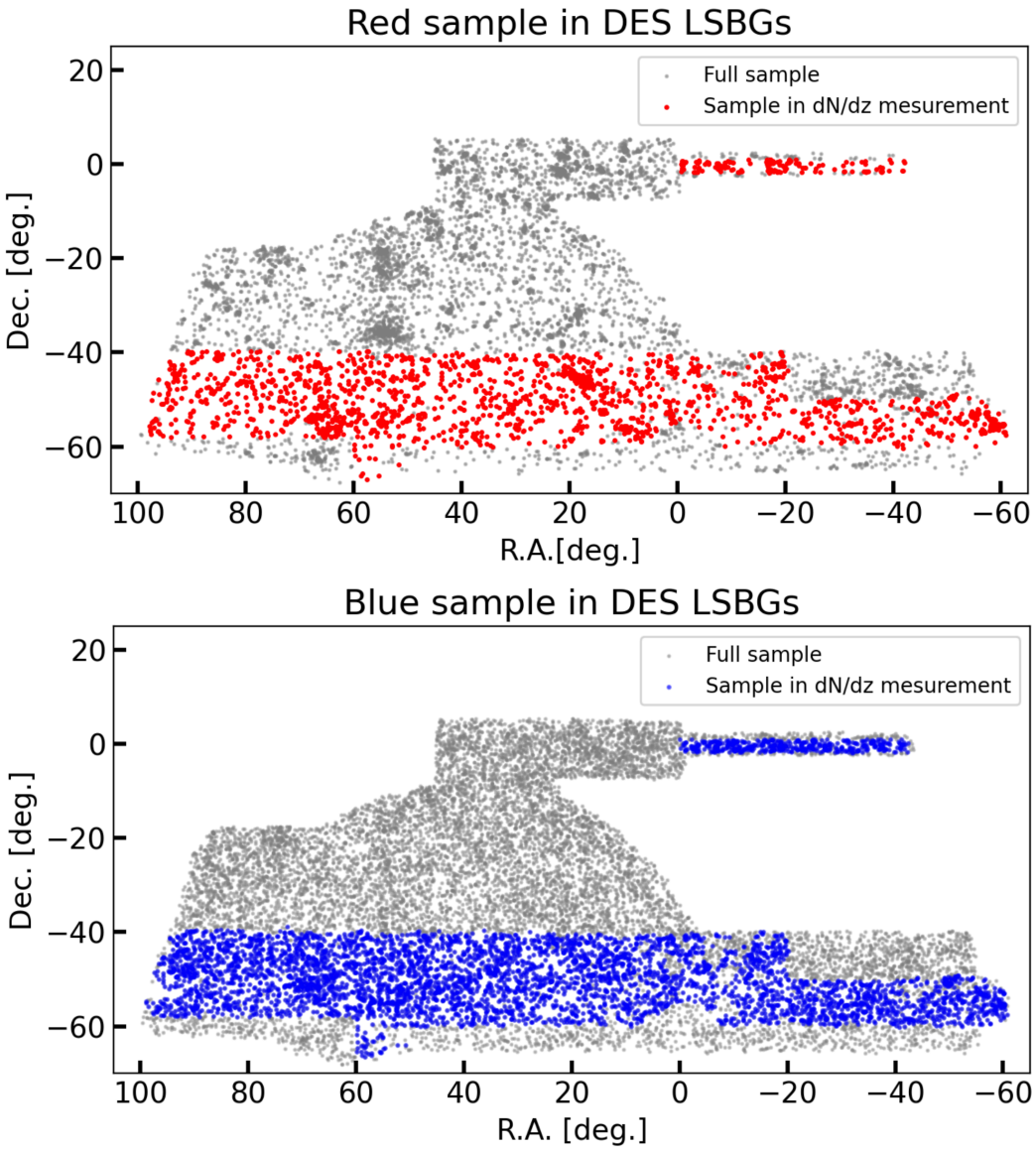

FIGURE 5.3: Sky positions of the red ($g - i \geq 0.60$) and blue ($g - i < 0.60$) DES-LSBG samples in the top and bottom panels, respectively. The red and green dots represent samples used in the dN/dz measurement.

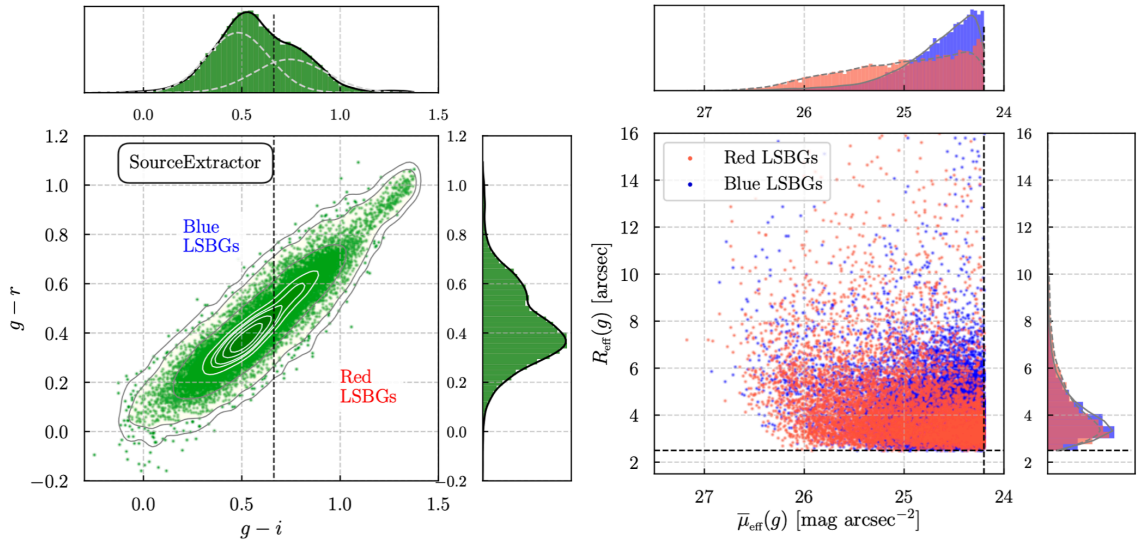

FIGURE 5.4: (*Left*) Color-color diagram for DES LSBGs divided into red ($g-i \geq 0.60$) and blue ($g-i < 0.60$) samples. (*Right*) The relation of the effective surface brightness (measured within the circularized effective radius) in the g band and effective radii (measured along the major axis) of DES LSBGs. These plots are adapted from Tanoglidis et al. [2021].

5.2.2 6dFGRS sample

For measuring the DES LSBGs's dN/dz, we use the final data release (DR3) of Six-degree Field Galaxy Survey (6dFGS) spectroscopic redshift sample [5] [Jones et al., 2004, 2009]. The catalog is based on the observation of the Six-Degree Field (6dF) fiber-red multiobject spectrograph in the near infrared wavelength at a 1.2-m UK Schmidt Telescope, covering over $\sim 17,000$ deg^2 of the southern sky and more than 10° from the galactic plane. The limiting magnitudes in K, H, and J bands are 12.65, 12.95, and 13.75, respectively, and the catalog comprises 1,447 6dFs (5, 7° FoV) of the telescope, covering most survey regions two times over. In each field, 150 spectra are obtained simultaneously by individual fibers which have 100 μm ($\sim 6.7''$)-fiber diameter size of each. Owing to the fiber collision and interference between neighboring buttons, the spectra of neighboring objects closer than 5.7 arcmin cannot be measured simultaneously. These wide gaps between sizes of the fiber diameter and the lowest distance for the simultaneous measurement are largely due to the difference between sizes of the input end of the fiber (5-mm diameter circular button)

[5] http://www-wfau.roe.ac.uk/6dFGS/download.html

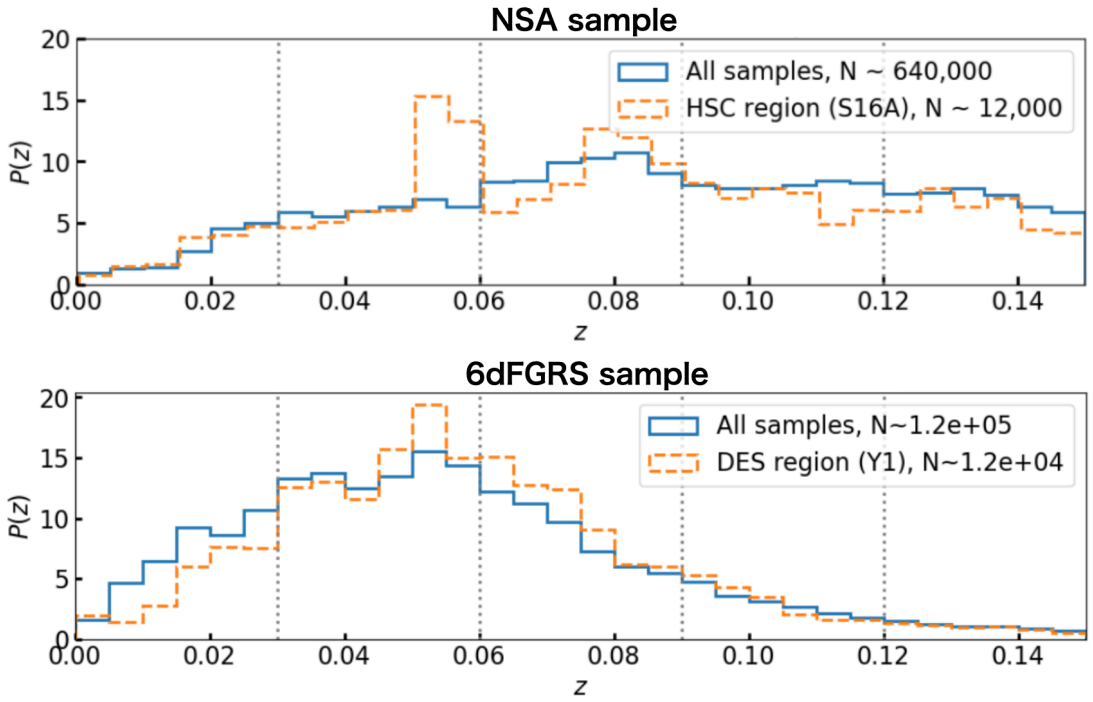

FIGURE 5.5: The redshift distributions of the NSA (top panel) and 6dFGRS (bottom panel) spec-z samples. In each panel, the solid and dashed lines are distributions of overall spec-z sample and limited sample within the survey footprints of S16A and Y1 Gold, for the NSA and 6dFGRS observations, respectively. The vertical lines represent redsfhit-binning bounds with equal width of 0.03. N denotes the number of objects of corresponding samples.

and the fiber diameter (100 μm). As described in the DR3 report [Jones et al., 2009], we only use samples with the redshift-quality flag $Q = 3, 4$.

The random sample corresponding to the DES galaxy sample is only available publicly for the Y1 Gold object catalog [Drlica-Wagner et al., 2018] that has been reduced from the DES observation data with the first one year. For measuring the angular cross-correlation in the clustering redshift method, we need random samples corresponding to both the LSBG and spec-z samples in fully overlapping sky regions. Accordingly, we use the limited LSBG sample ($\sim$ 7000 obejcts) only in dN/dz measurement of the DES-LSBG sample within the footprint of the Y1 Gold, which covers $\sim$ 1800 deg^2.

5.3 *Fermi*-LAT photon data

5.3.1 LAT instrument and performance

LAT is a γ-ray detector for imaging surveys in the whole sky and the primary instrument on boarding the Fermi Gamma-Ray Space Telescope launched in June 2008. Over 13 years, the LAT has observed cosmic γ rays and provided photon data with unprecedented solution, energy dispersion, and sensitivity, enabling us to probe the natures of various high-energy events and their origins, such as gamma-ray bursts, supernova remnants, pulsars, active galactic nuclei, and star-forming galaxies. In addition, observed γ-ray excess and unspecified components are expected to play a significant role to access new physics beyond the SM, such as WIMPs.

The instrument has a wide FoV of 2.4 sr (at 1 GeV) and detects γ-ray photons with energies from 20 MeV to 1 TeV. In principal, the LAT detects photons with pair conversion from the photons to e^+e^-, using interactions with tungsten. The detector comprises 16 silicon modules to track the secondary e^+e^- pairs that originated from incident photons and calorimeters made of CsI(Tl) crystals installed in the bottom of trackers. Each silicon tracker comprises 18 plates and is divided into three components. The first 12 and next 4 plates have thick (0.035 radiation lengths) and thin (0.18 radiation lengths) tungsten plates, respectively. This tracker design is for an increase in the effective area and the FoV at all energy ranges. The last two plates in front of the calorimeters do not have any converter. The direction of an incident photon is reconstructed from the tracked data of the e^+e^- pairs and the photon energy determined from cumulative energies in calorimeters and estimation of the energy-loss in tracker layers. The number of cosmic charged particles incident on the detector is roughly a factor of 100 larger than those of γ-ray photons; thus, those particles can be overwhelming background. To avoid contamination, the system is surrounded by an anticoincidence detector to distinguish signals induced by the charged particles from the photon signals[6].

For our likelihood analysis described after Chapter 7, it is important to consider the LAT-PSF[7] (Figure 5.6). The PSF is a monotone decreasing function of the photon energy. The solid and dashed lines are 68% and 95% containment angles out of the distribution of

[6]The description for the LAT design is in Atwood et al. [2009] in greater depth.
[7]https://www.slac.stanford.edu/exp/glast/groups/canda/lat_Performance.html

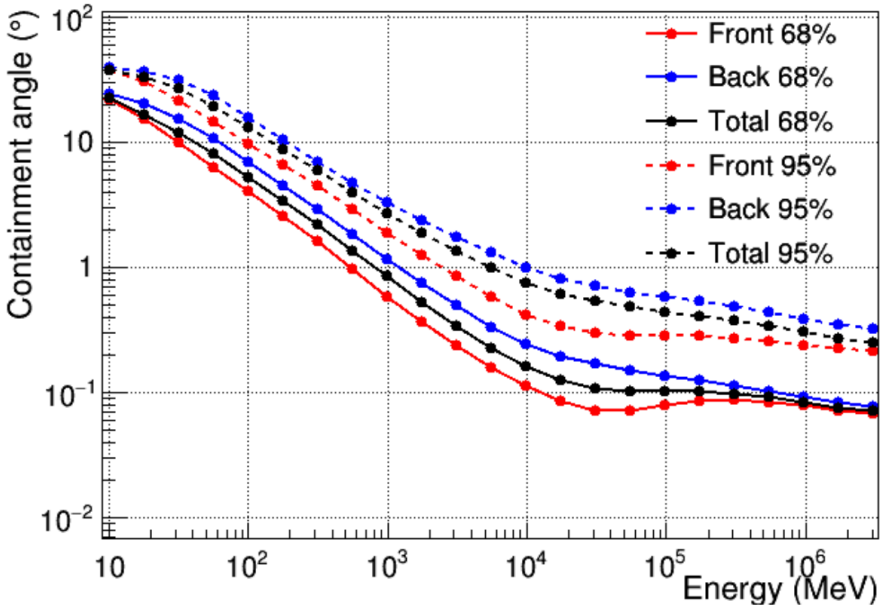

FIGURE 5.6: The LAT PSF from the LAT Collaboration web site (see the footnote for the URL).

detected photon locations, respectively. "Front" and "Back" mean two event conversion types that have different PSFs due to the thin and thick event-detection tungsten layers to increase the effective area and widen the FoV at all energy ranges. The PSF with 68% containment angles varies in the range of $0.1° < \theta < 1.5°$ in the energy range of our photon data (500 MeV $< E_\gamma <$ 500 GeV).

5.3.2 γ-ray data selection

In our composite likelihood analysis with the HSC- and DES-LSBG catalogs, we use different LAT data and data selections, which are listed in Table 5.2.

We select the photon event class `P8R3 SOURCE` for point-like source analysis recommended by the Fermi Collaboration, and employ a corresponding instrument response function (IRF) `P8R3_SOURCE_V2` or `P8R3_SOURCE_V3` to reduce photon count data. We also apply the quality-cut filter `DATA_QUAL>0 && LAT_CONFIG==1`. To avoid γ-ray contamination from photon emission produced by interactions of cosmic rays with Earth's atmosphere, we exclude photon events with zenith angles larger than 100°. We are careful in choosing the energy range of γ-ray photons because of following reasons. The

photon statistics decrease in the high energy regime. Meanwhile, lower energy photons introduce nonphysical biases in the analysis because such photons are likely to leak to the neighboring pixels due to the PSF broadening. According to the compromise between the photon statistics and angular resolution, the photon energy range is set to 500 MeV $< E_\gamma <$ 500 GeV with 24 logarithmic bins. For the region of the γ-ray sky in our analysis, we select regions of interest (ROIs) as $10^\circ \times 10^\circ$ or $15^\circ \times 15^\circ$ sky patches with 0.1° spatial grid, which fully includes areas LSBG samples distribute.

To construct the UGRB sky from the observed photon data, we need to estimate contributions from bright γ-ray sources to the total emission in our ROIs. The bright sources consists of three types of sources: the diffuse emission of galactic and isotropic component as well as resolved point sources by the LAT. For modeling of the source fluxes, we adopt the standard galactic (`gll iem v07.fits`) and isotropic template (`iso P8R3 SOURCE V2 v01.txt` or `iso P8R3 SOURCE V3 v01.txt`) for the Galactic and isotropic diffuse emission models, respectively. We derive model fluxes of resolved γ-ray sources from the 4FGL and 4FG-DR2 catalogs [Abdollahi et al., 2020, Ballet et al., 2020]. Then, we perform the maximum likelihood analysis in each ROI to fit spectral parameters for all the above mentioned flux models to the photon data. Note that in the likelihood analysis, for proper optimization of the model parameters within regions LSBG samples locate, we need to consider nearby bright sources without those regions. Therefore, in addition to the bright sources above, we perform an analysis with cataloged sources located within $15^\circ \times 15^\circ$ or $20^\circ \times 20^\circ$ areas, with the same centeroids to corresponding ROIs, in the case of ROI of $10^\circ \times 10^\circ$ and $15^\circ \times 15^\circ$, respectively. See details for our UGRB construction procedure in Appendix A. To analyze the photon data, we use a open-source software, `fermipy` (v0.17.4 or v1.0.1), which is based on the `Fermi Science Tools (v115p3 or v2.0.8)`, including advanced analysis tools, especially those to find new sources and measure SEDs of objects of interest in our analysis.

Parameters	*HSC, known redshifts*	*HSC Catalog*	*DES Catalog*
ROI size	$10^\circ \times 10^\circ$	$10^\circ \times 10^\circ$	$15^\circ \times 15^\circ$
Start of observation	08-04-2008	08-04-2008	10-27-2008
End of observation	08-02-2016	08-02-2016	07-06-2021
Pixel size	0.1°	0.1°	0.1°
Energy range	500 MeV - 500 GeV	500 MeV - 500 GeV	500 MeV - 500 GeV
Number of energy bins	24	24	24
Event class	P8R3 SOURCE	P8R3 SOURCE	P8R3 SOURCE
Event type	Front+Back (3)	Front+Back (3)	Front+Back (3)
IRF	P8R3_SOURCE_V2	P8R3_SOURCE_V2	P8R3_SOURCE_V3
Zenith angle cut	100°	100°	100°
Filter applied 1	`DATA_QUAL>0`	`DATA_QUAL>0`	`DATA_QUAL>0`
Filter applied 2	`LAT_CONFIG==1`	`LAT_CONFIG==1`	`LAT_CONFIG==1`
Fermitools version	v11r5p3	v2.0.8	v2.0.8
fermipy version	v0.17.4	v1.0.1	v1.0.1
Source model template			
Galactic diffuse	gll_iem_v07	gll_iem_v07	gll_iem_v07
Isotropic diffuse	iso_P8R3_SOURCE_V2_v01	iso_P8R3_SOURCE_V2_v01	iso_P8R3_SOURCE_V3_v01
Source catalog	4FGL	4FGL	4FGL-DR2

TABLE 5.2: Table of the configuration of the LAT data selection and parameters for our analyses. *"HSC, known redshifts"* means the analysis with eight HSC LSBGs with measured redshifts in Chapter 6. *"HSC Catalog"* and *"DES Catalog"* mean analyses with the HSC- and DES-LSBG catalogs, respectively, with dN/dz measurement in Chapter 7. Details for the parameters are seen in the texts.

Chapter 6

DM Constraint with individual LSBGs

In this chapter, we explore the γ-ray photon data from the LAT observation with individual LSBGs with known redshifts described in Section 5.1.1, to perform the annihilation signal search considering the annihilation channel of $b\bar{b}$. In Section 6.1, we describe a method to compute the J-factors for the LSBGs and estimate a scatter of the J-factor values propagated from uncertainties of halo properties. In Section 7.3, we perform the composite likelihood analysis with all objects. Finally, discuss the upper limit on the cross section using a single and stacking eight objects in Section 6.3. Note that descriptions in this chapter are based on Hashimoto et al. [2020].

6.1 DM annihilation γ-ray flux from individual LSBGs

First, we specify a practical J-factor formulation for our LSBGs (see Equation 2.20 for the general representation of the J-factor). In our analysis, we assume the Navarro-Frenk-White (NFW) profile [Navarro et al., 1996] as the smoothed DM density profile within the LSBG DM halo:

$$\rho_{\rm DM}(r) = \frac{\rho_s}{cr/r_{\rm vir}\left[(cr/r_{\rm vir})+1\right]^2}, \tag{6.1}$$

where ρ_s, $r_{\rm vir}$ and c are the scale density, virial radius, and concentration parameter, respectively. The concentration parameter largely depends on the halo mass. We adopt the parameter of the mass-concentration relation from Dutton and Macciò [2014b], which is calibrated using high-resolution N-body simulations. In this study, we consider that the halo mass is the entire mass within $r_{\rm vir}$, $M_{\rm halo} = 4\pi \int_0^{r_{\rm vir}} \rho_{\rm DM}(r) r^2 dr$. Given the halo mass, c is uniquely determined from the mass-concentration relation, and accordingly, ρ_s is also specified.

As described in Section 5.3, the LAT PSF varies in the range of $0.1^\circ < \theta < 1.5^\circ$ in the energy ranges we consider, whereas the angular sizes of our LSBGs are much smaller than 0.1°. Hence, we consider our target objects to be point-like sources in the likelihood analysis with the LAT data. Then, the integration of $\rho^2_{\rm DM}$ over the target volume in Equation 2.20 reduces to the following:

$$\int ds \int d\Omega \rho^2_{\rm DM}(s, \Omega) \rightarrow \int dV \rho^2_{\rm DM}(r)/d_A^2, \tag{6.2}$$

where d_A, s and Ω are the angular diameter distance to the object, line-of-sight vector and object angular scale, respectively. Then the J-factor is reduces as follows,

$$J = (1 + b_{\rm sh}) \frac{M_{\rm halo}}{d_A^2} \frac{\Delta \rho_{c,z} c^3}{9} \left[1 - \frac{1}{(1+c)^3}\right] \left[\log(1+c) - \frac{c}{1+c}\right]^{-2}, \tag{6.3}$$

where $\rho_{c,z}$ is the critical density in the universe at z. Δ is the over-density of the spherical collapse to be assumed as 200. In the smoothed density profile, substructures that are local high-density regions are not considered. Such substructures can cause an excess of the total γ-ray flux within the DM halo, because the annihilation rate per time is proportional to the square of the number density of DM particles. Therefore, this increase in γ-ray photons (the so-called *boost factor*) can play a considerable role in the annihilation-signal probe, which has been searched using high-resolution N-body simulations. We introduce the boost factor $b_{\rm st}$ set to unity for our LSBGs from Hiroshima et al. [2018], who have used an analytical model to account for the tidal mass-loss rate of subhalos and numerical N-body simulations on different scales. Because $b_{\rm sh}$ is a monotone increasing function of the halo mass and $b_{\rm sh}$ at halo mass of 10^9 $M_\odot$ is ~ 1, our assumption of $b_{\rm st} = 1$ is conservative in the halo-mass range of our LSBGs ($\sim 10^9 < M_{\rm halo}[M_\odot] < 10^{11}$).

In the next step, we describe how to estimate halo masses of LSBGs from the observed

fluxes in optical bands. First, we convert the observed g, r and i band magnitudes in Table 5.1 into V band magnitude as follows [Jester et al., 2005]:

$$V = g - 0.59(g - r) - 0.01. \tag{6.4}$$

Given the luminosity distance to object d, we can convert the apparent magnitude to the absolute magnitude M_V, using the well known relation $M_V = V + 5 - 5\log_{10} d$. To estimate the stellar mass M_* from M_V, we set the mass-to-light ratio to unity from Woo et al. [2008], in which the mass-to-light ratio of local dwarf galaxies whose ratios are estimated approximately one. Then, we obtain $M_* = L_L/L_\odot$ $[M_\odot]$, where L_L is the luminosity of LSBG. Finally, we apply the stellar-to-halo mass ratio [Moster et al., 2013] for the crude estimate of the total halo mass of our sample.

We show the stellar masses, halo masses, and J-factors of the eight LSBGs in Table 6.1. We note that the median values of the stellar masses for LSBG-285 and LSBG-750 are both $\sim 4 \times 10^7$ $M_\odot$, and halo masses are estimated to be $\sim 2.5 \times 10^{10}$ $M_\odot$. These values agree with those in Greco et al. [2018b], which is the rotation curve study described in 5.1.1.

For statistical uncertainties of J-factor, we consider the following three uncertainties: 1) the i-band magnitude Gaussian error of 0.24 at 1-σ level for all objects from Greco et al. [2018a], 2) the scatter in the stellar-to-halo mass conversion and 3) the uncertainty of the concentration parameter of $\Delta \log c = 0.1$ at 1-σ Gaussian error [Dutton and Macciò, 2014a]. With the Monte-Carlo simulation of 500 times, for the halo mass and J-factor uncertainties, we evaluate $\Delta \log M_{\rm halo} \sim 0.4$ and $\Delta \log J \sim 0.7$ at 1-σ Gaussian error, respectively. Note that we fix all distances of the eight objects to values in 5.1.

6.2 composite likelihood analysis

From Equation 2.19, the predicted DM energy annihilation spectra are independent of the search target, only the J-factors present differences in our LSBGs. This characteristic allows us to combine data from all individual LSBGs in order to set stronger constraints on the DM model parameters. After first analyzing every individual LSBG, a composite

LSBG ID	$\log_{10}(M_*[M_\odot])$	$\log_{10}(M_{\rm halo}[M_\odot])$	$\log_{10}(J[{\rm GeV}^2{\rm cm}^{-5}])$
171	9.3	11.1	14.4
285	7.6	10.4	15.7
456	9.1	11.1	14.7
464	9.1	11.0	14.8
575	7.4	10.3	15.5
613	9.3	10.7	14.7
729	9.3	10.7	14.8
750	7.6	10.4	15.4

TABLE 6.1: The stellar masses, halo masses, and J-factor values for the eight LSBGs with known redshifts. Each parameter is a median value in the Monte Carlo simulation.

analysis is subsequently performed following the methods employed by the Fermi Collaboration in dSphs Ackermann et al. [2015d]. Specifically, our pipeline adds together the photon counts from the signal and background regions for each LSBG and then computes upper limits on the DM annihilation rate following the same prescription of individual sources. We note that this composite likelihood technique takes into account that every LSBG has a different J-factor computed from Equation 6.3. In addition, we consider only $b\bar{b}$ channel among the final states of the annihilation process. Almost all of LSBGs in our analysis are found to have very low statistical significance detection in the LAT data (see Appendix B). Therefore, in the computation of the 95% C.L. upper limits of the DM annihilation cross-section, we employ the Bayesian method Helene [1983] recommended in the 2FGL catalog Nolan et al. [2012] for analyses of faint point-like sources.

Using our bin-by-bin method, we perform likelihood scans as a function of putative DM fluxes associated with each LSBG in every individual energy bin. Because all likelihood values obtained at each ROI are assumed to be independent of each other, the joint likelihood $\mathcal{L}_{\rm st}$ for the full sample of targets can be expressed as follows:

$$\log \mathcal{L}_{\rm st}(\alpha|\langle\sigma v\rangle, J) = \sum_{ij} \mathcal{L}(\alpha_{ij}|\langle\sigma v\rangle, J_i), \tag{6.5}$$

where α_{ij} is the putative flux amplitude of the i-th LSBG at j-th energy bin, which is obtained from the UGRB flux at the object position. Here, we define a delta-likelihood, $\Delta \log \mathcal{L}_{\rm st}(\alpha|\langle\sigma v\rangle, J) \equiv \log \mathcal{L}_{\rm st}(\alpha|\langle\sigma v\rangle, J) - \log \mathcal{L}_{\rm st,0}$, where $\mathcal{L}_{\rm st,0}$ is the composite likelihood

for zero flux of the annihilation flux.

In this formulation, we assume that all our LSBGs are statistically independent of each other. Since our LSBGs are treated as point-like sources, this assumption is correct if the angular separations between LSBGs are larger than the LAT PSF at the energy range in question. In our analysis, we assume that the LSBG flux is positive definite. This implies that in the limit of large number counts, the data is well-described by a $\chi^2/2$ distribution from the Wilks theorem [Wilks, 1938]. In this sense, the 95% C.L. upper limits on the DM cross-section can be obtained when the total likelihood $\Delta \log \mathcal{L}_{\rm st}(\alpha|\langle\sigma v\rangle) \sim 3.8/2$ (for 1 degree of freedom). We estimate the astrophysical uncertainties associated with the upper limits computed this way by performing Monte Carlo simulations of the J-factor distributions for the eight LSBGs.

6.3 Result

The LSBG sample considered in this chapter are not significantly detected in γ-rays (see Figure B.1). The computation of the upper limits is done using the methods explained in the previous section. Figure 6.1 displays the 95% C.L. upper limits on $\langle\sigma v\rangle$ as obtained for individual LSBG (dashed lines) using their respective median J-factor. The joint upper limit for the full sample (black solid line) was obtained using the joint likelihood method described in Equation 6.5. The green band displays the impact on our limits due to astrophysical uncertainties in the DM model parameters. As discussed earlier, these come mainly from uncertainties in the halo mass and the matter concentration of the LSBGs. As it can be seen, the objects LSBG-285 and LSBG-575 place the strongest constraints on $\langle\sigma v\rangle$ and also provide dominant contributions to the joint constraint. Even after stacking over the full sample of eight LSBGs, our joint constraints are weaker than the ones obtained using more traditional targets like dSphs or nearby galaxy groups and clusters of galaxies Ackermann et al. [2015d], Lisanti et al. [2018], Hoof et al. [2020]. Using the alternative Galactic diffuse emission models, we repeat our $\langle\sigma v\rangle$ upper limits calculation and find that those are affected at the few percent level for DM mass values smaller than 100 GeV, while no difference is apparent for larger DM masses. This is shown by the black dotted lines in Figure 6.1.

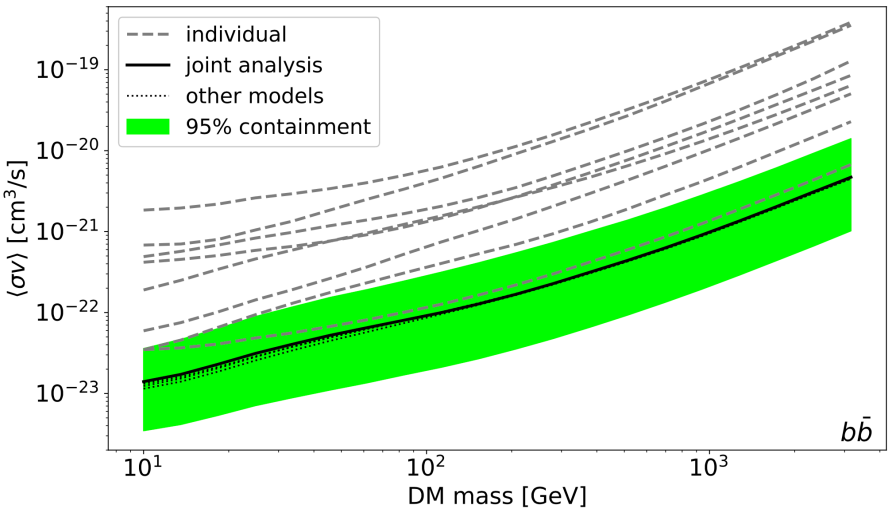

FIGURE 6.1: 95% C.L. upper limits on the DM annihilation cross-section in the $b\bar{b}$ channel. The black solid line represents the upper limit obtained with a composite analysis assuming the median J-factor values of each LSBG, while the gray dashed lines display the upper limit obtained for each LSBG in the eight samples with known redshifts. The black dotted lines show the joint upper limits obtained after replacing our baseline galactic diffuse emission model with three alternative background models simulated with GALPROP. The green band shows the uncertainty of the upper limit due to uncertainties in the J-factor, which is estimated by Monte Carlo sampling of the individual J-factors.

Chapter 7

DM Constraint with overall LSBG catalog

In this chapter, we perform the DM cross-section constraint with unknown redshift samples of the HSC- and DES-LSBG catalogs. For each object redshift, we randomly assign the redshift from the redshift distribution of overall the sample, without measuring individual redshifts. As described in Section 5.1, we use the HSC-LSBG catalog to validate our method and to clarify the scaling relation between the DM constraint and the number of objects used in the analysis. Moreover, in the analysis with the DES-LSBG catalog, we obtain the main result of the current DM constraint with the largest LSBG catalog.

7.1 Digest of our technique

In this section, we briefly describe our technique. First, we measure dN/dz amplitudes of our LSBG catalog in five redshift bins with equal width of 0.03 (total redshift range of $0 < z < 0.15$), by using the clustering redshift method. Then, we randomly assign redshifts to individual objects from the redshift distribution obtained by the dN/dz measurement (see Section 7.2). Furthermore, we model the annihilation γ-ray flux of each object, using optical band magnitudes and the assigned redshift of each object (see Section 6.1). Note that these flux models have a single parameter of $\langle \sigma v \rangle$ for each.

On the other hand, we estimate UGRB fluxes around individual LSBG positions using the Fermi γ-ray observation, which are used by obtaining the putative flux of each LSBG. These fluxes are used as a prior in our likelihood analysis. For construction of UGRB fields in our ROIs, we need to estimate bright sources that consist of the Galactic and isotropic diffuse emissions as well as resolved-source emissions in the LAT observation; thus, we derive the optimal flux models for these sources in each ROI, and perform the maximum likelihood method to optimize the model parameters. The UGRB flux field is obtained by subtracting the total flux of above sources from the observed photon-flux field (see Appendix A).

After constructing the UGRB field, we compute the likelihood function of each LSBG model by the Bayesian method, which is recommended in cases of treating very faint sources, such as LSBGs and dSphs, by the Fermi Collaboration [Nolan et al., 2012]. For obtain the prior distribution of the likelihood, we put a test-source model, which has a power-law spectrum with a single amplitude parameter, on each LSBG position and fit the parameter to the UGRB flux filed. Then, we introduce the LSBG flux model for the DM annihilation and compute the likelihood for each LSBG using the prior distribution (see Section 7.3 and Appendix B). Under an assumption of independence of each LSBG model parameter in our likelihood analysis, we calculate the composite likelihood for multiple objects and provide the constraint on the LSBG model parameter, i.e., $\langle \sigma v \rangle$. We describe the validity check of our procedures in Section 7.4.

7.2 Clustering redshift method

In this section, we describe a method to estimate the dN/dz distribution from spatial clustering, the so-called the clustering redshift method. Given two galaxy samples in an overlapped region. Even if the galaxies in the two galaxy samples are statistically different, they both correlate with the underlying DM distribution. In the case where one galaxy sample has known redshifts and the other has unknown redshifts, taking the cross-correlation between the two galaxy samples gives a statistical estimate of the redshift distribution of the galaxies with unknown redshifts. We denote the galaxy samples with known and unknown redshifts as '*spectroscopic sample*' and '*photometric sample*', respectively. The angular cross-correlation function can be factorized as follows [Newman,

2008],

$$w(\theta) = \int_0^\infty dz \frac{dN_p}{dz} \frac{dN_s}{dz} b_p(z) b_s(z) w_{\rm DM}(z, \theta), \tag{7.1}$$

where subscripts 's' and 'p' represent spectroscopic and photometric samples, respectively. $\frac{dN}{dz}$ represents the redshift distribution normalized to unity, $b(z)$ is a linear bias, and $w_{\rm DM}(z, \theta)$ is the angular DM correlation function. Notably, the mass of the employed DM model is high enough not to affect the DM clustering pattern itself. We define an integrated cross-correlation $\bar{w}$ with a weighting function $W(\theta)$ as follows

$$\bar{w} = \int_{\theta_{\rm min}}^{\theta_{\rm max}} d\theta \; W(\theta) w(\theta), \tag{7.2}$$

where the weight W is introduced so that the signal to noise ratio of $\bar{w}$ can be optimized. Following [Ménard et al., 2013], we empirically adopt $W = \theta^{-1}$. In practical measurement, we divide the spectroscopic sample into narrow redshift bins so that dN_s/dz can be approximated by the narrow top-hat function; $dN_s^i/dz \simeq 1/\Delta z$ if $z_i < z < z_{i+1}$. Now we rewrite Equation 7.2 at $z = z_i$ as follows

$$\bar{w}(z_i) \approx \frac{dN_p}{dz}(z_i) b_{\rm p}(z_i) b_{\rm s}(z_i) \bar{w}_{\rm DM}(z_i), \tag{7.3}$$

where $\bar{w}_{\rm DM}(z)$ can be defined similarly as Equation 7.2 by replacing $w(\theta)$ with $w_{\rm DM}(z, \theta)$.

To compute $w(\theta, z)$, we take the cross correlation between the sample in each bin and the entire LSBG sample. The angular cross correlation is computed by the estimator [Landy and Szalay, 1993] in angular bins of $0.1^\circ < \theta < 1.0^\circ$ (10 logarithmic bins) and $0.1^\circ < \theta < 5.0^\circ$ (20 logarithmic bins) for measurement with the HSC and DES LSBGs, respectively, logarithmically uniformly sampled,

$$w(z_i, \theta_j) \equiv w_i^m = \frac{{\rm D}_p{\rm D}_{si} - {\rm D}_p{\rm R}_{si} - {\rm R}_p{\rm D}_{si} + {\rm R}_p{\rm R}_{si}}{{\rm R}_p{\rm R}_{si}}, \tag{7.4}$$

where DD and DR represent the normalized number of pairs separated within the $j-$th angular bin between data and data or data and random, respectively. Subscripts pi and si represent the photometric sample and reference sample in the $i-$th redshift bin, respectively. We omit the argument of θ_j on the right hand side where no confusion arises.

$\bar{w}_{\rm DM}(z)$ is fully predictable from the standard cold DM theory including the nonlinear matter clustering evolution. Otherwise, $\bar{w}_{\rm DM}(z)$ can be treated as a *constant* with varying

redshift if the redshift range we are goint to estimate is small enough. A better estimation might be to replace $\bar{w}_{\rm DM}(z)$ with the square of the linear growth factor, $D^2(z)$. Before concluding to directly connect measurement to the dN_p/dz, we need to address the bias functions. The bias of the spectroscopic sample b_s can be measured using the sample auto-correlation. However, rather than estimating b_s, we assume the redshift evolution of the bias can be negligible as the redshift range is small $0 < z < 0.15$. The redshift evolution of the photometric sample b_p is fully degenerated with the dN_p/dz and cannot be further decomposed.

We compute a statistical uncertainty of $w(z, \theta)$ by the `treecorr` jackknife method with 100 jackknife subsamples, which corresponds to sky coverage of each patch of ~ 2 deg^2 and ~ 50 deg^2 for the HSC and DES samples, respectively. For measurement with the DES LSBGs, the full convariance matrix of the cross correlation between different angular and redshift bins is written as follows,

$$C_{ij}^{ml} = \frac{K-1}{K} \sum_{k=1}^{K} [w_{ik}^{m} - \widehat{w}_i^m][w_{jk}^{l} - \widehat{w}_j^l], \tag{7.5}$$

where w_{yk}^{x} is the correlation function in the x-th redshift and y-th angular bins for the k-th jackknife subsample. $\widehat{w}$ is the averaged correlation function over K jackknife subsamples ($K = 100$ in our analysis). By contrast, for measurement with the HSC LSBGs, we do not consider the redshift cross-covariance, so that we estimate the covarianve matrix for $m = l$.

Here, we consider assignment of object redshifts to our LSBGs. For the covariance matrix of $\bar{w}(z_i)$ between different redshift bins, we integrate C_{ij}^{ml} over all angular bins though,

$$\bar{C}_{ml} = \sum_{ij} W(\theta_i) W(\theta_j) C_{ij}^{ml}. \tag{7.6}$$

We consider a multivaluate Gaussian distribution as a prior distribution with five amplitude parameters $\mathbf{X} = \{X_m\}$,

$$\mathcal{P}(\mathbf{X}|D) \propto \frac{1}{\sqrt{\det(\bar{\mathbf{C}})}} \exp\left(-\frac{1}{2}(\mathbf{X} - \boldsymbol{\mu})^{\rm T} \bar{\mathbf{C}}^{-1} (\mathbf{X} - \boldsymbol{\mu})\right), \tag{7.7}$$

where μ_m is the amplitude converted from the integrated $\widehat{w}_i^m$ using Equation 7.2. To prohibit negative amplitudes of dN/dz, we require stepwise prior, $\Theta(\mathbf{X}) = 0$ for $X_i < 0$. Then, the posterior distribution of the parameters is given by $\mathcal{P}(\mathbf{X}|D)\Theta(\mathbf{X})$. We finally apply linear interpolation between each redshift-bin center to the posterior distribution. For conservative analysis, we consider the minimum distance to object to be 25 Mpc, which is the nearest object with a precise redshift in the HSC-LSBG catalog. In Figure 7.1, we show the measured dN/dz for the HSC- and DES LSBG samples. The error bars denote statistical uncertainties with 1-σ level derived from the error propagation of the jackknife errors of the angular cross-correlation. Note that these dN/dz is still not normalized to unity.

For the angular cross-correlation of the HSC- and DES-LSBG samples as well as the full covariance matrix C_{ij}^{ml} and $\bar{C}_{ml}$ of the correlation, we show the result of our measurement in Appendix C.

7.3 Uncertainties of constraint on DM cross-section

To evaluate statistical uncertainties for the upper limit on the cross section in the composite likelihood analysis, we consider uncertainties of the halo mass and concentration parameter in addition to the dN/dz measurement uncertainty described in Section 7.2, with 500 Monte Carlo simulations. For the halo mass, we evaluate its uncertainty as $\Delta \log M_{\rm halo} = 0.4$ at 1-σ Gaussian error by computing the scatter of stellar-to-halo-mass conversion from Hashimoto et al. [2020]. For the concentration-parameter error, we adopt a $\Delta \log c$ of 0.1 at 1-σ Gaussian error [Dutton and Macciò, 2014a].

In Figure 7.2, we show the J-factor values summed over $N_{\rm st}$ samples. In the order of square, cross, and circle symbols, the error-bars plot the total values including halo property uncertainty, dN/dz measurement uncertainty, and both, respectively. The black, red and blue error-bar plots represent the total values with all ($N_{\rm st} = 781$), red ($N_{\rm st} = 450$) and blue ($N_{\rm st} = 331$) HSC-LSBG samples, respectively. For the red and blue samples, we display only the values with both the uncertainties. For comparison with relevant works for probing constraint on the DM annihilation cross-section, we display the upper limit on the DM cross-section with 95% C.L. for DM mass of 1 TeV in the right axis, which

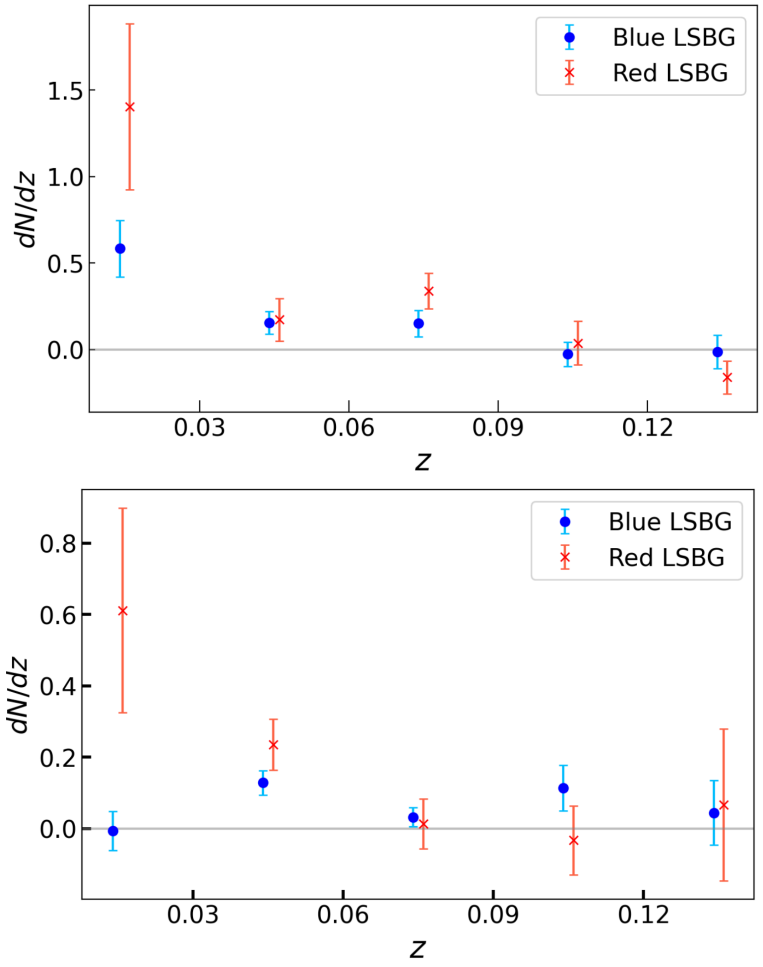

FIGURE 7.1: dN/dz of HSC (*Top*) and DES (*Bottom*) LSBG samples. In each panel, the red and blue error-bar plots are amplitudes of dN/dz for the red and blue samples, respectively.

corresponds to the J-factor value on the left axis. Note that for converting J-factor values to the upper limits, we apply a mean UGRB flux at the LSBG positions. The upper limit is affected by the UGRB fluctuation at the sample position, which is $\sim$1 dex and $\sim$0.6 dex at 2-σ level at DM masses of 10 GeV and 1 TeV, respectively.

7.4 Validity check

In our likelihood analysis, we performed the composite analysis assuming that the likelihood functions of individual objects are independent of each other. This assumption is

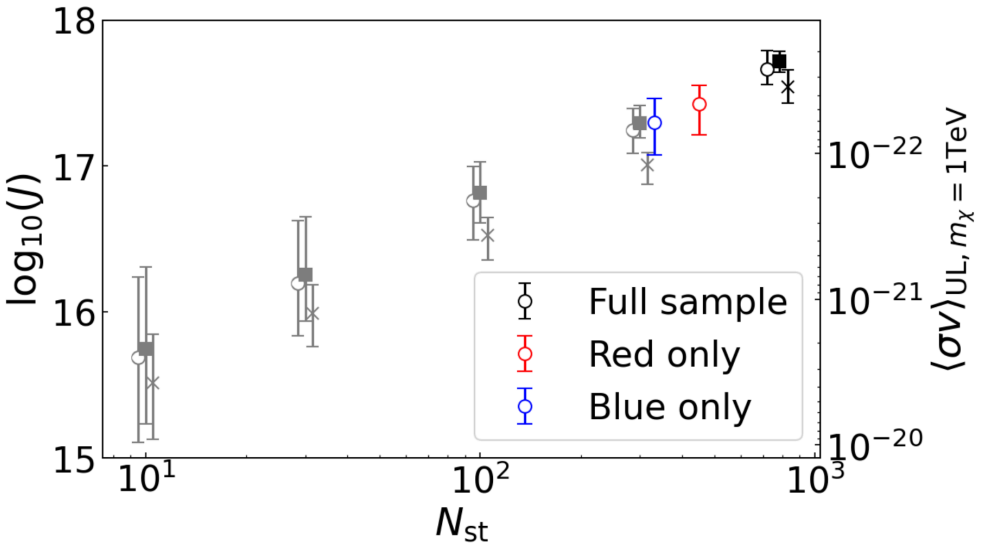

FIGURE 7.2: Total J-factor values summed over $N_{\rm st}$ sample. The values of all HSC LSBGs in black error-bar plots. The error bar with filled square includes halo property uncertainty, cross symbol includes dN/dz measurement uncertainty and circle symbol includes both. Each error bar shows a 95% confidence region based on 500 Monte Carlo simulations. The blue and red error-bar plots correspond to the values with the blue and red samples, respectively. The gray error-bar plots are the total values summed over 10, 30, 100, and 300 samples randomly taken from 781 samples in the simulations in order from left to right. The right axis shows $\langle\sigma v\rangle_{\rm UL}$ for DM mass of 1 TeV with 95% C.L. in the mean UGRB flux corresponding to J-factor value in the left axis. We apply $b\bar{b}$ to the annihilation channel.

expected to be valid when the mean separation of the sample is sufficiently larger than the LAT-PSF of $\sim 1^\circ$. In our case, however, the separation of both catalogs are $\sim 0.5^\circ$. Therefore, we perform validation check of this assumption, using the HSC-LSBG sample.

7.4.1 Correlation between neighbors

In the HSC-*Fermi* sky coverage, we select 10 independent patches with the size of 10×10 deg^2. From each patch, we randomly select 60 pairs of points with separations of 0.5° to 3°. To evaluate the correlation between the putative flux amplitudes of paired objects, we perform the composite likelihood analysis for the pairs, which simultaneously optimizes the fluxes of the paired objects. The putative flux of an object in the i-th energy bin is

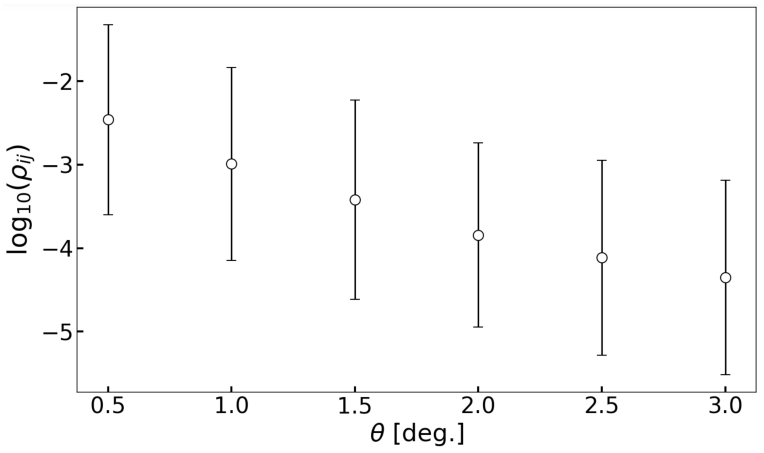

FIGURE 7.3: The off-diagonal value of covariance matrix between two amplitude parameters for each paired objects as a function of separation angles. The error bars represent 1-σ errors of the off-diagonals with 60 pairs in each angular bin.

parameterized as follows,

$$\frac{d\Phi}{dE} = \alpha \left(\frac{E}{1000[\mathrm{MeV}]} \right)^{-2}. \tag{7.8}$$

Figure 7.3 shows the absolute value of an off-diagonal value of the correlation matrix between two amplitude parameters as a function of the separation. The error bars are computed from the 60 independent pairs that reflect the fluctuations of the residual gamma-ray flux. The cross-covariance is normalized by the diagonal terms, i.e., $\rho_{ij} \equiv \mathrm{cov}(\alpha_i, \alpha_j)/\sigma_i\sigma_j$, where superscripts i and j are the indexes of test objects. Although we expect a strong correlation on scales smaller than 1° because of the LAT-PSF size, even the correlation at the smallest separation, which corresponds to the HSC-LSBG mean separation, is less than 0.1 at 1-σ level. We note that almost all off-diagonal covariance are negative due to the total flux conservation in the likelihood analysis.

7.4.2 *Simultaneous* analysis versus *Independent* analysis

For further validation, we perform a composite likelihood analysis in which we obtain the likelihood profiles for putative fluxes of all samples within a single LAT data patch simultaneously. Figure 7.4 compares the cross-section constraints with this simultaneous method ('simultaneous' case) with that obtained based on the assumption that all objects are independent of each other ('independent' case). We emphasize that the 'independent'

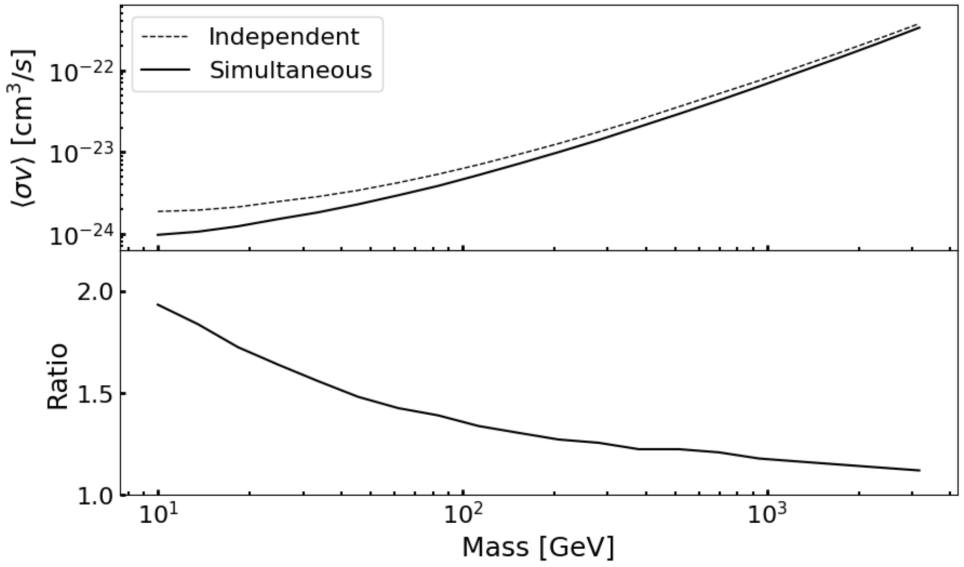

FIGURE 7.4: (Top) The difference between the cross-section constraints at the $b\bar{b}$ channel in the composite analysis with all LSBGs in the "simultaneous" case (solid line) and that with assumption of flux likelihood profiles of all LSBGs being independent of each other (dotted line) as a function of DM mass. (Bottom) The ratio of the upper limits in the two cases.

case provides a weaker constraint than that in the 'simultaneous' case. This is because the total flux conservation is imposed, which results in the larger putative flux amplitude in the 'independent' case than 'simultaneous' case. Note that in this calculation, we set all objects' J-factor to $10^{14.5}$ GeV^2/cm^5 and choose a specific dN/dz.

We conclude that the correlation between neighboring points is less than 10% on scales 0.5°; in addition, even if we ignore the correlation, which is computationally much less expensive, we will obtain the conservative constraints.

7.5 Scaling relation in composite analysis

In this section, we discuss a scaling relation of the statistical power on $\langle\sigma v\rangle_{\rm UL}$ as a function of the number of stacking $N_{\rm st}$ under the low background photon limit. We show that $\langle\sigma v\rangle_{\rm UL}$ is proportional to $1/N_{\rm st}$ at a high mass limit but scales with $1/\sqrt{N_{\rm st}}$ at low mass ranges. We also show that this scaling relation converges to $1/N_{\rm st}$ whatever the

DM mass if $N_{\rm st}$ is sufficiently large that is due to the observed photon count to be almost zero around LSBGs in some fraction in higher energy regime. This scaling relation is significant for the DM constraint using a number of LSBGs.

First, we revisit a Poisson likelihood for the flux model of a single LSBG in the UGRB. The likelihood function for model parameters is given by the Poisson distribution,

$$\mathcal{L} = \prod_i \frac{\lambda_i^{n_i} \mathrm{e}^{-\lambda_i}}{n_i!}, \tag{7.9}$$

where the index i runs over all energy bins and pixels and n_i is the observed photon counts; λ_i is the expected photon counts for model fluxes, which is decomposed into the Galactic foreground, isotropic background and resolved point-like source model fluxes as well as the flux by the DM annihilation in the single LSBG. A UGRB sky is derived from the modeling of all γ-ray sources, except for the LSBG flux, by the maximum likelihood process using the LAT data (see details of the UGRB construction in Appendix A). Note that the LSBG flux model has a single parameter $\langle\sigma v\rangle$ and, as seen in Equation 2.20, the flux is proportional to $\langle\sigma v\rangle$. After fixing all the model parameters $\boldsymbol{\Theta}$ except for $\langle\sigma v\rangle$, λ_i depends only on $\langle\sigma v\rangle$. We denote $\lambda_i = \lambda_i^{\rm others}(\boldsymbol{\Theta}) + \lambda_i^T(\langle\sigma v\rangle)$, where $\lambda_i^{\rm others}$ is the total model flux of all the sources without the LSBG and λ_i^T is the LSBG model flux. For simplicity, we consider that all LSBGs have the same J-factor, which means that their model fluxes are equal. As shown in Figure 7.5, we consider the fact that, in energy regimes higher than ∼30 GeV, the LAT hardly detects photons. Given that there is no photon count ($n_i = 0$) in such energy regimes and in all pixels, we expect $\lambda_i^{\rm others}(\boldsymbol{\Theta}) = 0$ and then $\log\mathcal{L} = -\sum_i \lambda_i^T(\langle\sigma v\rangle)$.

Consequently, we obtain the composite likelihood with $N_{\rm st}$ objects using Equation 6.5,

$$\Delta\log\mathcal{L}_{\rm st} = -N_{\rm st}\sum_i \lambda_i^T(\langle\sigma v\rangle), \tag{7.10}$$

where $N_{\rm st}$ is the number of objects in the composite analysis. Therefore, in our criteria (see Section 7.3) the upper limit is proportional to $1/N_{\rm st}$ because of $\lambda_i^T(\langle\sigma v\rangle) \propto \langle\sigma v\rangle$.

In Figure 7.6, we show the ratio of the upper limit on the DM cross-section with $N_{\rm st}$ objects to that with a single object for DM masses of 10 GeV, 100 GeV, and 1 TeV. We randomly select $N_{\rm st}$ objects from the HSC-LSBG sample and compute the upper limit

by the composite likelihood analysis with $N_{\rm st}$ objects, fixing J-factor values of all the objects to $10^{14.5}$ [GeV^2/cm^5]. We repeat this process in 500 times and in the figure, we show the median values of the ratio for each DM mass. With $N_{\rm st}$ larger than $\sim$30, the upper limits scale with the inverse of $N_{\rm st}$ for all mass ranges. For DM mass of 100 GeV and 1 TeV, this scaling relation is seen, even in smaller $N_{\rm st}$. This behavior is reasonable, considering less photon-count statistics in a high energy regime. The annihilation process with more massive DM particles can produce higher energy photons, thus probing the DM annihilation for more massive DM is affected by the photon-count statistics in high energy regimes.

7.6 Main result

Constraint with DES-LSBGs

In Figure 7.7, we provide upper limits on the annihilation cross-section in the black, red and blue solid lines, by the composite likelihood analysis of the annihilation γ-ray flux models for full, red and blue DES-LSBG samples, respectively. We show the total uncertainty for the upper limit with the full sample in the green shaded region of 95% containment in 1,000 Monte-Carlo simulations. Although the number of blue LSBGs are roughly two times larger than that of red LSBGs, the upper limits with both populations are similar, which reflects the difference of the measured dN/dz, and means that the red LSBGs are more abundant in low redshifts for the red LSBG than the blue LSBGs.

For conservative constraints, we consider all objects, except for ones with separation less than 1° from bright point sources, because UGRB flux around the sources may be underestimated due to oversubtraction by model fluxes of the sources, yielding a spuriously strong constraint. We show the upper limit with the limited sample of 16,353 objects in the dashed line in Figure 7.7. This upper limit is $\sim$30 % weaker than that with the full sample in all DM mass ranges, with a decrease in sample volume to $\sim$70% of the full sample size. The result implies that the constraint simply scales with an inverse of the sample volume, and shows that the use of the excluded objects in the composite analysis does not yield spuriously aggressive constraints in our analysis.

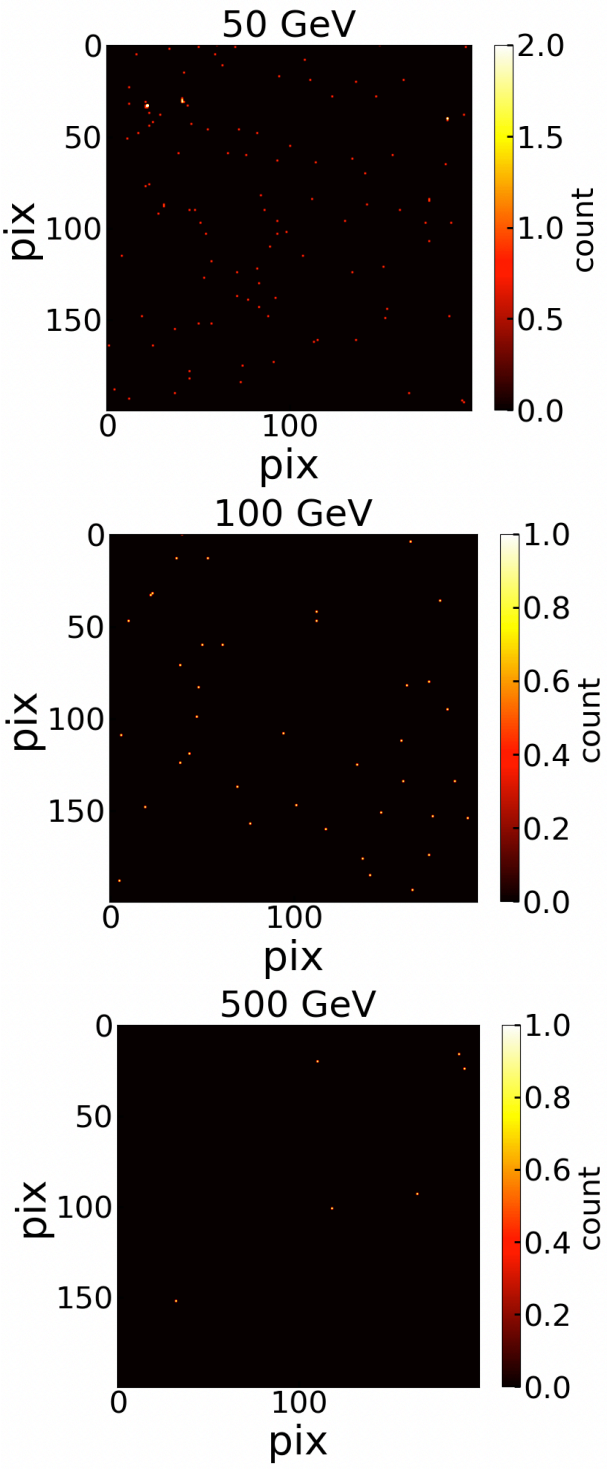

FIGURE 7.5: Sample of the observed-photon-count map in a single patch in our ROIs for $\sim 50, \sim 100$, and ~ 500 GeV from top to bottom. The vertical and horizontal axes represent spatial-pixel number and a single pixel is $0.1^\circ \times 0.1^\circ$.

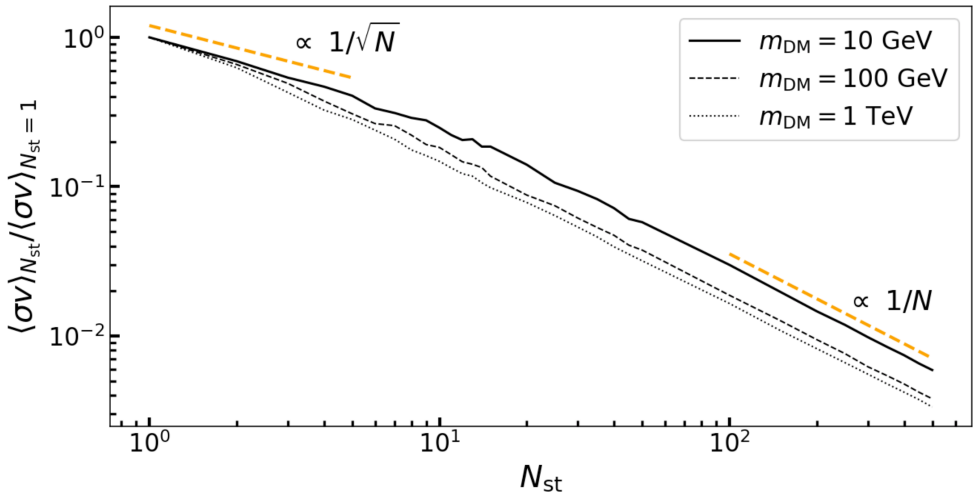

FIGURE 7.6: Scaling relation of the upper limit on the DM cross-section with the number of objects $N_{\rm st}$ in the composite analysis. The vertical axis is the ratio of the upper limit with $N_{\rm st}$ objects to the one with a single object. The black solid, dashed, and dotted lines correspond to the ratio for DM masses of 10 GeV, 100 GeV, and 1 TeV, respectively. Scaling with $1/N_{\rm st}$ and $1/\sqrt{N_{\rm st}}$ are shown in orange dashed lines.

Further, we consider variability of flux model parameters of bright sources in ROI as well as resolved sources around LSBGs to evaluate the impact to the DM constraint with the LSBG sample. As described in A, for estimate of the putative flux of a faint source, the variability may induce relatively large modification of the flux. Accordingly, we recalibrate the model parameters of the sources to allow for the variability (see more details for the recalibration processes in A). The dash-dotted line in Figure 7.7 represents the cross-section constraint with the full DES-LSBG sample and the UGRB fluxes without the recalibration. In all DM mass ranges, the constraint with the recalibrated UGRB is weaker than that without the recalibration. As the photon statistics are larger in lower energies, the recalibration affects to the likelihood analysis in the lower-energy bins and as a result, the upper limits in lower DM-mass regimes are weaker and weaker by comparing to those with the non-recalibrated UGRB.

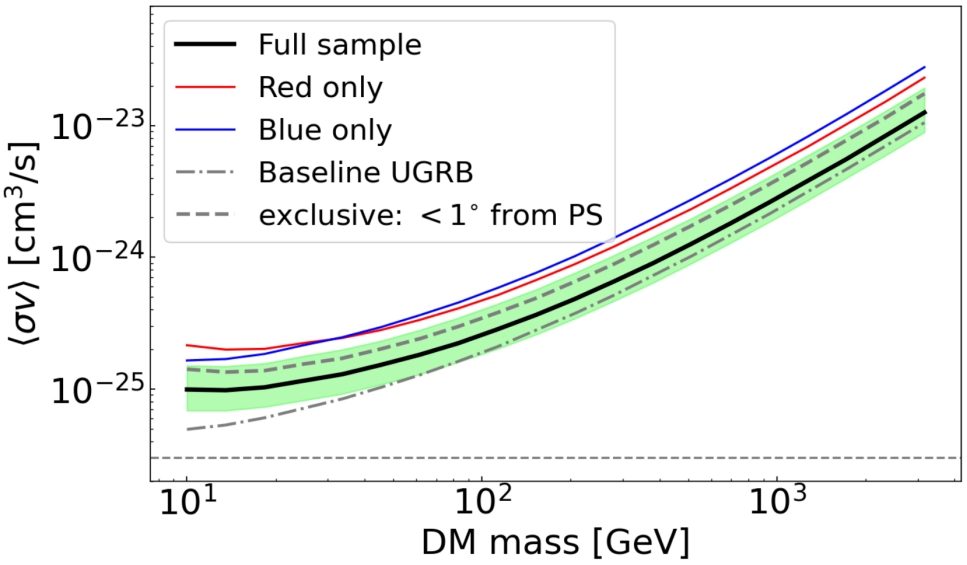

FIGURE 7.7: The upper limits on the velocity-averaged DM annihilation cross-section as a function of DM masses. The black, red, and blue solid lines present median values of the upper limits on the cross section with 95% C.L. in Monte Carlo simulations in the case of using the full, red, and blue samples of DES LSBGs, respectively. The shaded region represents a 95% containment region in the simulation for the full sample case. The upper limit with all samples, except for neighbors within 1° from resolved sources is shown as the dashed line. In the dash-dotted line, we show the constraint with all samples and the UGRB without the recalibration process described in Appendix A. Note that for all constraints except for one in the dash-dotted line, we use the UGRB flux with the recalibration. The horizontal line represents the thermal relic cross section. All upper limits are for the $b\bar{b}$ channel.

Chapter 8

Conclusion

Summary

In this thesis, for probing the DM annihilation γ-ray signal, we proposed using a number of LSBGs with unknown redshifts and presented a method with the objects to constrain the annihilation cross-section. LSBGs have favorable aspects for the purpose as follows. The halo masses of LSBGs are at least an order of magnitude larger than those of the MW dSphs, which have provided the most robust and relatively stringent constraint on the annihilating DM. In addition, LSBGs are highly DM-dominated systems and are expected to be γ-ray quiescent due to relatively few star-formation activities. Further, in the likelihood analysis with the estimated γ-ray flux from the DM annihilation in these objects and the UGRB field, LSBGs can be regarded as point-like sources because of the much smaller angular size of LSBGs than the LAT PSF. Finally, it has been indicated that the number of LSBGs can possess 30%-40% of the local galaxy population. Because the annihilation γ-ray flux from an object is inversely proportional to the square of the object distance, it is significant for the annihilating DM constraint to search for nearby objects. With the composite analysis using local numerous LSBGs with extragalactic γ-ray photons, we can obtain a strong and robust constraint on the DM cross-section.

In our strategy, for modeling the flux of γ rays that originated from the DM annihilation from LSBG with unknown redshift, we focused on the redshift distribution dN/dz of the overall LSBG sample and randomly assigned redshift to each object, instead of measuring

individual redshifts. The redshift distribution was obtained using the clustering redshift method, in which one measures the angular cross-correlation between an unknown redshift sample (LSBGs in our case) and a precisely measured redshift sample, and converted the correlation to the amplitudes of dN/dz.

In our analysis, we employed two LSBG catalogs produced from the HSC and DES observations. The HSC-LSBG catalog includes 781 objects with a sky coverage of $\sim$ 200 deg^2. This catalog was used to test a series of our procedures and validate our composite likelihood analysis. We found the scaling relation of the number of objects used in our analysis and the upper limit on the DM cross-section. On the other hand, the DES-LSBG catalog, including 23, 790 objects, was constructed from the DES Y3 Gold object catalog covering $\sim$ 5000 deg^2. This catalog was used to obtain the main results in this thesis.

For exploring the extragalactic γ-ray sky, we constructed the UGRB photon field from the photon data via the *Fermi*-LAT observation in an energy range of 500 MeV-500 GeV. In the analyses using the HSC- and DES- LSBG catalogs, we used the LAT data accumulated over about 8 and 13 years, respectively. The UGRB flux was obtained by subtracting the total model flux of the Galactic, isotropic diffuse and resolved-source emissions from the observed photon flux. For modeling the fluxes of the Galactic and isotropic emissions, we employed emission templates provided by the Fermi Collaboration. Similarly, for the resolved-source emission, we derived the 4FGL and 4FGL-DR2 catalogs for our likelihood analyses with the HSC- and DES-LSBG samples, respectively. Via the maximum likelihood analysis of all spectral parameters of flux models with the LAT photon data, we optimized parameters to obtain the UGRB flux. In the LAT data analysis, we used `fermipy`, which is based on the `Fermi Science Tools` supplied by the Fermi Collaboration.

Note that the 4FGL catalog was produced using the LAT data with the same time interval as our photon data for the HSC-LSBG catalog, whereas, for the DES-LSBG catalog, the time interval was $\sim$ 20% longer than that used for the 4FGL-DR2 catalog. Therefore, our photon data for the DES-LSBG catalog included new resolved sources with TS values above the point-source detection threshold ($TS \geq 25$) that were not listed in the 4FGL-DR2 catalog. With the point-source detection processes using `fermipy`, we detected 79 new point sources (about 11% of all resolved sources in our ROIs). After the UGRB

construction, we varied the background flux amplitude at the LSBG position to evaluate the likelihood profile of a putative flux of the sample in each energy bin. According to the prescription in Nolan et al. [2012], which considered the likelihood analysis of very faint sources, we applied the Bayesian method [Helene, 1983] in the composite likelihood analysis of our LSBG sample given the putative fluxes.

In the following, we summarize our method and its validation check with the HSC-LSBG catalog, and also our final result of the constraint on the DM cross-section with DES-LSBG catalog. Note that in the analyses with respect to the DM annihilation, we used a representative annihilation channel of $b\bar{b}$.

1) *Analysis with HSC-LSBG catalog*
First, using the HSC-LSBG catalog, we confirmed whether our procedure works well to constrain the DM cross-section. In dN/dz measurement for the LSBG samples, we employed the NSA sample as the reference sample in fully overlapping sky areas in which the LSBGs distribute. We divided into five redshift bins with equal width of $\Delta z = 0.03$ to measure the angular cross-correlation of the LSBG sample with the redshift-binned NSA sample. To evaluate the statistical error of the correlation, we applied the jackknife method with 100 jackknife subsamples. In the composite analysis with all LSBG sample, we considered the error propagation of the correlation uncertainty to dN/dz amplitudes as well as the uncertainties of the halo mass and concentration parameter. We found that the uncertainty in the upper limit was quite small (~ 0.3 dex), which implies that it is sufficient for the DM cross-section constraint to use the redshift distribution of the overall LSBG sample without knowing individual object redshifts.

In our likelihood analysis, we assumed that all spectral parameters for LSBG flux models are independent of each other, to reduce of the computational cost in estimating the putative fluxes in the UGRB field. However, the number density of the LSBG sample ($\sim 0.5^\circ$) is comparable to the LAT PSF scale, which may lead to a correlation between flux model parameters for neighboring LSBGs, and thus may break the assumption. We validated the assumption using two techniques. 1) We computed the covariance matrix between two amplitude parameters for paired LSBGs with certain angular separations and confirmed that the off-diagonals of the correlation matrix was smaller than 0.1 at the separation angle of 0.5°. 2) Fixing the J-factor of each object, we performed a composite likelihood analysis in which we obtained the likelihood profiles for the putative fluxes

of all samples in each LAT patch simultaneously. By comparing the upper limit on the cross section in this "simultaneous" method to the one with our assumption, we found that the constraints differ at most a factor of 2. Moreover, when we considered the data independently, the constraints became more conservative due to the relaxation of the total flux conservation condition. This means that, even if we ignored the correlation among the data, particularly to reduce the computational cost, we do not need to worry about the artificially strong constraint.

Further, we found the scaling relation between the upper limit on the cross-section and the number of objects N in the composite likelihood analysis. Under an assumption of no observed photon, we found analytically that the upper limit was proportional to $1/N$. In addition, using the HSC-LSBGs, we computed the scaling for DM masses of 10 GeV, 100 GeV and 1 TeV, and showed that for all DM masses, the upper limit scaled with $1/N$ for $N \gtrsim 30$. This is a significant consequence of the Poisson statistics, and is different from the Gaussian statistics in which the scaling obeys $1/\sqrt{N}$.

2) *Final result with DES-LSBG catalog*
Similar to the dN/dz measurement of the HSC LSBGs, we measured the angular cross-correlation of the DES LSBGs with the 6dFGRS sample as the reference sample. Note that for the dN/dz measurement, we used only LSBG samples in the DES Y1 footprint ($\sim$ 7000 objects with a sky coverage of $\sim$ 1800 deg^2) due to the limited region of the random sample in public used in the angular cross-correlation measurement.

In the composite likelihood analysis of the UGRB with all LSBG flux models for the DM annihilation, we obtained the upper limit with 95% C.L. on the cross section for $b\bar{b}$ as 3×10^{-25} cm^3/s at DM mass of 100 GeV. To be conservative in our analysis, we excluded LSBG samples that exist within one degree from point-like sources ($\sim$ 30% of the total sample), because UGRB fluxes around the sources can be under-estimated by mismodeling of source emissions. As a result, the upper limit with the limited sample was $\sim$ 30% weaker than the one with the full sample in all DM mass ranges, i.e., the constraint scales with the inverse of the number of objects. This scaling relation is the same as what we found in the analysis with the HSC LSBGs, which indicates that there is no artificial effect resulting from mismodeling of the UGRB field around the masked sample positions.

Further, as mentioned in a relevant work for the UGRB-flux estimation at a faint source position Ackermann et al. [2015b], the putative flux can be largely affected by variability of model parameters of bright sources in addition to resolved sources around LSBGs. Accordingly, we performed a recalibration of these parameters to consider the variability. We compared DM cross-section constraints using UGRB fields with and without the recalibration process and found that the analysis without the recalibration provided more stringent constraints in all DM mass ranges than those with the UGRB with the recalibration. In particular, at DM mass of 10 GeV, the former gave a $\sim$2 times stronger constraint than the latter. This result indicates that it is imperative to perform the recalibration process for flux-model parameters of bright sources in ROI as well as resolved sources around faint objects when constraining the DM cross-section via likelihood analysis with the faint objects.

Future prospects

Although our constraint on the DM cross-section with all DES LSBGs is one order of magnitude weaker than the canonical cross-section ($\sim 2 \times 10^{-26}$ cm^3/s) at DM mass of 100 GeV. It is at least one order of magnitude weaker than that using the MW dSphs, in the future, we expect to obtain a significant improvement with a joint analysis of large amounts of LSBGs and next-generation telescopes with unprecedented sensitivity and angular resolution.

In an upcoming optical imaging survey with LSST, numerous LSBGs will be discovered with a larger number density than those in the HSC- and DES-LSBG catalogs, because LSST has a sky coverage of $\sim$18,000 deg^2 and reaches the depth of $\sim$27.5 mag/arcsec^2 in r band that is deeper than that in the HSC or DES observation. Accordingly, LSST can discover $\mathcal{O}(10^5)$ LSBGs, which indicates that a constraint with LSST LSBGs can be stringent by an order of magnitude than that using DES LSBGs, considering the simple scaling relation between the upper limit on the cross section and the number of the objects, $\langle \sigma v \rangle \propto 1/N$. We also expect to decrease the uncertainties in the upper limit, which comes from the dN/dz measurement uncertainty and halo properties.

Moreover, LSST will discover fainter and closer LSBGs that are too faint to be detected by the HSC and DES observation. Such faint objects may have small halo and stellar

masses, and they possibly less astronomical γ-ray emitters. Further, because the J-factor of an object is inversely proportional to the square of the distance to those objects, such faint objects' J-factor are expected to be relatively large despite their small halo masses. In order to take this advantage, we need to perform a more precise dN/dz measurement, in particular, at redshifts lower than $z = 0.03$, which corresponds to the lowest redshift-bin bound in our analysis. Of course, for the dN/dz measurement with a very large sky coverage, we need a proper spec-z sample or high-precision photo-z sample in the local universe. However, future constraints with MW dSphs are not expected to be dramatically strict, because the number of dSphs will be at most a few times larger with next-generation telescopes.

As next-generation γ-ray telescopes, the All-sky Medium Energy Gamma-ray Observatory (AMEGO), e-ASTROGAM, GAMMA-400, High Energy cosmic-Radiation Detection (HERD), AMS-100 and Cherenkov Telescope Array (CTA) are underway. GAMMA-400 is a space-based γ-ray telescope with energy ranges of $\sim$ 20 MeV-1 TeV, which fully overlaps with the LAT energy range. The angular and energy resolution are planned to be 0.01° and $\sim$2% at 100 GeV, respectively (for LAT, those values are 0.1° and 10%, respectively). AMEGO and e-ASTROGAM are space-based telescopes and planned for the cosmic γ-ray search in MeV energy (from $\sim$0.1 MeV to several GeV, with an angular resolution of $< 2°$ at 100 MeV), which is one of the most underexplored windows in the universe. HERD and AMS-100 will cover the energy range from $\sim$1 GeV to 10 TeV; meanwhile, and for CTA, the range is from $\sim$50 GeV to $\sim$300 TeV. The observations of the cosmic γ ray in the wide energy ranges with these detectors allow us to perform more robust and detailed DM-signal probes.

In addition to surveys by the above mentioned γ-ray telescopes, there is the paramount up-coming radio survey, the Square Kilometre Array (SKA). As described in Chapter 3, because most LSBGs are HI rich, radio surveys with a frequency of $\sim$ 1.4 GHz are one of the best techniques to discover them in the local universe. In the survey, numerous gas-rich LSBGs will be detected with precise redshifts in the local universe. According to Conselice et al. [2016], the galaxy number density in $z \lesssim 0.1$ is ~ 0.1 Mpc^{-3}. Then, we expect that $\sim 50,000$ LSBGs will be discovered in ≤ 120 Mpc that corresponds to the redshfit of the first redshift-bin edge in our dN/dz measurement (to be conservative, we assume the sky fraction to 0.25 and the LSBG fraction in the galaxy population in the local universe to 30% [Trachternach et al., 2006]). Similarly, it will be expected that

$\sim$ 500 LSBGs will be discovered in $z \leq 25$ Mpc that is the minimum distance assigned to individual LSBGs in our analysis. If the redshift distribution of these 500 objects is uniform, the DM cross-section constraint will be lower than the canonical cross-section below DM mass of several hundred GeV. Or depending on the redshift distribution of them, DM masses below a few TeV are possibly ruled out, which would be not able to reached in the DM probe using MW dSphs.

Further, as also described in Chapter 3, by applying the same method to the study of LSBG properties using the ALFALFA HI survey data with SDSS photometric data, we will measure various astrophysical properties of LSBGs. It will enables us to know more precise masses and density profiles of those DM halos, and the capability of LSBG for the DM-signal probe would be more apparent.

Appendix A

UGRB construction

In this appendix, we describe detailed procedures to construct the UGRB field used in the composite likelihood analysis. Particularly, we 1) optimize the model parameters of all bright sources, including the galactic diffuse, isotropic diffuse, and cataloged sources, 2) find new point sources exceeding the detection threshold in our ROIs, and 3) perform optimization again using the up-dated bright-source list and further detailed fitting model paratemeters of bright sources around LSBG positions. In these steps, our procedures are performed using `fermipy`.

1) *Optimization of bright source parameters*
Before performing the composite likelihood analysis, we construct the UGRB field from the observed photon data. As described in Section 5.3.2, we derive the galactic and isotropic diffuse emission model from the corresponding templates provided from the Fermi Collaboration, in addition to the bright-source emission model from the 4FGL or 4FGL-DR2 source catalog, which contains point-like and extended sources with TS larger than 25. According to the Fermi Collaboration, this detection threshold corresponds to 4-σ level. As the first step of UGRB construction, we perform the maximum likelihood analysis in each ROI to fit spectral parameters for all flux models to the photon data. `fermipy` optimizes the parameters in order of greater intensity sources down to fainter ones for convergence in our maximum likelihood procedure.

Then, we obtain the UGRB field by subtraction of all emission model fluxes from the observed photon flux. In the analysis with HSC LSBGs, we use the current UGRB field,

whereas, for the analysis with DES LSBGs, we further perform point-like source selection and detection processes in steps 2) and 3). We show two samples of the observed photon flux in two different ROIs in Figure A.1 and show the model and UGRB-flux maps in Figure A.2.

2) *Detection of new sources*
First, the 4FGL-DR2 catalog, used in the analysis with DES LSBGs, contains point sources with TS above the detection threshold in the 4FGL catalog but below in the 4FGL-DR2 catalog. We remove those sources in our analysis. Next, we find new point sources in ROIs. The photon statistics in our analysis is larger than those in the 4FGL-DR2 catalog because the observation-time interval in our data is ∼20% longer than that in the 4FGL-DR2 catalog. Therefore, there should be new point sources with TS values above the detection threshold in our ROIs. To detect the source candidates, we implement the source finding method in *fermipy*, applying a flux model of a point-like test source with a power-law spectrum, which has a single free parameter for an amplitude α of the flux model. We set source selection filters of `sqrt_ts_threshold`=5.0 and `min_separation`=1.0. To quantify the significance of excess of the candidate fluxes in the UGRB flux we constructed in the first maximum likelihood run above, we define a TS value as follows:

$$\begin{aligned} TS \equiv\ & 2\Delta \log \mathcal{L}_{\max}, \\ & \text{where } \Delta \log \mathcal{L} \equiv \log \mathcal{L}(\mathcal{D}, \theta|\alpha) - \log \mathcal{L}(\mathcal{D}, \theta|\alpha = 0). \end{aligned} \tag{A.1}$$

$\mathcal{D}$ is the observed photon count. θ is the best-fit model parameters of the diffuse emission models as well as resolved sources in the 4FGL-DR2 catalog with $TS \geq 25$. $\Delta \log \mathcal{L}_{\max}$ denotes the maximum delta-likelihood when varying the candidate's flux amplitude α. As a result, we find 79 new point sources in ROIs ($\sim$ 7% of all resolved sources), excluding duplicates in overlapping areas with neighboring ROIs. After identifying positions of new sources with $TS \geq 25$, *fermipy* fits their spectral amplitudes and indexes to the residual photon flux that is produced in the previous step.

3) *Recalibration of parameters of bright sources around LSBGs*
As a relevant work with respect to the UGRB-flux estimation at a faint source position [Ackermann et al., 2015b] have highlighted, the flux estimation can be significantly affected by fluctuations of model parameters for neighboring bright sources. Therefore,

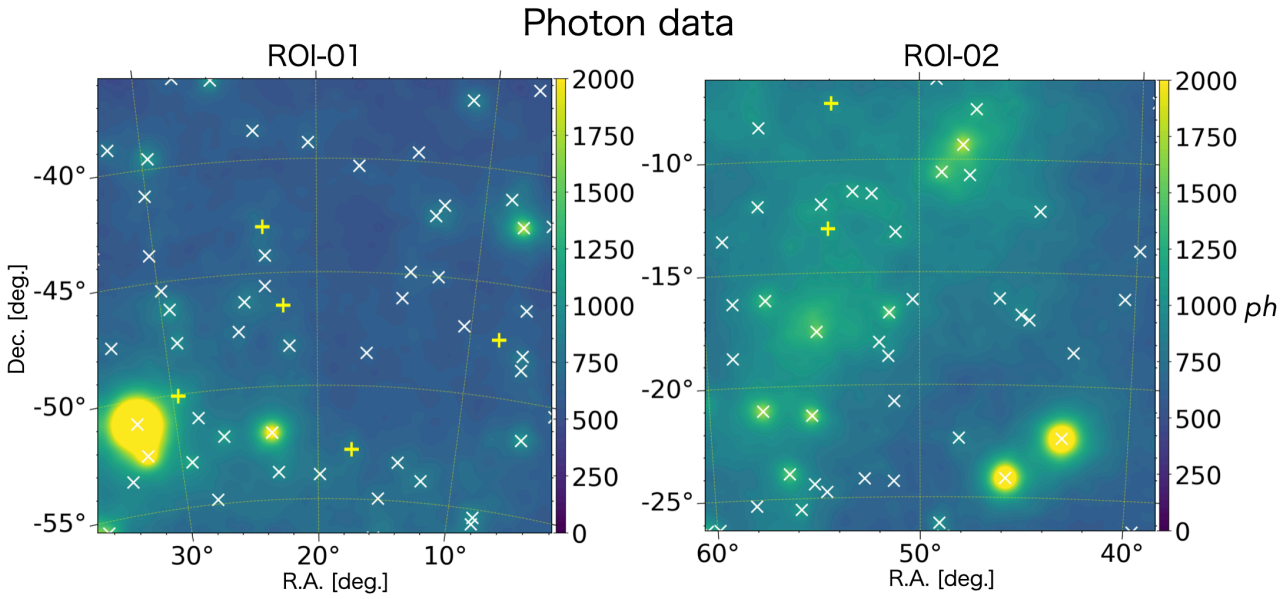

FIGURE A.1: Photon-data maps for two different ROIs. The cross and plus markers represent the location of cataloged sources and new ones we detected in step 2), respectively. The color bars represent the photon count.

we revisit UGRB construction around LSBG positions to allow for the variability of these model parameters and perform a recalibration of these parameters as follows. First, for sources with $TS > 1000$, we vary both shape and amplitude parameters of them. Also, for all resolved sources within 3° from the LSBG position, we vary both parameters for $400 < TS \leq 1000$ and only the amplitude parameter for $25 \leq TS \leq 400$. Then, all the freeing parameters are fit to the observed photon data by `fit` function of `Fermipy`. Note that the other parameters except for the freeing ones are fixed to the values in the previous step. The sample of the recalibrated UGRB and corresponding TS map are shown in Figure A.3. All left or right panels in these plots show the same ROI of each ("ROI-01" and "ROI-02").

Name	(l [deg], b [deg])	TS	Prefactor	Index
PS J2058.8-4105	(0.70, -40.83)	77.3	4.29e-13	-2.87
PS J2049.0-4020	(1.52, -38.92)	37.4	1.50e-13	-2.06
PS J2152.9-3930	(2.69, -51.15)	41.0	1.76e-13	-2.14
PS J2038.7-3655	(5.51, -36.52)	36.7	4.44e-14	-1.55
PS J0402.7-2743	(12.68, -27.72)	35.5	1.91e-13	-2.61
PS J2108.6-0408	(46.05, -32.22)	28.0	9.78e-14	-1.91
PS J2348.6-2100	(52.70, -74.42)	30.0	1.57e-13	-2.34
PS J2211.0-0029	(60.84, -43.21)	37.2	1.37e-13	-1.98
PS J2202.3+0208	(61.79, -39.87)	33.9	2.39e-13	-2.51
PS J2311.8-0504	(71.39, -57.61)	484.5	9.30e-13	-4.19
PS J2241.5+0454	(73.59, -45.16)	44.1	6.37e-14	-1.69
PS J2350.2-0558	(85.67, -64.33)	32.0	7.84e-14	-1.85
PS J2349.8-0122	(90.55, -60.31)	32.7	1.97e-13	-2.34
PS J0003.3-0702	(91.12, -66.90)	34.6	5.37e-14	-1.72
PS J0001.3-0008	(96.83, -60.45)	39.5	1.36e-13	-2.02
PS J0003.3+0716	(102.51, -53.68)	35.4	2.15e-13	-2.42
PS J0147.6-0826	(161.01, -67.06)	115.1	3.65e-13	-2.40
PS J0152.9-1108	(168.02, -68.45)	30.1	7.55e-14	-1.97
PS J0139.2-1705	(173.17, -75.08)	32.0	1.08e-13	-2.11
PS J0335.7-0728	(193.87, -46.42)	40.6	1.65e-13	-2.16
PS J0336.6-1302	(201.26, -48.95)	55.9	3.33e-13	-3.03
PS J0203.6-2442	(208.49, -73.61)	27.3	7.93e-14	-2.00
PS J0504.3-0956	(209.77, -28.27)	28.5	9.67e-14	-1.95
PS J0427.4-1832	(215.08, -39.86)	30.0	3.51e-14	-1.62
PS J0446.3-1729	(215.86, -35.28)	29.0	6.36e-14	-1.75
PS J0624.6-0736	(216.72, -9.39)	36.3	3.74e-13	-2.35
PS J0508.8-2327	(224.76, -32.33)	33.7	1.31e-13	-2.21
PS J0541.3-2059	(225.01, -24.43)	29.0	1.34e-13	-2.24
PS J0402.4-2743	(225.22, -47.89)	36.7	1.95e-13	-2.54
PS J0653.9-1329	(225.25, -5.56)	39.8	1.17e-13	-1.77
PS J0524.5-2614	(229.14, -29.80)	33.5	1.24e-13	-2.11
PS J0554.5-2756	(233.31, -24.00)	42.1	3.10e-14	-1.50
PS J0627.5-2600	(234.18, -16.44)	44.6	1.17e-13	-1.92
PS J0156.7-3235	(237.98, -74.85)	27.2	3.84e-14	-1.73
PS J0352.1-3704	(239.26, -50.84)	31.1	3.96e-14	-1.68
PS J0412.6-3927	(242.78, -46.78)	39.5	5.33e-14	-1.74
PS J0515.4-3840	(242.90, -34.57)	36.4	9.94e-14	-1.99
PS J0514.1-4004	(244.55, -35.04)	49.8	2.27e-13	-2.49

TABLE A.1: List of parameters for point sources we detected in our ROI. "Prefactor" and "Index" means spectral parameters of α and γ for $dN/dE = \alpha(E/1[\mathrm{GeV}])^{\gamma}$, respectively. The units of α are $\mathrm{cm}^{-2}\mathrm{s}^{-1}\mathrm{MeV}^{-1}$.

Name	(l [deg], b [deg])	TS	Prefactor	Index
PS J0459.6-4530	(251.00, -38.15)	93.7	2.96e-13	-2.45
PS J0528.1-4648	(253.00, -33.30)	53.9	2.34e-13	-2.49
PS J0243.2-4218	(253.92, -62.67)	38.5	1.07e-13	-2.12
PS J0500.2-5321	(260.98, -37.85)	37.0	1.64e-13	-2.54
PS J0641.2-5203	(261.24, -22.58)	40.1	1.63e-13	-2.33
PS J0259.1-4746	(261.25, -57.70)	34.0	1.02e-13	-2.11
PS J0535.0-5441	(262.45, -32.71)	55.1	2.11e-13	-2.20
PS J0323.0-5035	(262.59, -52.95)	37.1	1.72e-13	-2.56
PS J0412.6-5434	(264.21, -44.52)	39.1	9.05e-14	-2.01
PS J0338.9-5321	(265.01, -49.59)	36.4	6.44e-14	-1.85
PS J0358.9-5432	(265.05, -46.41)	49.3	2.16e-13	-2.79
PS J0524.1-5700	(265.23, -34.24)	39.4	1.86e-13	-2.62
PS J0443.4-5951	(269.63, -39.14)	33.6	1.01e-13	-2.02
PS J0637.5-6220	(272.08, -25.39)	28.4	9.54e-14	-2.06
PS J0535.9-6603	(275.93, -32.24)	51.2	1.01e-13	-1.73
PS J0612.9-6637	(276.50, -28.53)	38.5	1.34e-13	-2.12
PS J0531.4-6705	(277.20, -32.58)	58.2	3.35e-13	-2.28
PS J0133.1-4257	(277.49, -72.06)	43.2	2.14e-13	-2.82
PS J0158.3-5004	(278.25, -63.73)	202.2	4.30e-13	-2.34
PS J0543.3-6909	(279.47, -31.26)	50.5	3.22e-13	-2.13
PS J0739.2-6739	(279.52, -20.59)	71.3	2.75e-13	-2.14
PS J0459.0-7006	(281.48, -34.85)	39.4	1.79e-13	-2.05
PS J0358.3-6946	(283.83, -39.70)	60.0	2.56e-13	-2.40
PS J0128.6-4626	(284.53, -69.33)	36.3	1.48e-13	-2.43
PS J0147.4-6027	(290.82, -55.34)	39.0	6.68e-14	-1.88
PS J0154.5-6604	(293.10, -49.83)	734.7	8.80e-13	-2.36
PS J0110.2-5248	(296.41, -64.08)	55.2	2.29e-13	-2.67
PS J0126.1-6747	(297.95, -49.01)	39.5	3.93e-14	-1.67
PS J0032.3-4728	(312.08, -69.31)	41.4	4.88e-14	-1.70
PS J0006.1-5627	(315.29, -59.57)	33.4	1.47e-13	-2.49
PS J2217.3-6728	(322.12, -43.46)	36.2	1.08e-13	-2.05
PS J2152.6-6442	(327.20, -43.04)	36.2	7.49e-14	-1.92
PS J2127.6-5743	(337.63, -43.23)	33.0	1.36e-13	-2.10
PS J2129.9-5631	(339.06, -43.91)	45.7	1.64e-13	-2.13
PS J2042.9-5756	(339.13, -37.39)	38.3	5.83e-14	-1.71
PS J2118.2-5420	(342.55, -42.89)	55.7	1.16e-13	-1.88
PS J2210.5-5027	(344.43, -51.65)	35.8	1.64e-13	-2.31
PS J2331.3-3840	(353.27, -69.68)	40.8	4.43e-14	-1.62
PS J2145.7-4505	(354.31, -49.11)	34.0	1.26e-13	-1.98
PS J2020.4-4534	(354.46, -34.16)	31.0	1.05e-13	-1.85
PS J2135.9-4445	(355.21, -47.45)	27.5	1.37e-13	-2.07

TABLE A.2: Continued from Table A.1.

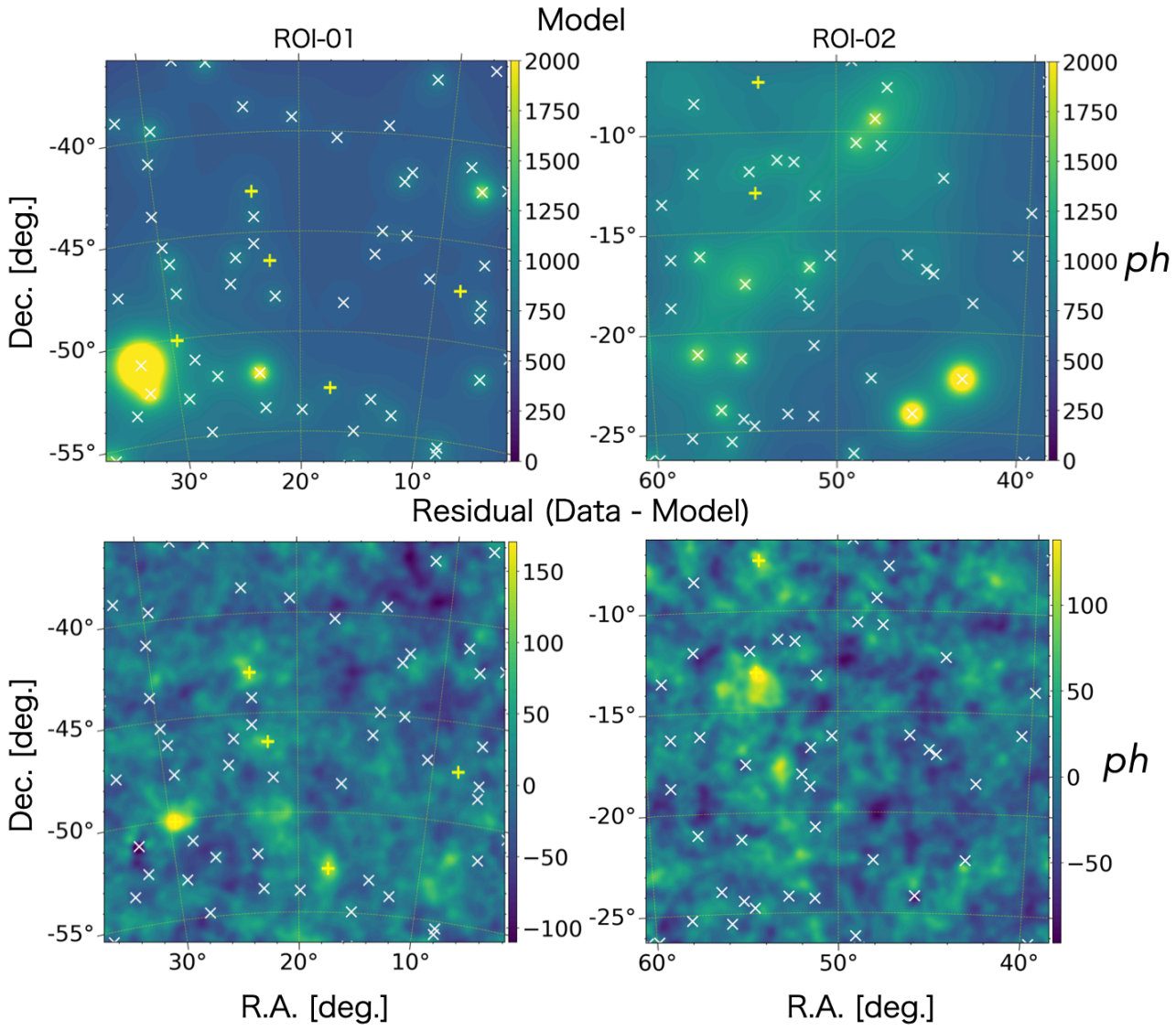

FIGURE A.2: (*Top*) The model maps and (*Bottom*) UGRB fields constructed in step 1). The markers are the same in Figure A.1.

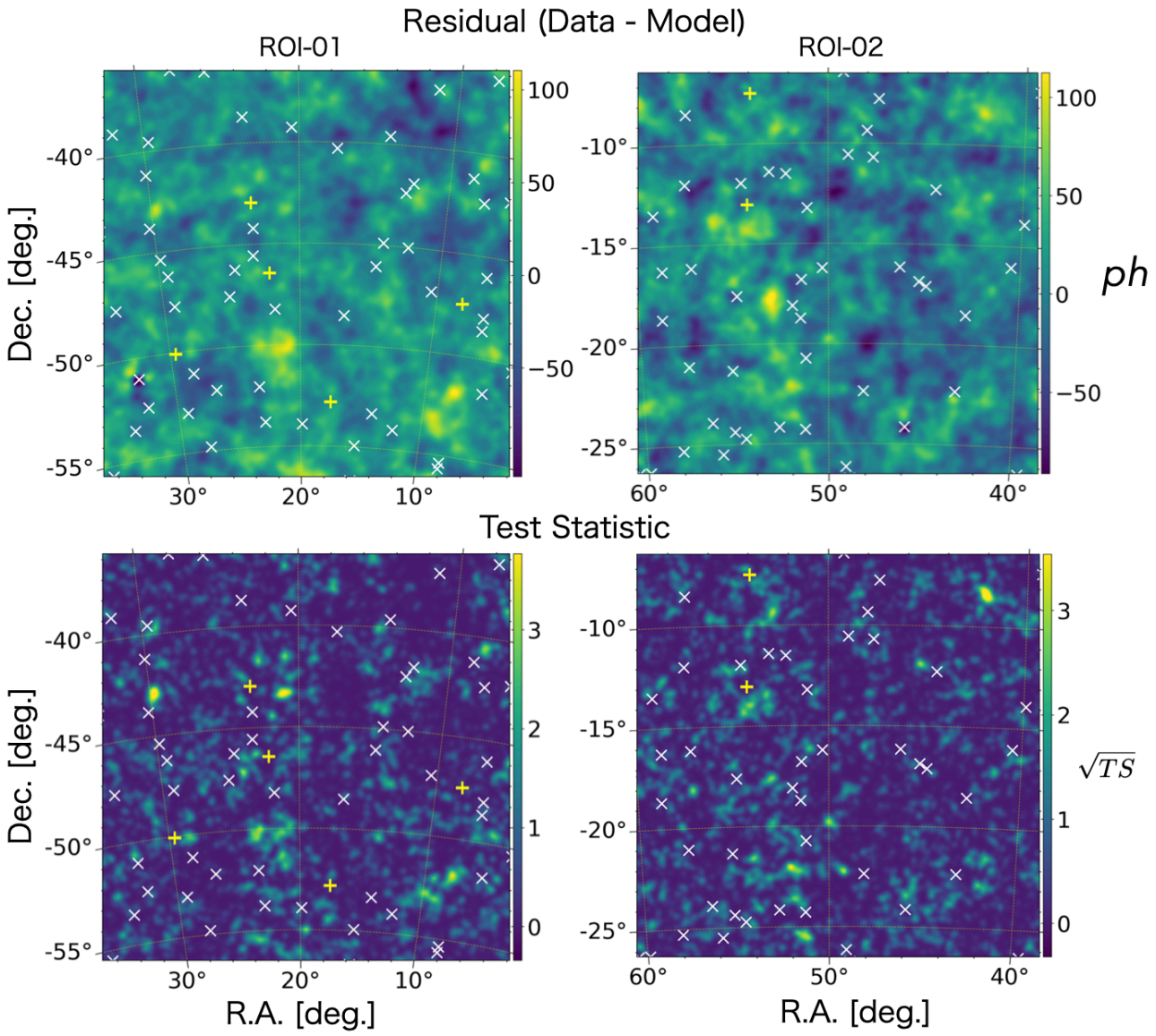

FIGURE A.3: (*Top*) The reconstructed UGRB fields in step 3) and (*Bottom*) TS maps. These ROIs do not contain any bright source with $TS \geq 25$. The markers are the same in Figure A.1.

Appendix B

LSBG putative flux & covariance

In this appendix, we describe our detailed procedures to obtain likelihood profiles of UGRB fluxes at the LSBG positions as a function of the amplitude parameter, which are called "LSBG putative fluxes". The flux profiles are employed as a prior distribution for the Bayesian method in our likelihood analysis in Chapters 6 and 7, to constrain the amplitude parameter of γ-ray fluxes that originated from the DM annihilation within LSBG DM halos, i.e., to provide upper limits on the DM cross-section. We note that for the likelihood measurement, we consider the recalibrated UGRB field which is discussed in Chapter A. For an impact of the recalibration to constraint on the DM cross-section, see Section 7.6. In addition, we discuss a covariance between model parameters of the putative flux of neighboring LSBGs.

LSBG putative flux
As described in Section 7.3, in the case of a likelihood analysis for point-like faint sources, particularly for sources with TS values of less than 1 in most energy bins, the Fermi Collaboration has recommended the Bayesian method Nolan et al. [2012]. Therefore, we discuss whether it is valid to apply the Bayesian method to our likelihood procedure with respect to the use of LSBGs. Accordingly, we compute the TS values of our LSBGs.

To estimate the likelihood profile for the LSBG putative flux in addition to the TS value, we apply a simple power-law model with an index of -2 and amplitude parameter α at the LSBG position, as a point-like test source. We assign the point source in the UGRB field to fit the amplitude parameter to the UGRB flux. Then, the delta-likelihood is given as

follows:

$$TS \equiv -2\Delta \log \mathcal{L}_{\max},$$
$$\text{where } \Delta \log \mathcal{L} \equiv \log \left(\frac{\mathcal{L}(\mathcal{D}, \theta|\alpha = 0)}{\mathcal{L}(\mathcal{D}, \theta|\alpha)} \right). \tag{B.1}$$

$\mathcal{D}$ is the photon count data by the *Fermi*-LAT observation. θ is the model parameter set of the galactic and isotropic diffuse emissions as well as point sources in the 4FGL-DR2 sources with $TS \geq 25$, which are optimized in the maximum likelihood run in Appendix A. $\Delta \log \mathcal{L}_{\max}$ represents the maximum delta-likelihood when varying the amplitude of the test model α. We show some samples of profiles of the LSBG putative flux in Figure B.1.

In Figure B.2, we show TS values of all DES-LSBG putative fluxes in each energy bin. We find that fractions of LSBGs with $TS < 1$ for energy ranges of $E < 1$ GeV, $1 < E < 10$ GeV and $E > 10$ GeV are 89.0%, 90.8% and 97.4%, respectively, and conclude that it is valid for our likelihood analysis to apply the Bayesian method introducing the putative flux profile as a prior distribution. In addition, we found similar TS values for the HSC-LSBGs. For comparison, in Figure B.3, we show a scatter plot for TS values of all DES LSBGs computed from two different UGRB fields. One is constructed by procedures in step 1) in Appendix A, which is called the "baseline" UGRB, whereas another is constructed by all procedures from step 1) to 3) in Appendix A.

Covariance between neighboring LSBGs

To compute the covariance between neighboring LSBGs, we perform the maximum likelihood run for two amplitude parameters of an object pair to the UGRB flux, similar to the method used in Section 7.4.1. We show a sample of the measured cross-covariance of the pair in Figure B.4. Note that all values of the cross-covariance are negative except for one pair. These negative values are due to the total photon flux conservation in the likelihood run. Similar behavior has been reported in Adam et al. [2021]. They have seached the UGRB sky around the coma cluster and found that the negative covarinaces between amplitude parameters of γ-ray sources within the ROI have been measured in most cases in Figure B.5. Meanwhile, in the case of spectral shape parameters, the covariance is likely to be positive. This is also the same result from the photon count conservation and the case of the amplitude parameter because the model flux decreases as the spectral index increases.

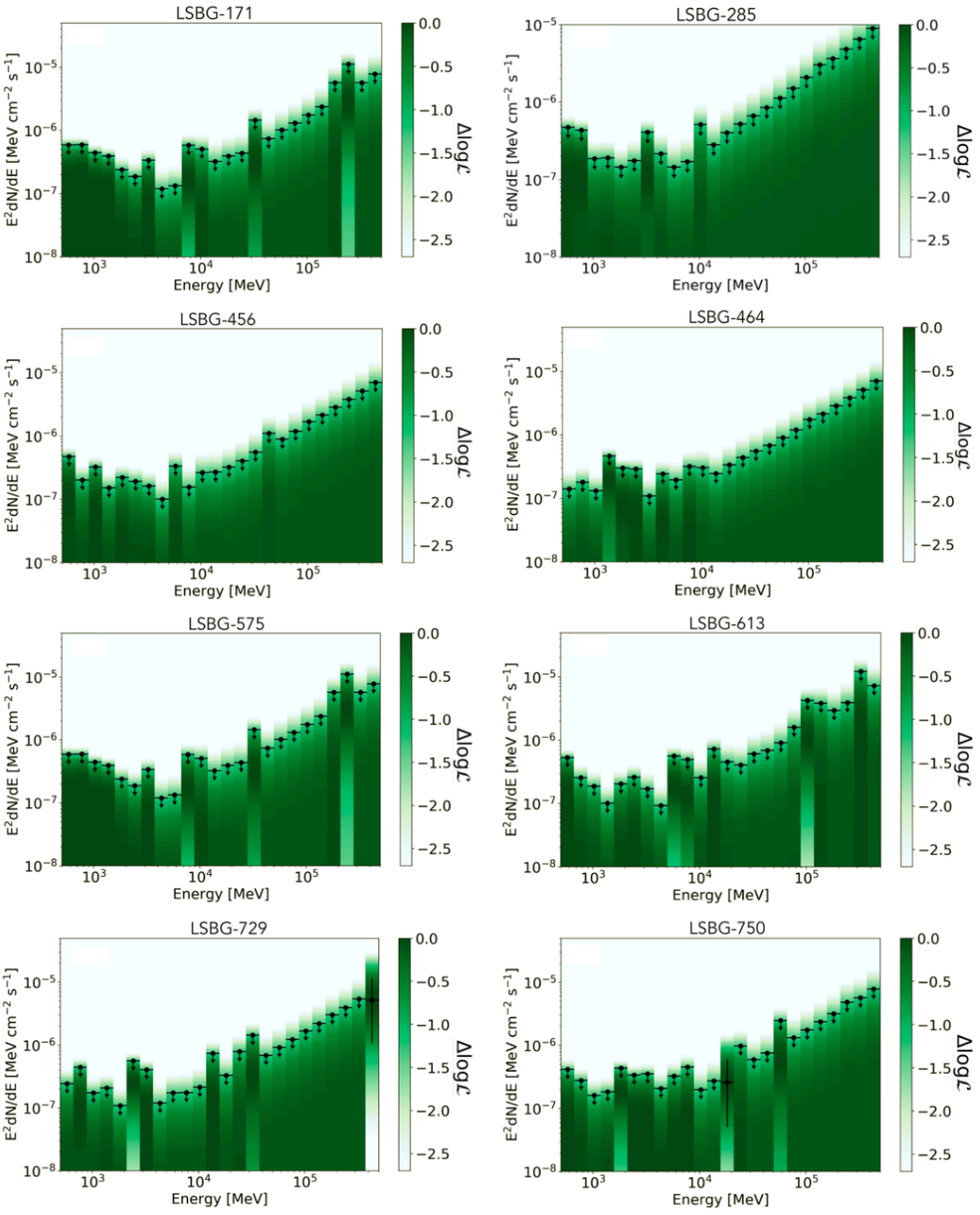

FIGURE B.1: Sample of LSBG putative fluxes; putative fluxes of the eight HSC-LSBGs with known redshifts are shown. The color bar plots represent the delta-likelihood as a function of flux amplitude, which is defined by Equation B.1. The down arrows represent upper limits on flux amplitudes with 95% C.L.. The bar plots denote a 1-σ level centered on the amplitude providing the maximum likelihood.

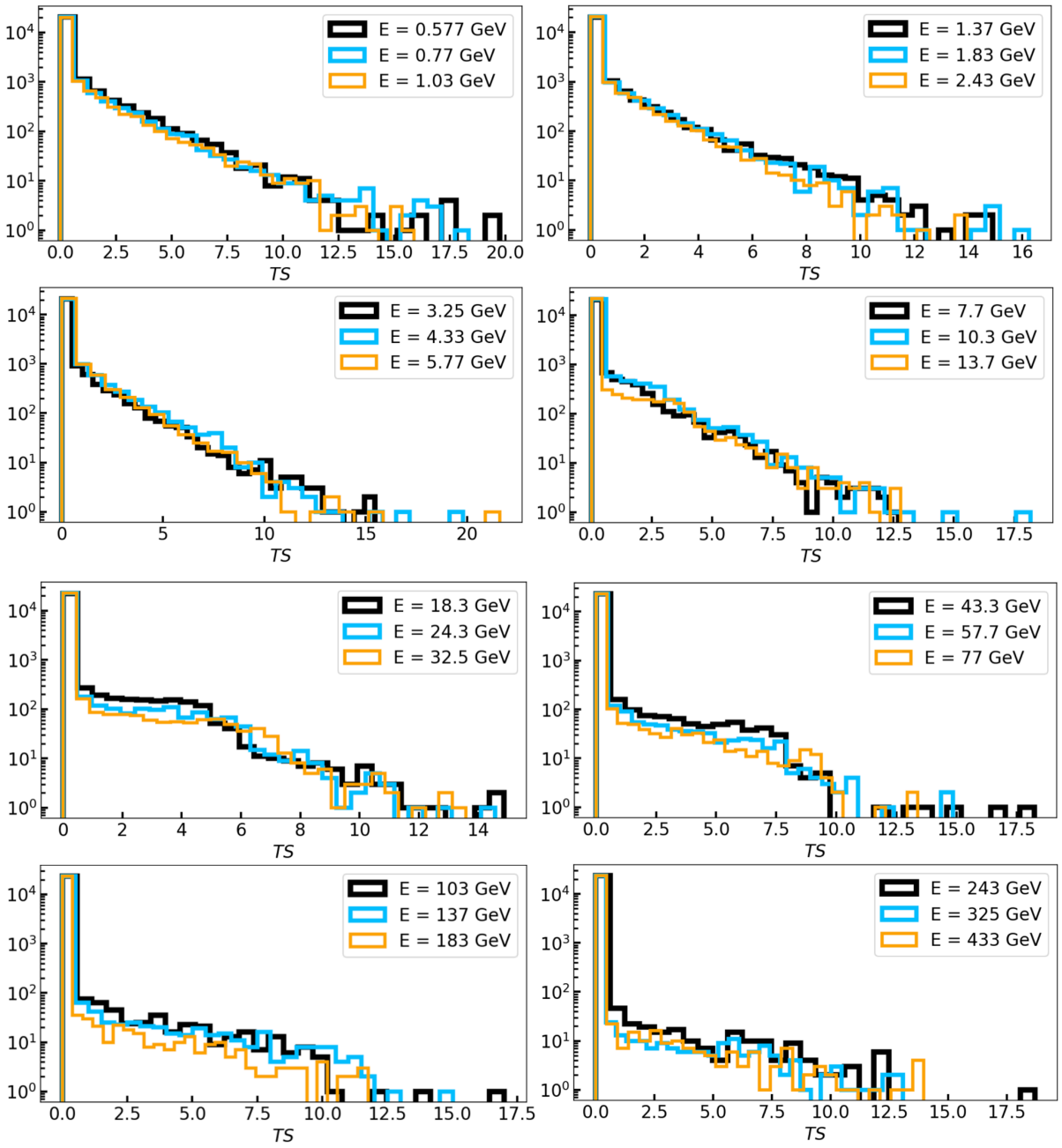

FIGURE B.2: Histogram for the TS values of DES-LSBG putative fluxes in each energy bin.

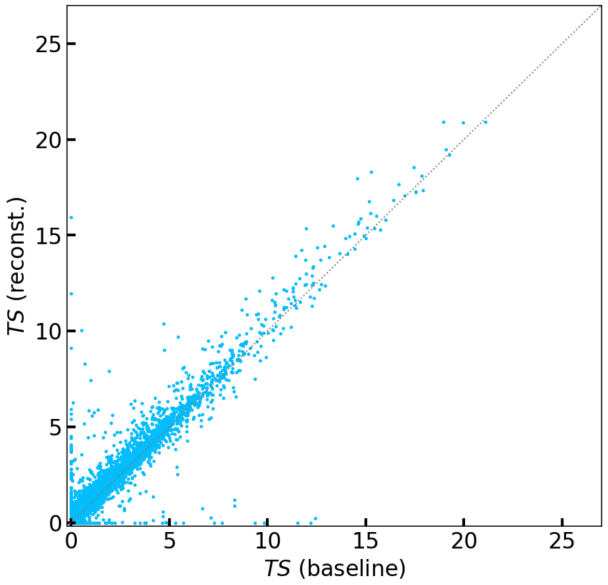

FIGURE B.3: TS values with the recalibrated and baseline UGRB.

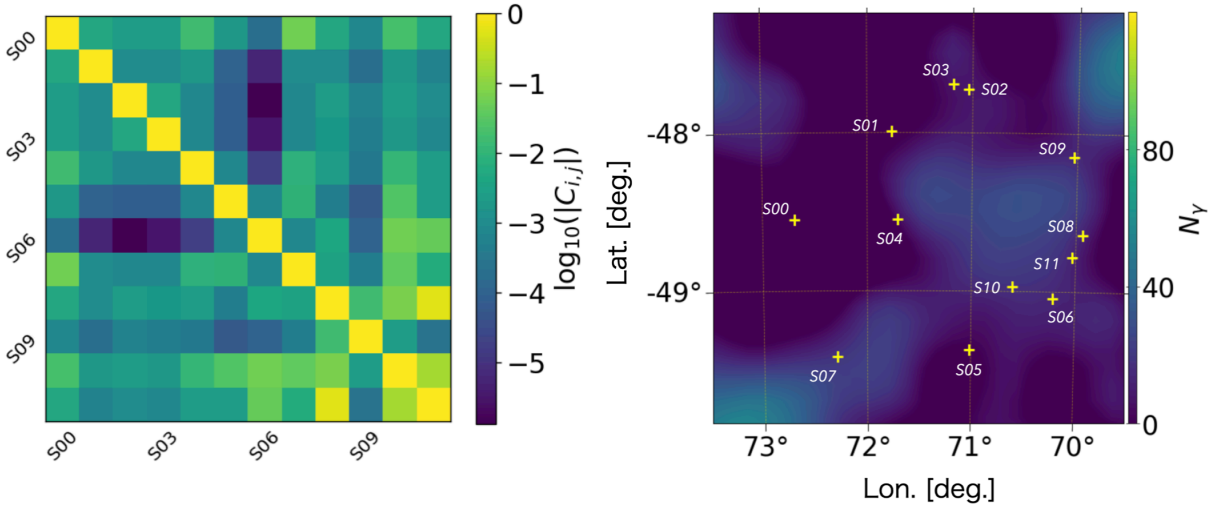

FIGURE B.4: (*Left*): Sample of the covariance matrix for amplitude parameters of putative fluxes at 12 LSBG positions in the UGRB field. This sample patch locates in the HSC S16A footprint. Note that the color bars represent the absolute values of the matrix elements in logarithmic and all of the values are negative except for the covariance between S06 and S09. (*Right*): The UGRB photon count map with the LSBG positions with plus signs. The color bars show photon counts.

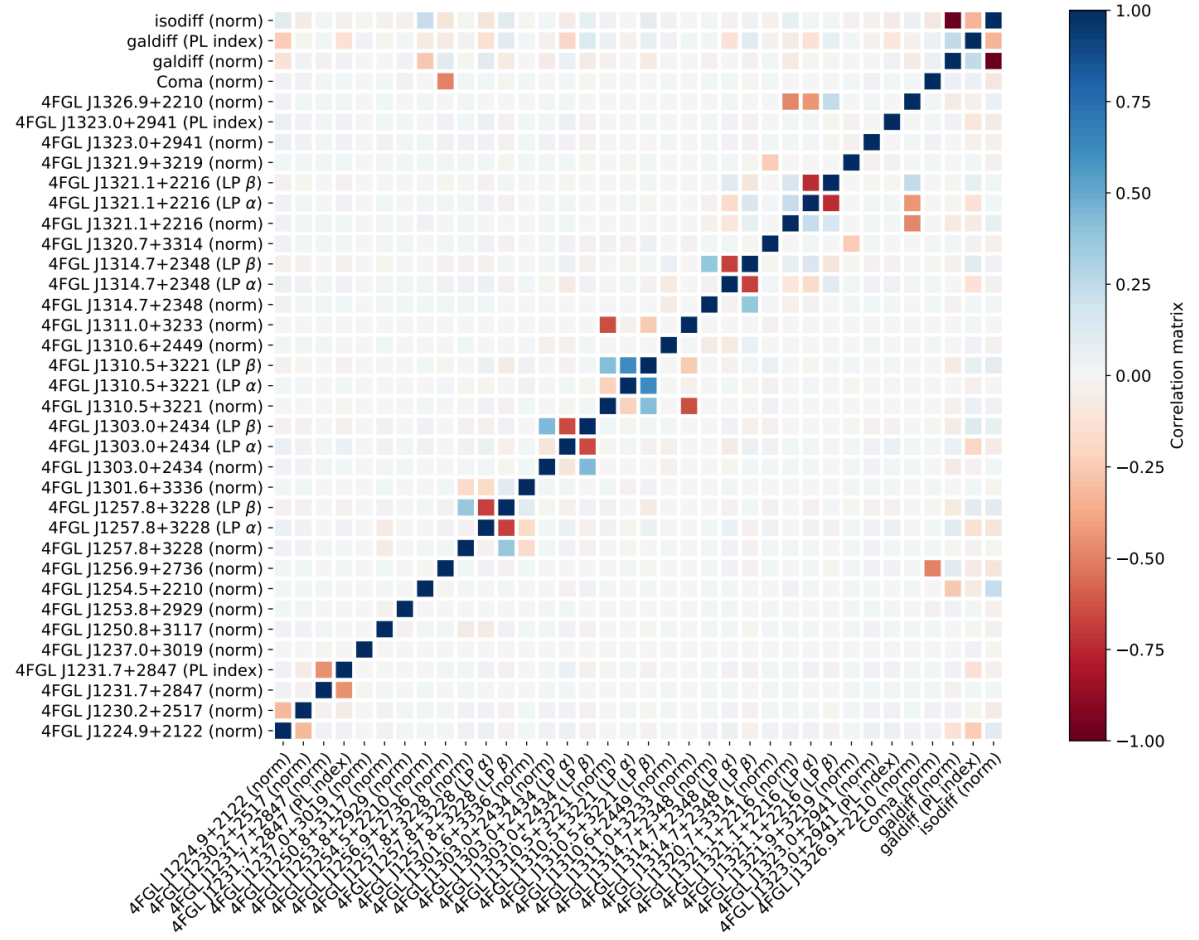

FIGURE B.5: The covariance matrix of the spectral parameters for γ-ray sources within the ROI, including the amplitude parameter for the Coma cluster in the fourth line. The amplitude parameter of the nearest object, *4FGL J1256.9+2736*, is in the ninth line up to the bottom and has a negative covarinance between the amplitude parameters of this 4FGL source and the Coma cluster. *(norm)* with a source name means an amplitude parameter of the source, and *(PL index)*, *(LP α)* and *(LP β)* mean the source's shape parameters for a single power-law and log-parabola (the latter two) spectra, respectively. This figure is obtained from Adam et al. [2021].

Appendix C

Supplemental plots for dN/dz measurement

We display the angular cross-correlation of the HSC- and DES-LSBG catalogs in Figure C.2. In addition, we show the full covariance matrix in the case of using the DES-LSBG sample in Figure C.3 and show the matrix $\bar{C}_{ml}$ in Equation 7.6 in Figure C.1.

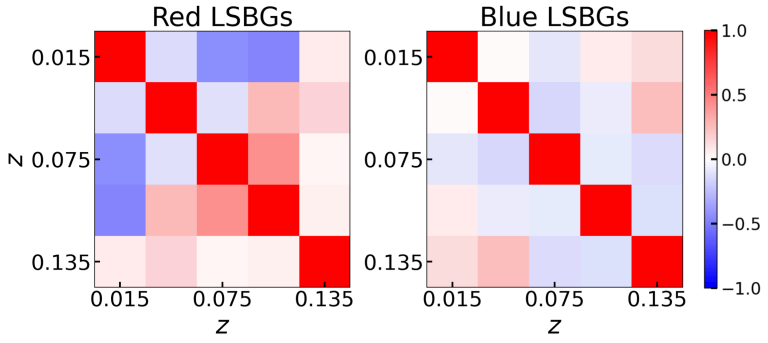

FIGURE C.1: The covariance matrix between different redshift bins in Equation 7.6 for the red LSBGs (*Left*) and the blue LSBGs (*Right*), which are normalized by diagonals.

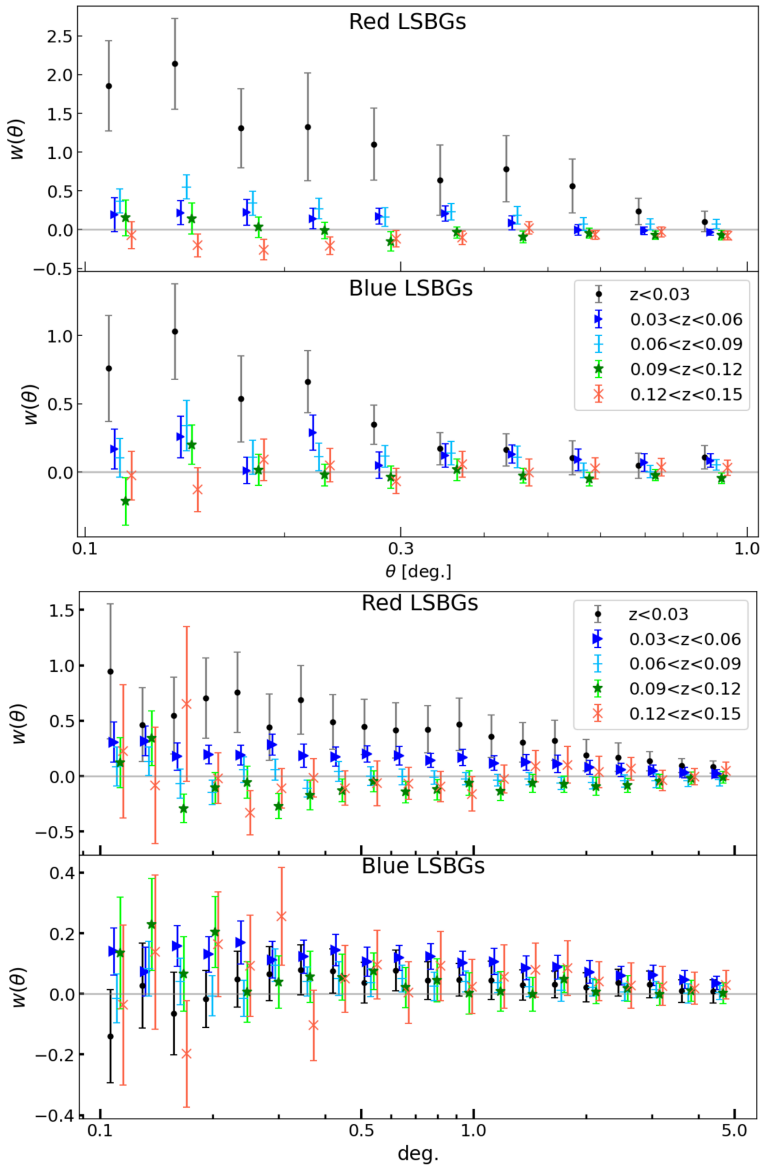

FIGURE C.2: The angular cross-correlations of HSC (*Top*) and DES (*Bottom*) LSBGs with reference samples of each, the NSA (for HSC LSBGs) and 6dFGRS (for DES LSBGs) samples. Each panel displays the angular correlation with red ($g-i \geq 0.64$ for the HSC sample, $g-i \geq 0.60$ for the DES sample) and blue ($g-i < 0.64$ for the HSC sample, $g-i < 0.60$ for the DES sample) objects. Each angular separation for the cross-correlation measurement for the HSC and DES samples is defined by logarithmic binning with 10 and 20 bins in angular range of $0.1^\circ < \theta < 1.0^\circ$ and $0.1^\circ < \theta < 5.0^\circ$, respectively. The error-bar plots with 1-σ jackknife errors with circle, triangle, plus, star and cross markers represent redshift range of $z < 0.03$, $0.03 < z < 0.06$, $0.06 < z < 0.09$, $0.09 < z < 0.12$ and $0.12 < z < 0.15$, respectively.

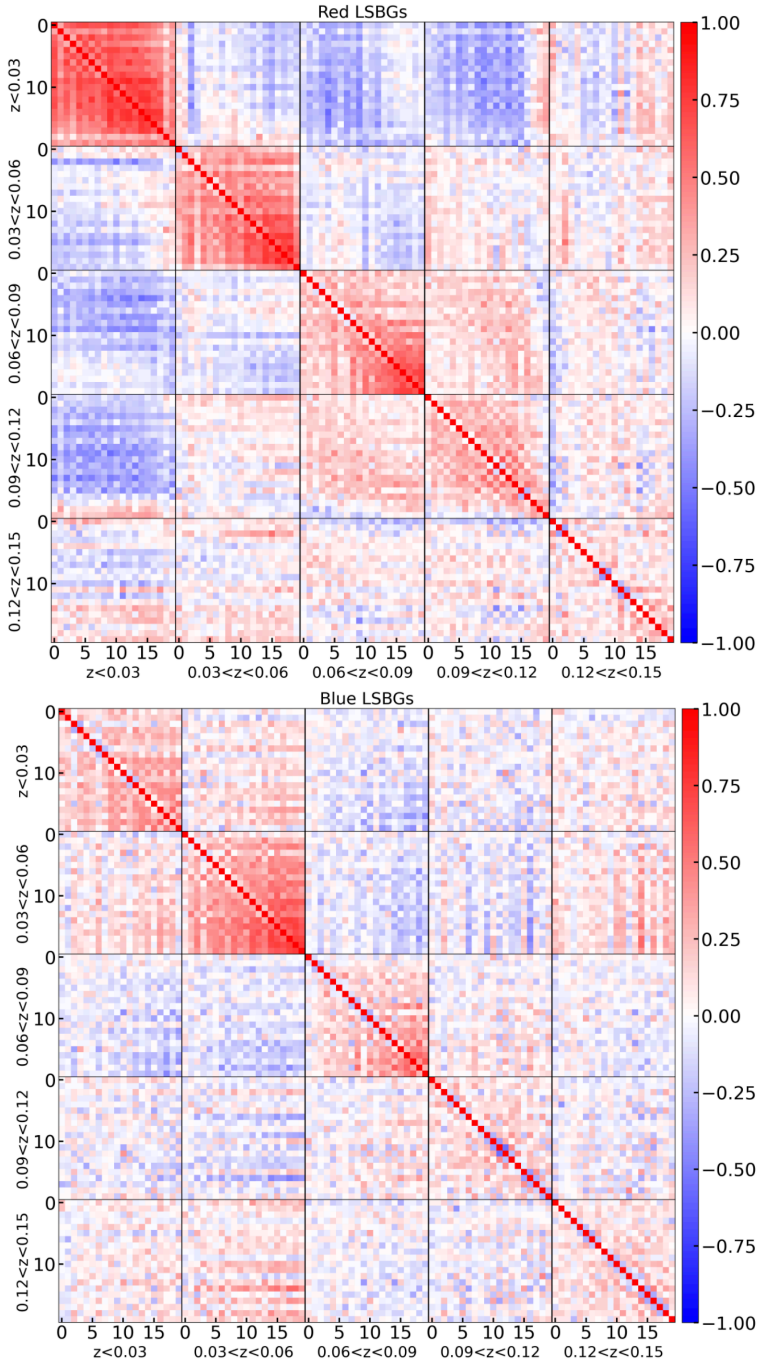

FIGURE C.3: The full covariance matrix between different the redshift and angular bins in Equation 7.5 for the red LSBGs (*Top*) and the blue LSBGs (*Bottom*), which are normalized by diagonals.

Bibliography

Search for dark matter in final states with an energetic jet, or a hadronically decaying W or Z boson using 12.9 fb^{-1} of data at $\sqrt{s} = 13$ TeV. 2016.

Kevork N. Abazajian, Jennifer K. Adelman-McCarthy, Marcel A. Agüeros, Sahar S. Allam, and Carlos Allende Prieto *et al.* The Seventh Data Release of the Sloan Digital Sky Survey. *ApJS*, 182(2):543–558, June 2009. doi: 10.1088/0067-0049/182/2/543.

Kevork N. Abazajian, Shunsaku Horiuchi, Manoj Kaplinghat, Ryan E. Keeley, and Oscar Macias. Strong constraints on thermal relic dark matter from Fermi-LAT observations of the Galactic Center. *Phys. Rev. D*, 102(4):043012, August 2020. doi: 10.1103/PhysRevD.102.043012.

A. A. Abdo, M. Ackermann, M. Ajello, A. Allafort, and E. Antolini *et al.* (Fermi LAT Collaboration). Fermi Large Area Telescope First Source Catalog. *ApJS*, 188(2):405–436, June 2010. doi: 10.1088/0067-0049/188/2/405.

S. Abdollahi, F. Acero, M. Ackermann, M. Ajello, and W. B. Atwood *et al.* (Fermi-LAT Collaboration). Fermi Large Area Telescope Fourth Source Catalog. *ApJS*, 247(1):33, March 2020. doi: 10.3847/1538-4365/ab6bcb.

F. Acero, M. Ackermann, M. Ajello, A. Albert, and W. B. Atwood *et al.* (Fermi-LAT Collaboration). Fermi Large Area Telescope Third Source Catalog. *ApJS*, 218:23, June 2015. doi: 10.1088/0067-0049/218/2/23.

M. Ackermann, A. Albert, B. Anderson, L. Baldini, and J. Ballet *et al.* (Fermi-LAT Collaboration). Dark matter constraints from observations of 25 MilkyÂ Way satellite galaxies with the Fermi Large Area Telescope. *Phys. Rev. D*, 89(4):042001, February 2014. doi: 10.1103/PhysRevD.89.042001.

M. Ackermann, M. Ajello, A. Albert, W. B. Atwood, and L. Baldini *et al.* The Spectrum of Isotropic Diffuse Gamma-Ray Emission between 100 MeV and 820 GeV. *ApJ*, 799: 86, January 2015a. doi: 10.1088/0004-637X/799/1/86.

M. Ackermann, M. Ajello, A. Albert, W. B. Atwood, and L. Baldini *et al.* Search for Extended Gamma-Ray Emission from the Virgo Galaxy Cluster with FERMI-LAT. *ApJ*, 812(2):159, October 2015b. doi: 10.1088/0004-637X/812/2/159.

M. Ackermann, M. Ajello, A. Albert, W. B. Atwood, and L. Baldini *et al.* The Spectrum of Isotropic Diffuse Gamma-Ray Emission between 100 MeV and 820 GeV. *ApJ*, 799: 86, January 2015c. doi: 10.1088/0004-637X/799/1/86.

M. Ackermann, A. Albert, B. Anderson, W. B. Atwood, and L. Baldini *et al.* (Fermi-LAT Collaboration). Searching for Dark Matter Annihilation from Milky Way Dwarf Spheroidal Galaxies with Six Years of Fermi Large Area Telescope Data. *Phys. Rev. Lett.*, 115(23):231301, December 2015d. doi: 10.1103/PhysRevLett.115.231301.

M. Ackermann, M. Ajello, A. Albert, W. B. Atwood, and L. Baldini *et al.* The Fermi Galactic Center GeV Excess and Implications for Dark Matter. *ApJ*, 840(1):43, May 2017. doi: 10.3847/1538-4357/aa6cab.

M. Ackermann, M. Ajello, L. Baldini, J. Ballet, and G. Barbiellini *et al.* (Fermi-LAT Collaboration). Unresolved Gamma-Ray Sky through its Angular Power Spectrum. *Phys. Rev. Lett.*, 121(24):241101, December 2018. doi: 10.1103/PhysRevLett.121.241101.

R. Adam, H. Goksu, S. Brown, L. Rudnick, and C. Ferrari. γ-ray detection toward the Coma cluster with Fermi-LAT: Implications for the cosmic ray content in the hadronic scenario. *A&A*, 648:A60, April 2021. doi: 10.1051/0004-6361/202039660.

M. L. Ahnen, S. Ansoldi, L. A. Antonelli, P. Antoranz, and A. Babic *et al.* Deep observation of the NGC 1275 region with MAGIC: search of diffuse γ-ray emission from cosmic rays in the Perseus cluster. *A&A*, 589:A33, May 2016. doi: 10.1051/0004-6361/201527846.

H. Aihara, R. Armstrong, S. Bickerton, J. Bosch, and J. Coupon *et al.* First data release of the Hyper Suprime-Cam Subaru Strategic Program. *PASJ*, 70:S8, January 2018. doi: 10.1093/pasj/psx081.

Hiroaki Aihara, Yusra AlSayyad, Makoto Ando, Robert Armstrong, and James Bosch *et al*. Second data release of the Hyper Suprime-Cam Subaru Strategic Program. *PASJ*, 71(6):114, December 2019. doi: 10.1093/pasj/psz103.

Hiroaki Aihara, Yusra AlSayyad, Makoto Ando, Robert Armstrong, and James Bosch *et al*. Third Data Release of the Hyper Suprime-Cam Subaru Strategic Program. *arXiv e-prints*, art. arXiv:2108.13045, August 2021.

M. Ajello, D. Gasparrini, M. Sánchez-Conde, G. Zaharijas, and M. Gustafsson *et al*. The Origin of the Extragalactic Gamma-Ray Background and Implications for Dark Matter Annihilation. *ApJ*, 800(2):L27, February 2015. doi: 10.1088/2041-8205/800/2/L27.

M. Ajello, A. Albert, W. B. Atwood, G. Barbiellini, and D. Bastieri *et al*. Fermi-LAT Observations of High-Energy Gamma-Ray Emission toward the Galactic Center. *ApJ*, 819(1):44, March 2016. doi: 10.3847/0004-637X/819/1/44.

Albert, A., B. Anderson, K. Bechtol, A. Drlica-Wagner, and M. Meyer *et al*. Searching for Dark Matter Annihilation in Recently Discovered Milky Way Satellites with Fermi-Lat. *ApJ*, 834(2):110, Jan 2017. doi: 10.3847/1538-4357/834/2/110.

S. Ando. Power spectrum tomography of dark matter annihilation with local galaxy distribution. *J. Cosmology Astropart. Phys.*, 10:061, October 2014. doi: 10.1088/1475-7516/2014/10/061.

Shin'ichiro Ando and Daisuke Nagai. Fermi-LAT constraints on dark matter annihilation cross section from observations of the Fornax cluster. *J. Cosmology Astropart. Phys.*, 2012(7):017, July 2012. doi: 10.1088/1475-7516/2012/07/017.

Shin'ichiro Ando, Aurélien Benoit-Lévy, and Eiichiro Komatsu. Mapping dark matter in the gamma-ray sky with galaxy catalogs. *Phys. Rev. D*, 90(2):023514, Jul 2014. doi: 10.1103/PhysRevD.90.023514.

Shin'ichiro Ando, Alex Geringer-Sameth, Nagisa Hiroshima, Sebastian Hoof, Roberto Trotta, and Matthew G. Walker. Structure formation models weaken limits on wimp dark matter from dwarf spheroidal galaxies. *Phys. Rev. D*, 102:061302, Sep 2020. doi: 10.1103/PhysRevD.102.061302. URL https://link.aps.org/doi/10.1103/PhysRevD.102.061302.

ATLAS Collaboration. Constraints on new phenomena via Higgs boson couplings and invisible decays with the ATLAS detector. *arXiv e-prints*, art. arXiv:1509.00672, September 2015.

Atlas Collaboration. Search for new phenomena in final states with an energetic jet and large missing transverse momentum in p p collisions at $\sqrt{\{s\}}$=13 TeV using the ATLAS detector. *Phys. Rev. D*, 94(3):032005, August 2016. doi: 10.1103/PhysRevD.94.032005.

W. B. Atwood, A. A. Abdo, M. Ackermann, W. Althouse, and B. Anderson *et al.* The Large Area Telescope on the Fermi Gamma-Ray Space Telescope Mission. *ApJ*, 697 (2):1071–1102, June 2009. doi: 10.1088/0004-637X/697/2/1071.

J. Ballet, T. H. Burnett, S. W. Digel, and B. Lott. Fermi Large Area Telescope Fourth Source Catalog Data Release 2. *arXiv e-prints*, art. arXiv:2005.11208, May 2020.

Julien Baur, Nathalie Palanque-Delabrouille, Christophe Yèche, Alexey Boyarsky, Oleg Ruchayskiy, Éric Armengaud, and Julien Lesgourgues. Constraints from Ly-α forests on non-thermal dark matter including resonantly-produced sterile neutrinos. *J. Cosmology Astropart. Phys.*, 2017(12):013, December 2017. doi: 10.1088/1475-7516/2017/12/013.

R. Bernabei, P. Belli, F. Cappella, V. Caracciolo, and S. Castellano *et al.* Final model independent result of DAMA/LIBRA-phase1. *European Physical Journal C*, 73:2648, December 2013. doi: 10.1140/epjc/s10052-013-2648-7.

E. Bertin and S. Arnouts. SExtractor: Software for source extraction. *A&AS*, 117: 393–404, June 1996. doi: 10.1051/aas:1996164.

Gianfranco Bertone and Dan Hooper. History of dark matter. *Reviews of Modern Physics*, 90(4):045002, October 2018. doi: 10.1103/RevModPhys.90.045002.

Pooja Bhattacharjee, Pratik Majumdar, Mousumi Das, Subinoy Das, Partha S. Joarder, and Sayan Biswas. Multiwavelength analysis of low surface brightness galaxies to study possible dark matter signature. *MNRAS*, 501(3):4238–4254, March 2021. doi: 10.1093/mnras/staa3877.

Michael R. Blanton, Eyal Kazin, Demitri Muna, Benjamin A. Weaver, and Adrian Price-Whelan. Improved Background Subtraction for the Sloan Digital Sky Survey Images. *AJ*, 142(1):31, July 2011. doi: 10.1088/0004-6256/142/1/31.

Kimberly K. Boddy, Jason Kumar, Danny Marfatia, and Pearl Sand ick. Model-independent constraints on dark matter annihilation in dwarf spheroidal galaxies. *Phys. Rev. D*, 97(9):095031, May 2018. doi: 10.1103/PhysRevD.97.095031.

J. Bosch, R. Armstrong, S. Bickerton, H. Furusawa, and H. Ikeda *et al*. The Hyper Suprime-Cam software pipeline. *PASJ*, 70:S5, January 2018. doi: 10.1093/pasj/psx080.

Torsten Bringmann, Joakim Edsjö, Paolo Gondolo, Piero Ullio, and Lars Bergström. DarkSUSY 6: an advanced tool to compute dark matter properties numerically. *Journal of Cosmology and Astro-Particle Physics*, 2018(7):033, Jul 2018. doi: 10.1088/1475-7516/2018/07/033.

Tian-Wen Cao, Hong Wu, Wei Du, Feng-Jie Lei, Ming Zhu, Jan Wouterloot, Harriet Parsons, Yi-Nan Zhu, Chao-Jian Wu, Fan Yang, Chen Cao, Zhi-Min Zhou, Min He, Jun-Jie Jin, and James E. Wicker. Molecular Gas and Star-formation in Low Surface Brightness Galaxies. *AJ*, 154(3):116, September 2017. doi: 10.3847/1538-3881/aa845a.

Eric Carlson, Dan Hooper, and Tim Linden. Improving the sensitivity of gamma-ray telescopes to dark matter annihilation in dwarf spheroidal galaxies. *Phys. Rev. D*, 91 (6):061302, March 2015. doi: 10.1103/PhysRevD.91.061302.

Bernard Carr, Florian Kühnel, and Marit Sandstad. Primordial black holes as dark matter. *Phys. Rev. D*, 94(8):083504, October 2016. doi: 10.1103/PhysRevD.94.083504.

J. Carr, C. Balazs, T. Bringmann, T. Buanes, and M. Daniel *et al*. Prospects for Indirect Dark Matter Searches with the Cherenkov Telescope Array (CTA). In *34th International Cosmic Ray Conference (ICRC2015)*, volume 34 of *International Cosmic Ray Conference*, page 1203, July 2015.

Laura J. Chang, Mariangela Lisanti, and Siddharth Mishra-Sharma. Search for dark matter annihilation in the Milky Way halo. *Phys. Rev. D*, 98(12):123004, December 2018. doi: 10.1103/PhysRevD.98.123004.

E. Charles, M. Sánchez-Conde, B. Anderson, R. Caputo, and A. Cuoco *et al*. Sensitivity projections for dark matter searches with the Fermi large area telescope. *Phys. Rep.*, 636:1–46, Jun 2016. doi: 10.1016/j.physrep.2016.05.001.

Douglas Clowe, Maruša Bradač, and Anthony H. Gonzalez *et al*. A Direct Empirical Proof of the Existence of Dark Matter. *ApJ*, 648(2):L109–L113, September 2006. doi: 10.1086/508162.

Christopher J. Conselice, Aaron Wilkinson, Kenneth Duncan, and Alice Mortlock. The Evolution of Galaxy Number Density at z ¡ 8 and Its Implications. *ApJ*, 830(2):83, October 2016. doi: 10.3847/0004-637X/830/2/83.

Basudeb Dasgupta and Joachim Kopp. Sterile neutrinos. *Phys. Rep.*, 928:1–63, September 2021. doi: 10.1016/j.physrep.2021.06.002.

W. J. C. de Blok and S. S. McGough. Dark Matter in Low Surface Brightness Galaxies. In Massimo Persic and Paolo Salucci, editors, *Dark and Visible Matter in Galaxies and Cosmological Implications*, volume 117 of *Astronomical Society of the Pacific Conference Series*, page 39, January 1997.

Chiara Di Paolo, Paolo Salucci, and Adnan Erkurt. The universal rotation curve of low surface brightness galaxies - IV. The interrelation between dark and luminous matter. *MNRAS*, 490(4):5451–5477, December 2019. doi: 10.1093/mnras/stz2700.

A. Drlica-Wagner, I. Sevilla-Noarbe, E. S. Rykoff, R. A. Gruendl, and B. Yanny *et al.* (DES Collaboration). Dark Energy Survey Year 1 Results: The Photometric Data Set for Cosmology. *ApJS*, 235(2):33, April 2018. doi: 10.3847/1538-4365/aab4f5.

Wei Du, Hong Wu, Man I. Lam, Yinan Zhu, Fengjie Lei, and Zhimin Zhou. Low Surface Brightness Galaxies Selected from the 40% Sky Area of the ALFALFA H I Survey. I. Sample and Statistical Properties. *AJ*, 149(6):199, June 2015. doi: 10.1088/0004-6256/149/6/199.

Wei Du, Cheng Cheng, Hong Wu, Ming Zhu, and Yougang Wang. Low Surface Brightness Galaxy catalogue selected from the α.40-SDSS DR7 Survey and Tully-Fisher relation. *MNRAS*, 483(2):1754–1795, February 2019. doi: 10.1093/mnras/sty2976.

A. A. Dutton and A. V. Macciò. Cold dark matter haloes in the Planck era: evolution of structural parameters for Einasto and NFW profiles. *MNRAS*, 441:3359–3374, July 2014a. doi: 10.1093/mnras/stu742.

Aaron A. Dutton and Andrea V. Macciò. Cold dark matter haloes in the Planck era: evolution of structural parameters for Einasto and NFW profiles. *MNRAS*, 441(4): 3359–3374, Jul 2014b. doi: 10.1093/mnras/stu742.

P. Erwin. IMFIT: A Fast, Flexible New Program for Astronomical Image Fitting. *ApJ*, 799:226, February 2015. doi: 10.1088/0004-637X/799/2/226.

B. Flaugher, H. T. Diehl, K. Honscheid, T. M. C. Abbott, and O. Alvarez *et al.* (DES collaboration). The Dark Energy Camera. *AJ*, 150(5):150, November 2015. doi: 10.1088/0004-6256/150/5/150.

K. C. Freeman. On the Disks of Spiral and S0 Galaxies. *ApJ*, 160:811, June 1970. doi: 10.1086/150474.

Gaspar Galaz, Rodrigo Herrera-Camus, Diego Garcia-Lambas, and Nelson Padilla. Low Surface Brightness Galaxies in the SDSS: The Link Between Environment, Star-forming Properties, and Active Galactic Nuclei. *ApJ*, 728(2):74, February 2011. doi: 10.1088/0004-637X/728/2/74.

V. Gammaldi, E. Karukes, and P. Salucci. Theoretical predictions for dark matter detection in dwarf irregular galaxies with gamma rays. *Phys. Rev. D*, 98(8):083008, October 2018. doi: 10.1103/PhysRevD.98.083008.

C. Gordon and O. Macías. Dark matter and pulsar model constraints from Galactic Center Fermi-LAT gamma-ray observations. *Phys. Rev. D*, 88(8):083521, October 2013. doi: 10.1103/PhysRevD.88.083521.

J. P. Greco, J. E. Greene, M. A. Strauss, L. A. Macarthur, and X. Flowers *et al.* Illuminating Low Surface Brightness Galaxies with the Hyper Suprime-Cam Survey. *ApJ*, 857:104, April 2018a. doi: 10.3847/1538-4357/aab842.

Johnny P. Greco, Andy D. Goulding, Jenny E. Greene, Michael A. Strauss, Song Huang, Ji Hoon Kim, and Yutaka Komiyama. A Study of Two Diffuse Dwarf Galaxies in the Field. *ApJ*, 866:112, October 2018b. doi: 10.3847/1538-4357/aae0f4.

Kim Griest and Marc Kamionkowski. Unitarity limits on the mass and radius of dark-matter particles. *Phys. Rev. Lett.*, 64:615–618, Feb 1990. doi: 10.1103/PhysRevLett.64.615. URL https://link.aps.org/doi/10.1103/PhysRevLett.64.615.

Kim Griest and David Seckel. Three exceptions in the calculation of relic abundances. *Phys. Rev. D*, 43:3191–3203, 1991. doi: 10.1103/PhysRevD.43.3191.

Daiki Hashimoto, Oscar Macias, Atsushi J. Nishizawa, Kohei Hayashi, and Masahiro Takada *et al*. Constraining dark matter annihilation with HSC low surface brightness galaxies. *J. Cosmology Astropart. Phys.*, 2020(1):059, January 2020. doi: 10.1088/1475-7516/2020/01/059.

Häußler, Boris, Steven P. Bamford, Marina Vika, Alex L. Rojas, and Marco Barden *et al*. MegaMorph - multiwavelength measurement of galaxy structure: complete Sérsic profile information from modern surveys. *MNRAS*, 430(1):330–369, March 2013. doi: 10.1093/mnras/sts633.

Martha P. Haynes, Riccardo Giovanelli, Ann M. Martin, Kelley M. Hess, and Amélie Saintonge *et al*. The Arecibo Legacy Fast ALFA Survey: The α.40 H I Source Catalog, Its Characteristics and Their Impact on the Derivation of the H I Mass Function. *AJ*, 142 (5):170, November 2011. doi: 10.1088/0004-6256/142/5/170.

O. Helene. Upper limit of peak area. *Nuclear Instruments and Methods in Physics Research*, 212(1-3):319–322, Jul 1983. doi: 10.1016/0167-5087(83)90709-3.

Sergio Hernández Cadena, Rubén Alfaro, Andrés Sandoval, Ernesto Belmont, Hermes León, Viviana Gammaldi, Ekaterina Karukes, and Paolo Salucci. Searching for TeV DM evidence from Dwarf Irregular Galaxies with the HAWC Observatory. *arXiv e-prints*, art. arXiv:1708.04642, August 2017.

Chiaki Hikage, Masamune Oguri, Takashi Hamana, Surhud More, and Shiang-Yu *et al*Rachel Mandelbaum. Cosmology from cosmic shear power spectra with Subaru Hyper Suprime-Cam first-year data. *PASJ*, 71(2):43, April 2019. doi: 10.1093/pasj/psz010.

N. Hiroshima, S. Ando, and T. Ishiyama. Modeling evolution of dark matter substructure and annihilation boost. *Phys. Rev. D*, 97(12):123002, June 2018. doi: 10.1103/PhysRevD.97.123002.

R. F. L. Holanda, R. S. Gonçalves, J. E. Gonzalez, and J. S. Alcaniz. An estimate of the dark matter density from galaxy clusters and supernovae data. *J. Cosmology Astropart. Phys.*, 2019(11):032, November 2019. doi: 10.1088/1475-7516/2019/11/032.

S. Hoof, A. Geringer-Sameth, and R. Trotta. A Global Analysis of Dark Matter Signals from 27 Dwarf Spheroidal Galaxies using Ten Years of Fermi-LAT Observations. *arXiv e-prints*, December 2018.

Sebastian Hoof, Alex Geringer-Sameth, and Roberto Trotta. A global analysis of dark matter signals from 27 dwarf spheroidal galaxies using 11 years of Fermi-LAT observations. *J. Cosmology Astropart. Phys.*, 2020(2):012, February 2020. doi: 10.1088/1475-7516/2020/02/012.

Dan Hooper and Lisa Goodenough. Dark matter annihilation in the Galactic Center as seen by the Fermi Gamma Ray Space Telescope. *Physics Letters B*, 697(5):412–428, March 2011. doi: 10.1016/j.physletb.2011.02.029.

Travis J. Hurst, Andrew R. Zentner, Aravind Natarajan, and Carles Badenes. Indirect probes of dark matter and globular cluster properties from dark matter annihilation within the coolest white dwarfs. *Phys. Rev. D*, 91(10):103514, May 2015. doi: 10.1103/PhysRevD.91.103514.

Chris Impey and Greg Bothun. Low Surface Brightness Galaxies. *ARA&A*, 35:267–307, January 1997. doi: 10.1146/annurev.astro.35.1.267.

Tesla E. Jeltema and Stefano Profumo. Fitting the Gamma-Ray Spectrum from Dark Matter with DMFIT: GLAST and the Galactic Center Region. *JCAP*, 0811:003, 2008. doi: 10.1088/1475-7516/2008/11/003.

S. Jester, D. P. Schneider, G. T. Richards, R. F. Green, and M. Schmidt *et al.* The Sloan Digital Sky Survey View of the Palomar-Green Bright Quasar Survey. *AJ*, 130:873–895, September 2005. doi: 10.1086/432466.

D. Heath Jones, Will Saunders, Matthew Colless, Mike A. Read, and Quentin A. Parker *et al.* The 6dF Galaxy Survey: samples, observational techniques and the first data release. *MNRAS*, 355(3):747–763, December 2004. doi: 10.1111/j.1365-2966.2004.08353.x.

D. Heath Jones, Mike A. Read, Will Saunders, Matthew Colless, and Tom Jarrett *et al.* *MNRAS*, 399(2):683–698, October 2009. doi: 10.1111/j.1365-2966.2009.15338.x.

M. Jurić, J. Kantor, K. T. Lim, R. H. Lupton, and G. Dubois-Felsmann *et al*. The LSST Data Management System. In N. P. F. Lorente, K. Shortridge, and R. Wayth, editors, *Astronomical Data Analysis Software and Systems XXV*, volume 512 of *Astronomical Society of the Pacific Conference Series*, page 279, December 2017.

Andrey Katz, Joachim Kopp, Sergey Sibiryakov, and Wei Xue. Femtolensing by dark matter revisited. *J. Cosmology Astropart. Phys.*, 2018(12):005, December 2018. doi: 10.1088/1475-7516/2018/12/005.

Y. Komiyama, Y. Obuchi, H. Nakaya, Y. Kamata, and S. Kawanomoto *et al*. Hyper Suprime-Cam: Camera dewar design. *PASJ*, 70:S2, January 2018. doi: 10.1093/pasj/psx069.

Michael Kuhlen, Mark Vogelsberger, and Raul Angulo. Numerical simulations of the dark universe: State of the art and the next decade. *Physics of the Dark Universe*, 1(1-2): 50–93, November 2012. doi: 10.1016/j.dark.2012.10.002.

S. D. Landy and A. S. Szalay. Bias and variance of angular correlation functions. *ApJ*, 412:64–71, July 1993. doi: 10.1086/172900.

Benjamin W. Lee and Steven Weinberg. Cosmological lower bound on heavy-neutrino masses. *Phys. Rev. Lett.*, 39:165–168, Jul 1977. doi: 10.1103/PhysRevLett.39.165. URL https://link.aps.org/doi/10.1103/PhysRevLett.39.165.

Feng-Jie Lei. Star Formation in Low Surface Brightness Galaxies. *PASP*, 131(1006): 127001, December 2019. doi: 10.1088/1538-3873/ab45cd.

Feng-Jie Lei, Hong Wu, Yi-Nan Zhu, Wei Du, and Min He *et al*. An Hα Imaging Survey of the Low Surface Brightness Galaxies Selected from the Spring Sky Region of the 40% ALFALFA H I Survey. *ApJS*, 242(1):11, May 2019. doi: 10.3847/1538-4365/ab16ee.

Mariangela Lisanti, Siddharth Mishra-Sharma, Nicholas L. Rodd, and Benjamin R. Safdi. Search for Dark Matter Annihilation in Galaxy Groups. *Phys. Rev. Lett.*, 120:101101, Mar 2018. doi: 10.1103/PhysRevLett.120.101101.

Paola Marigo, Léo Girardi, Alessandro Bressan, Philip Rosenfield, and Bernhard Aringer *et al*. A New Generation of PARSEC-COLIBRI Stellar Isochrones Including the TP-AGB Phase. *ApJ*, 835(1):77, January 2017. doi: 10.3847/1538-4357/835/1/77.

David J. E. Marsh. Axion cosmology. *Phys. Rep.*, 643:1–79, July 2016. doi: 10.1016/j.physrep.2016.06.005.

L. D. Matthews, W. van Driel, and D. Monnier-Ragaigne. H I observations of giant low surface brightness galaxies. *A&A*, 365:1–10, January 2001. doi: 10.1051/0004-6361:20000002.

S. S. McGaugh and G. D. Bothun. Structural Characteristics and Stellar Composition of Low Surface Brightness Disk Galaxies. *AJ*, 107:530, February 1994. doi: 10.1086/116874.

Brice Ménard, Ryan Scranton, Samuel Schmidt, Chris Morrison, and Donghui Jeong *et al.* Clustering-based redshift estimation: method and application to data. *arXiv e-prints*, art. arXiv:1303.4722, March 2013.

R. F. Minchin, M. J. Disney, Q. A. Parker, P. J. Boyce, and W. J. G. de Blok *et al.* The cosmological significance of low surface brightness galaxies found in a deep blind neutral hydrogen survey. *MNRAS*, 355(4):1303–1314, December 2004. doi: 10.1111/j.1365-2966.2004.08409.x.

S. Miyazaki, Y. Komiyama, S. Kawanomoto, Y. Doi, and H. Furusawa *et al.* Hyper Suprime-Cam: System design and verification of image quality. *PASJ*, 70:S1, January 2018. doi: 10.1093/pasj/psx063.

E. Morganson, R. A. Gruendl, F. Menanteau, M. Carrasco Kind, and Y. C. Chen *et al.* The Dark Energy Survey Image Processing Pipeline. *PASP*, 130(989):074501, July 2018. doi: 10.1088/1538-3873/aab4ef.

B. P. Moster, T. Naab, and S. D. M. White. Galactic star formation and accretion histories from matching galaxies to dark matter haloes. *MNRAS*, 428:3121–3138, February 2013. doi: 10.1093/mnras/sts261.

Riccardo Murgia, Vid Iršič, and Matteo Viel. Novel constraints on noncold, nonthermal dark matter from Lyman-α forest data. *Phys. Rev. D*, 98(8):083540, October 2018. doi: 10.1103/PhysRevD.98.083540.

J. F. Navarro, C. S. Frenk, and S. D. M. White. The Structure of Cold Dark Matter Halos. *ApJ*, 462:563, May 1996. doi: 10.1086/177173.

Jeffrey A. Newman. Calibrating Redshift Distributions beyond Spectroscopic Limits with Cross-Correlations. *ApJ*, 684(1):88–101, September 2008. doi: 10.1086/589982.

Takeshi Nihei, Leszek Roszkowski, and Roberto Ruiz de Austri. Towards an accurate calculation of the neutralino relic density. *Journal of High Energy Physics*, 2001(5): 063, May 2001. doi: 10.1088/1126-6708/2001/05/063.

P. L. Nolan, A. A. Abdo, M. Ackermann, M. Ajello, and A. Allafort *et al*. Fermi Large Area Telescope Second Source Catalog. *ApJS*, 199(2):31, Apr 2012. doi: 10.1088/0067-0049/199/2/31.

C. Patrignani et al. Review of Particle Physics. *Chin. Phys. C*, 40(10):100001, 2016. doi: 10.1088/1674-1137/40/10/100001.

Jovana Petrović, Pasquale Dario Serpico, and Gabrijela Zaharijaš. Galactic Center gamma-ray "excess" from an active past of the Galactic Centre? *J. Cosmology Astropart. Phys.*, 2014(10):052, October 2014. doi: 10.1088/1475-7516/2014/10/052.

R. W. Pike and Michael J. Hudson. Cosmological Parameters from the Comparison of the 2MASS Gravity Field with Peculiar Velocity Surveys. *ApJ*, 635(1):11–21, December 2005. doi: 10.1086/497359.

Planck Collaboration, N. Aghanim, Y. Akrami, M. Ashdown, J. Aumont, C. Baccigalupi, and *et al.* Planck 2018 results. VI. Cosmological parameters. *arXiv e-prints*, art. arXiv:1807.06209, Jul 2018.

D. J. Prole, M. Hilker, R. F. J. van der Burg, M. Cantiello, and A. Venhola *et al*. Halo mass estimates from the globular cluster populations of 175 low surface brightness galaxies in the Fornax cluster. *MNRAS*, 484(4):4865–4880, Apr 2019. doi: 10.1093/mnras/stz326.

Scott W. Randall, Maxim Markevitch, Douglas Clowe, Anthony H. Gonzalez, and Marusa Bradač. Constraints on the Self-Interaction Cross Section of Dark Matter from Numerical Simulations of the Merging Galaxy Cluster 1E 0657-56. *ApJ*, 679(2):1173–1180, June 2008. doi: 10.1086/587859.

M. Regis, J.-Q. Xia, A. Cuoco, E. Branchini, N. Fornengo, and M. Viel. Particle Dark Matter Searches Outside the Local Group. *Physical Review Letters*, 114(24):241301, June 2015. doi: 10.1103/PhysRevLett.114.241301.

Sarah Roberts, Jonathan Davies, Sabina Sabatini, Wim van Driel, and Karen O'Neil *et al*. A search for low surface brightness dwarf galaxies in different environments. *MNRAS*, 352(2):478–492, August 2004. doi: 10.1111/j.1365-2966.2004.07934.x.

Vera C. Rubin and Jr. Ford, W. Kent. Rotation of the Andromeda Nebula from a Spectroscopic Survey of Emission Regions. *ApJ*, 159:379, February 1970. doi: 10.1086/150317.

Misao Sasaki, Teruaki Suyama, Takahiro Tanaka, and Shuichiro Yokoyama. Primordial black holes—perspectives in gravitational wave astronomy. *Classical and Quantum Gravity*, 35(6):063001, March 2018. doi: 10.1088/1361-6382/aaa7b4.

Jose Luis Sersic. *Atlas de Galaxias Australes*. 1968.

I. Sevilla-Noarbe, K. Bechtol, M. Carrasco Kind, A. Carnero Rosell, and M. R. Becker *et al.* (DES collaboration). Dark Energy Survey Year 3 Results: Photometric Data Set for Cosmology. *ApJS*, 254(2):24, June 2021. doi: 10.3847/1538-4365/abeb66.

Pierre Sikivie. *Axion Cosmology*, volume 741, page 19. 2008.

Gary Steigman, Basudeb Dasgupta, and John F. Beacom. Precise relic WIMP abundance and its impact on searches for dark matter annihilation. *Phys. Rev. D*, 86(2):023506, Jul 2012. doi: 10.1103/PhysRevD.86.023506.

Sunao Sugiyama, Masahiro Takada, Hironao Miyatake, Takahiro Nishimichi, and Masato Shirasaki *et al*.

D. Tanoglidis, A. Drlica-Wagner, K. Wei, T. S. Li, and J. Sánchez *et al.* (DES Collaboration). Shadows in the Dark: Low-surface-brightness Galaxies Discovered in the Dark Energy Survey. *ApJS*, 252(2):18, February 2021. doi: 10.3847/1538-4365/abca89.

Charles Thorpe-Morgan, Denys Malyshev, Christoph-Alexander Stegen, Andrea Santangelo, and Josef Jochum. Annihilating dark matter search with 12 yr of Fermi LAT data in nearby galaxy clusters. *MNRAS*, 502(3):4039–4047, April 2021. doi: 10.1093/mnras/stab208.

C. Trachternach, D. J. Bomans, L. Haberzettl, and R. J. Dettmar. An optical search for low surface brightness galaxies in the Arecibo HI Strip Survey. *A&A*, 458(1):341–348, October 2006. doi: 10.1051/0004-6361:20054545.

Martin Vollmann, Volker Heesen, Timothy W. Shimwell, Martin J. Hardcastle, Marcus Brüggen, Günter Sigl, and Huub J. A. Röttgering. Radio constraints on dark matter annihilation in Canes Venatici I with LOFAR. *MNRAS*, 496(3):2663–2672, August 2020. doi: 10.1093/mnras/staa1657.

S. S. Wilks. The large-sample distribution of the likelihood ratio for testing composite hypotheses. *The Annals of Mathematical Statistics*, 9(1):60–62, 1938. ISSN 00034851. URL http://www.jstor.org/stable/2957648.

Henriette Wirth, Kenji Bekki, and Kohei Hayashi. Formation of massive globular clusters with dark matter and its implication on dark matter annihilation. *MNRAS*, 496(1): L70–L74, July 2020. doi: 10.1093/mnrasl/slaa089.

J. Woo, S. Courteau, and A. Dekel. Scaling relations and the fundamental line of the local group dwarf galaxies. *MNRAS*, 390:1453–1469, November 2008. doi: 10.1111/j.1365-2966.2008.13770.x.

Xenon Collaboration. First Dark Matter Search Results from the XENON1T Experiment. *Phys. Rev. Lett.*, 119(18):181301, November 2017. doi: 10.1103/PhysRevLett.119.181301.

XMASS Collaboration. Direct dark matter search by annual modulation in XMASS-I. *arXiv e-prints*, art. arXiv:1511.04807, November 2015.

P. C. Zinn, M. Stritzinger, J. Braithwaite, A. Gallazzi, and P. Grunden *et al*. Supernovae without host galaxies?. The low surface brightness host of SN 2009Z. *A&A*, 538:A30, February 2012. doi: 10.1051/0004-6361/201116433.

F. Zwicky. Die Rotverschiebung von extragalaktischen Nebeln. *Helvetica Physica Acta*, 6:110–127, January 1933.